THE GEOLOGICAL SOCIETY OF AMERICA®

Compressional origin of the Naxos metamorphic core complex, Greece: Structure, petrography, and thermobarometry

Thomas N. Lamont[1,†], Michael P. Searle[1], David J. Waters[1], Nick M.W. Roberts[2], Richard M. Palin[3], Andrew Smye[4], Brendan Dyck[5], Phillip Gopon[1], Owen M. Weller[6], and Marc R. St-Onge[7]

[1]*Department Earth Sciences, University of Oxford, South Parks Road, Oxford, OX1 3AN, UK*
[2]*Geochronology and Tracers Facility, British Geological Survey, Environmental Science Centre, Nottingham, NG12 5GG, UK*
[3]*Department of Geology and Geological Engineering, Colorado School of Mines, Golden, Colorado 80401, USA*
[4]*Department of Geosciences, The Pennsylvania State University, University Park, Pennsylvania 16802, USA*
[5]*Department of Earth Sciences, Simon Fraser University, 8888 University Drive, Burnaby, British Columbia, V5A 1S6, Canada*
[6]*Department of Earth Sciences, University of Cambridge, Downing Street, Cambridge, CB2 3EQ, UK*
[7]*Geological Survey of Canada, 601 Booth Street, Ottawa, Ontario, K1A 0E8, Canada*

ABSTRACT

The island of Naxos, Greece, has been previously considered to represent a Cordilleran-style metamorphic core complex that formed during Cenozoic extension of the Aegean Sea. Although lithospheric extension has undoubtedly occurred in the region since 10 Ma, the geodynamic history of older, regional-scale, kyanite- and sillimanite-grade metamorphic rocks exposed within the core of the Naxos dome is controversial. Specifically, little is known about the pre-extensional prograde evolution and the relative timing of peak metamorphism in relation to the onset of extension. In this work, new structural mapping is presented and integrated with petrographic analyses and phase equilibrium modeling of blueschists, kyanite gneisses, and anatectic sillimanite migmatites. The kyanite-sillimanite–grade rocks within the core complex record a complex history of burial and compression and did not form under crustal extension. Deformation and metamorphism were diachronous and advanced down the structural section, resulting in the juxtaposition of several distinct tectono-stratigraphic nappes that experienced contrasting metamorphic histories. The Cycladic Blueschists attained ~14.5 kbar and 470 °C during attempted northeast-directed subduction of the continental margin. These were subsequently thrusted onto the more proximal continental margin, resulting in crustal thickening and regional metamorphism associated with kyanite-grade conditions of ~10 kbar and 600–670 °C. With continued shortening, the deepest structural levels underwent kyanite-grade hydrous melting at ~8–10 kbar and 680–750 °C, followed by isothermal decompression through the muscovite dehydration melting reaction to sillimanite-grade conditions of ~5–6 kbar and 730 °C. This decompression process was associated with top-to-the-NNE shearing along passive-roof faults that formed because of SW-directed extrusion. These shear zones predated crustal extension, because they are folded around the migmatite dome and are crosscut by leucogranites and low-angle normal faults. The migmatite dome formed at lower-pressure conditions under horizontal constriction that caused vertical boudinage and upright isoclinal folds. The switch from compression to extension occurred immediately following doming and was associated with NNE-SSW horizontal boudinage and top-to-the-NNE brittle-ductile normal faults that truncate the internal shear zones and earlier collisional features. The Naxos metamorphic core complex is interpreted to have formed via crustal thickening, regional metamorphism, and partial melting in a compressional setting, here termed the Aegean orogeny, and it was exhumed from the midcrust due to the switch from compression to extension at ca. 15 Ma.

INTRODUCTION

Metamorphic core complexes (MCCs) are generally believed to form during lithospheric extension (e.g., Lister et al., 1984; Teyssier and Whitney, 2002). However, the pre-extensional histories of many such examples worldwide are poorly understood, including those on the Cycladic islands, Greece. MCCs occur in a variety of tectonic settings, ranging from wholly extensional (e.g., Basin and Range Province; Coney, 1980; Armstrong, 1982; Flecher and Hallet, 1983; Wernicke, 1985; Yin, 1991) to purely compressional (e.g., North Himalayan gneiss domes; e.g., Burg et al., 1984; Lee et al., 2004, 2006) regimes, making it unlikely that they share a common mechanism of formation (Platt et al., 2014). Although the exhumation of deep-crustal metamorphic rocks by footwall unroofing beneath an extensional detachment fault is now largely accepted (Wernicke, 1981; Axen, 2007), there remains a limited understanding of the relationship between the timing of metamorphism and the onset of extensional motion (Platt et al., 2014). Furthermore, the processes driving the initiation of detachment faulting, and whether these are associated with lithospheric-scale faulting or localized extension in a compressional environment (e.g., Searle, 2010), are still debated (Fig. 1).

The transition from compression to extension is commonly recorded by the development of characteristic extensional structures and metamorphic assemblages that overprint older collisional features (Platt, 1986; Vanderhaeghe and Teyssier, 2001). Examples include overprinting of suture zones by low-angle extensional detachments, and the replacement of high-pressure–low-temperature metamorphic mineral assemblages by high-temperature–medium-pressure assemblages, often due to an increased basal heat flow associated with crustal thinning, e.g., Betics Rif, Spain (e.g., Platt et al., 2013). Nevertheless,

[†]tnl1@st-andrews.ac.uk

GSA Bulletin; https://doi.org/10.1130/B31978.1; 23 figures; 5 tables; Data Repository item 2019167.

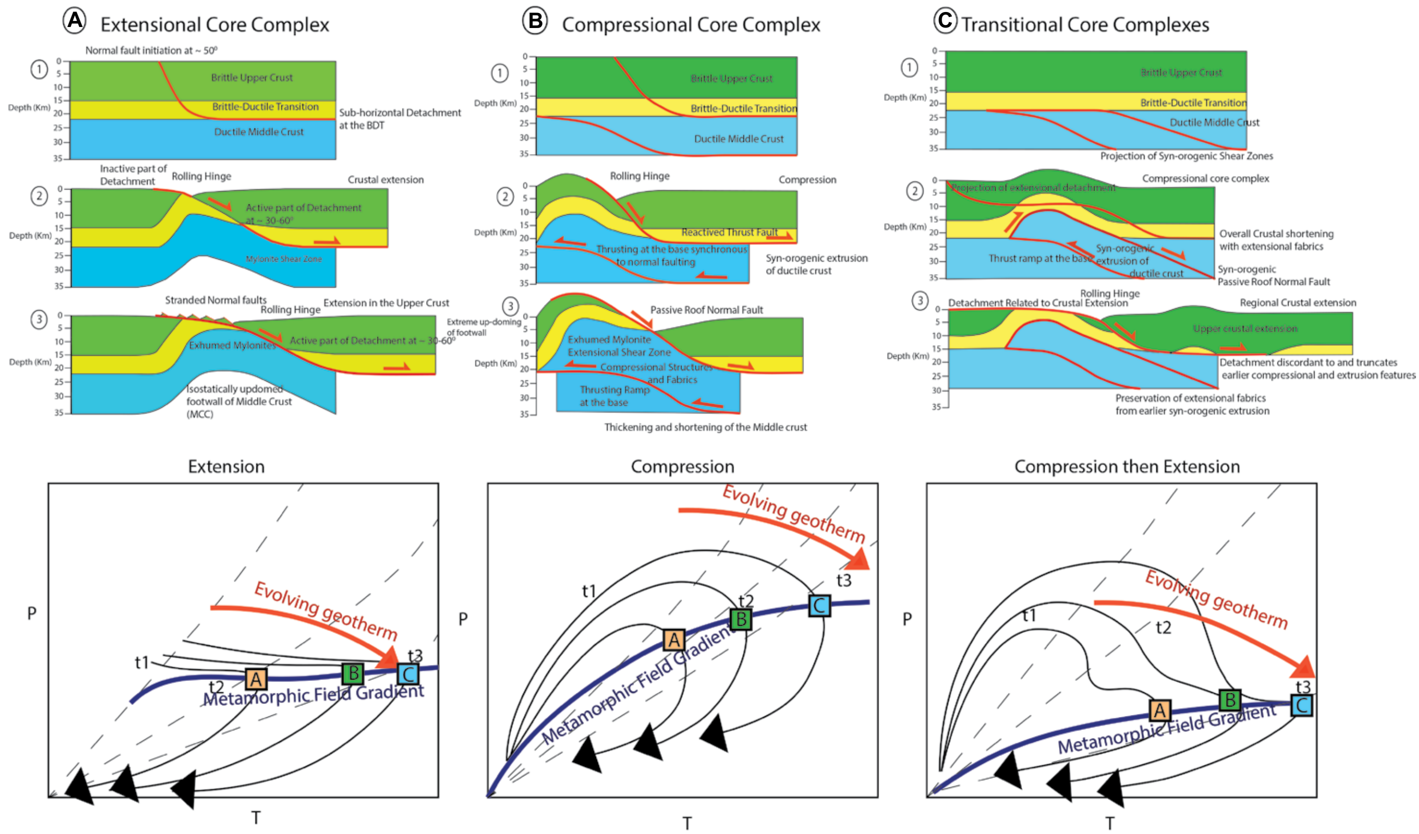

Figure 1. Schematic cartoons illustrating various tectonic models and pressure-temperature-time (*P-T-t*) paths associated with the formation of metamorphic core complexes (MCCs) (after Weller et al., 2013). The cogenetic suite of *P-T-t* paths is shown for three samples (A, B, and C), where the *P-T* loci of their respective *T*-max positions define the metamorphic field gradient, which is typically concave to the *T*-axis, polychronic, and at a steep angle to the *P-T* paths of an individual sample (England and Richardson, 1977; England and Thompson, 1984; Spear, 1993): (A) Classical cordilleran-style MCC formed by simple shear extension of the entire continental lithosphere and unroofing under a low-angle normal fault (e.g., Basin and Range). Predicted *P-T-t* path dominantly follows an isobaric heating excursion at lower pressure due to increased basal heating. BDT—brittle-ductile transition. (B) Compressional-type MCCs formed by doming above a thrust ramp at depth coeval with exhumation under a passive-roof normal fault (e.g., North Himalayan gneiss domes). These record a classical Barrovian type *P-T-t* path with heating to peak temperatures due to radiogenic heating. (C) Transitional MCC, where compression and crustal thickening cause metamorphism and early synorogenic extrusion followed by the switch to regional extension responsible for the last phase of heating and exhumation. This type is characterized by a classical Barrovian-type clockwise *P-T-t* path followed by an isobaric heating excursion upon the onset of extension.

Barrovian metamorphic overprints and MCCs are characteristic features in many active orogens, such as the Lepontine Dome and Tauern Window in the Alps (e.g., Smye et al., 2011, and references therein) and the Greater Himalayan Series (GHS) in the Himalayan Range (e.g., Jessup et al., 2006; Searle et al., 2006). Notably, a thickened crust that formed in response to continental collision would also equilibrate along a hotter geothermal gradient, resulting in widespread regional metamorphism driven largely by the conductive relaxation of perturbed isotherms (Bickle et al., 1975; England and Richardson, 1977; England and Thompson, 1984).

Although normal-sense extensional shear fabrics indeed record localized extension on their associated shear zone, they occur in zones of both overall crustal shortening and extension, and they record the relative uplift and exhumation of material, rather than a specific tectonic stress regime. Extensional microstructures typically form via one of three geodynamic mechanisms: (1) buoyancy-driven extrusion of crustal material transported to depth within a subduction zone, which occurs under a passive-roof normal fault on the interface between the subducting slab and overlying mantle wedge, in conditions responsible for creating extensional fabrics in blueschists and eclogites (e.g., England and Holland, 1979; Hacker et al., 2013); (2) exhumation and extrusion of high-grade migmatites and gneisses from a deep crustal root by coeval movement of a thrust at the base and an extensional synorogenic normal fault at the top (e.g., the top of the GHS beneath the South Tibetan Detachment System (STDS); Law et al., 2006; Searle et al., 2006); or (3) normal faulting during crustal extension and rifting (e.g., Lister et al., 1984; Jolivet et al., 2010; Teyssier and Whitney, 2002; Wernicke, 1985). Mechanisms 1 and 2 occur in compressional tectonic settings, while mechanism 3 occurs in crustal or lithospheric extensional settings. All three processes are reported herein to have occurred on Naxos.

The Cycladic islands in the Aegean Sea (Fig. 2), and the island of Naxos in particular (Fig. 3), expose a range of geological features that document the transition from a compressional to an extensional tectonic regime (Jansen and Schuiling, 1976; Buick and Holland, 1989; Urai et al., 1990). Naxos also exposes the

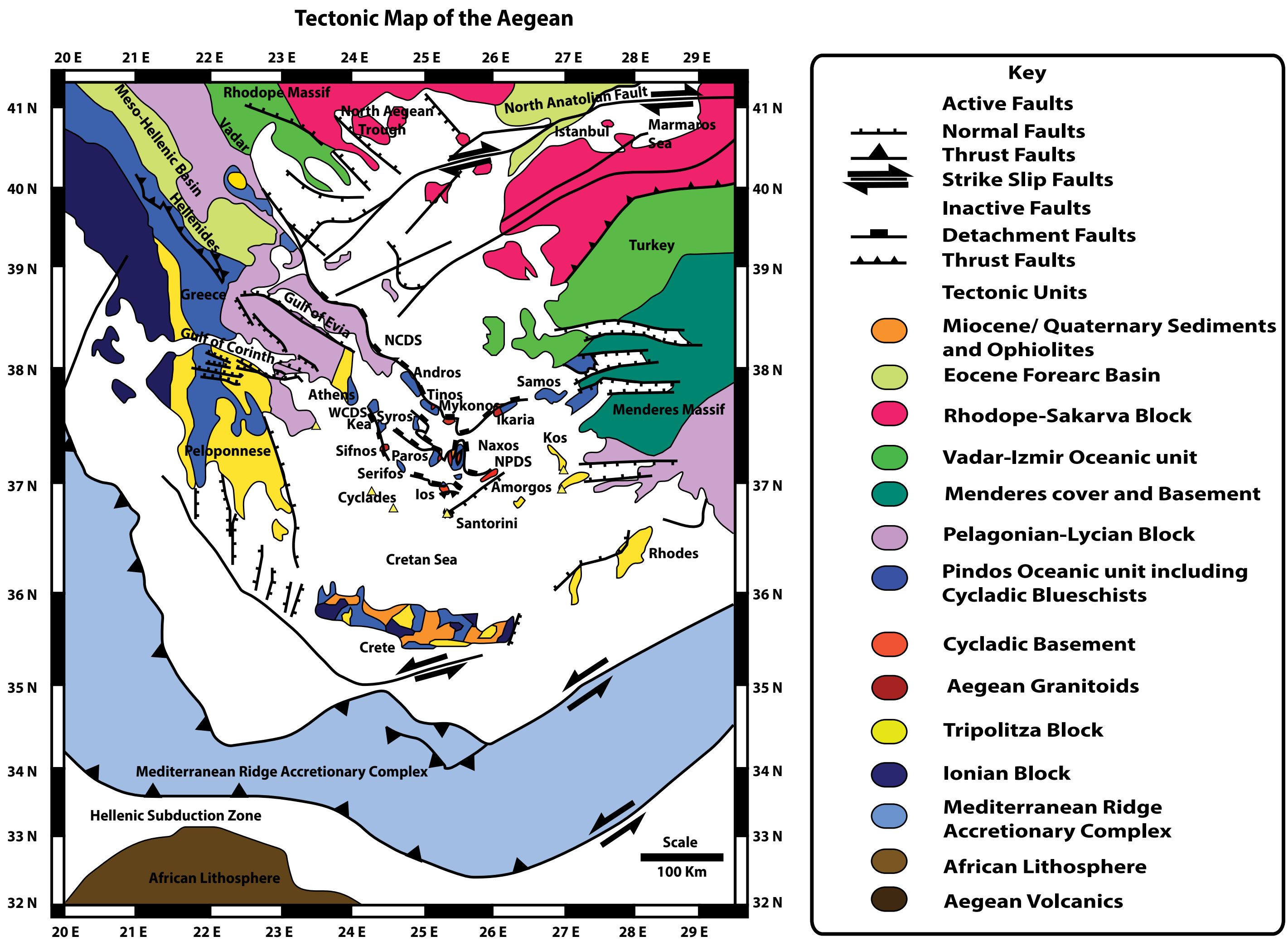

Figure 2. Simplified tectonic map of the Aegean region, after Jolivet et al. (2013), showing the major tectonic structures and rock types. Naxos lies in the Cycladic-Attic Massif in the central Cyclades. NCDS—North Cycladic detachment system; NPDS—Naxos-Paros detachment system; WCDS—West Cycladic Detachment System; yellow triangles—current Hellenic volcanic arc.

deepest structural levels of the Attic-Cycladic Massif, which experienced high-grade metamorphism, anataxis, and leucogranite formation during the Miocene. This study documents the pre-extensional, prograde, and retrograde history of the Naxos core complex and links the timing of kyanite- and sillimanite-grade Barrovian-type metamorphism to the prevailing tectonic regime. A future study will present the absolute ages of both compressional and extensional microstructures, which were constrained via in situ U-Th-Pb isotope geochronology performed on zircon, monazite, allanite, xenotime, and rutile. Finally, we assessed various tectonic scenarios to explain the history of Naxos prior to extension, and we conclude that the core complex formed due to prolonged compression, crustal thickening, and heating prior to the switch to extension in the late Miocene.

GEOLOGICAL SETTING

Regional Geology

The MCCs of the central Aegean region form part of the Attic-Cycladic Massif (Durr et al., 1978), which is a belt of thinned continental crust located to the north of the Hellenic subduction zone, where the Nubian plate is subducting northward beneath Eurasia (Wortel and Spakman, 2000; Jolivet and Brun, 2010). Within this subduction setting, the region can be subdivided into the forearc (Crete, Karpathos, Rhodes), the Hellenic arc (Santorini, Milos), and the back arc (Cyclades), which is reported to have experienced lithospheric extension in response to retreat of the Hellenic slab (Le Pichon and Anglier, 1979, 1981; Le Pichon et al., 2002; Jolivet et al., 2010, 2013, 2015).

Many studies have documented extension affecting the area from the Miocene until present day, and some estimate southward propagation of the Hellenic subduction zone on the order of 1000 km over this time period (John and Howard, 1995; Seward et al., 2009). It is estimated that NE-SW–oriented crustal extension rates within the last 15 m.y. may be up to twice as fast as present-day rates (Urai et al., 1990; Jolivet et al., 2001, 2004). In response to extension, three bivergent, crustal-scale, low-angle normal fault systems developed. The North Cycladic Detachment System (NCDS), exposed on the islands of Andros, Tinos, and Mykonos, displays top-to-the-NE sense of shear (Jolivet et al., 2010). The Naxos-Paros Detachment System (NPDS), exposed on Naxos and Paros, displays top-to-the-NNE shear fabrics (Buick, 1991a, 1991b; Cao et al., 2013, 2017; Urai et al., 1990;

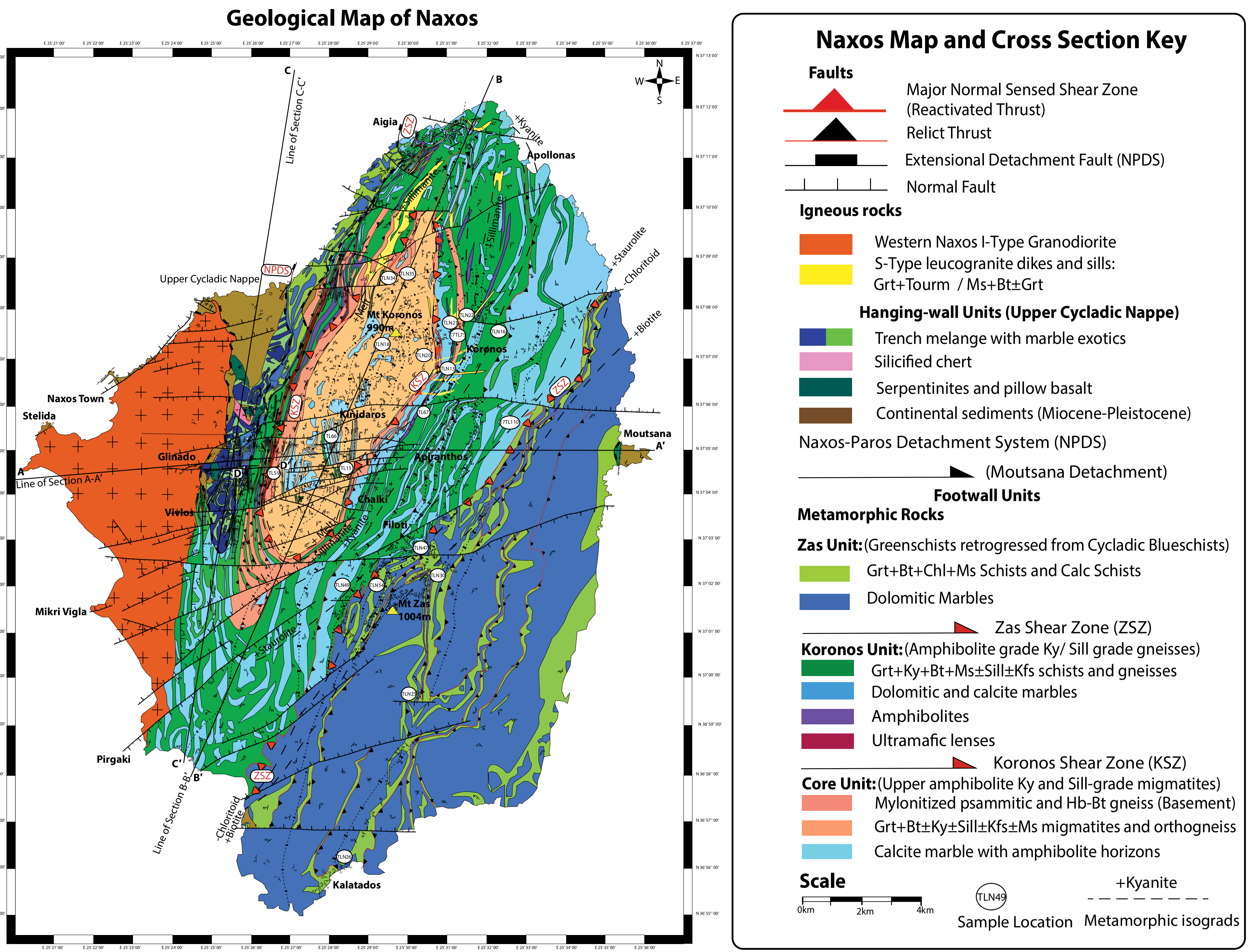

Figure 3. New geological map of Naxos metamorphic core complex, following previous mapping after Jansen (1973), Jansen and Schuiling (1976), Buick (1991a, 1991b), Urai et al. (1990), Vanderhaeghe (2004), and Kruckenberg et al. (2011). Major tectonic units within the metamorphic footwall include the Zas Unit (retrogressed Cycladic Blueschists), Koronos Unit (amphibolite-facies shelf carbonates), and Core Unit (upper-amphibolite-facies gneisses and migmatites). See text for more discussion and interpretation. Lines of sections A–A′, B–B′, C–C′, and D–D′ are presented in Figures 4 and 7. Mineral abbreviations follow Whitney and Evans (2010).

Kruckenberg et al., 2010, 2011). The West Cycladic Detachment System occurs on the islands of Kea, Kythnos, and Serifos and shows top-to-the-SSW kinematics (Grasemann et al., 2012).

Despite extensional deformation affecting all structural levels, little is known about the geological evolution of the area prior to the initiation of extensional tectonics. Structural and metamorphic evidence from several islands suggests that the Cyclades experienced a complete cycle of mountain building (Ring and Layer, 2003; Ring et al., 2007a, 2007b; Peillod et al., 2017). Remnant ophiolites crop out at the highest level on several islands, in the hanging walls of the low-angle normal faults (Stouraiti et al., 2017). These are underlain by (M_1) Eocene high-pressure eclogite- to blueschist-facies rocks of the Cycladic Blueschists in the footwalls of the detachments, dated at 52.2–51.4 Ma by U-Pb zircon and Lu-Hf garnet geochronology from Syros (Tomaschek et al., 2003; Lagos et al., 2007) and at ca. 46 Ma from Sifnos eclogites (Dragovic et al., 2012). The area then experienced regional Barrovian metamorphism (M_2) during the Oligocene to early Miocene (40–18 Ma), followed by a sillimanite-grade event (M_3) at ca. 16 Ma that reached anatectic conditions on Naxos and Ios (Jansen and Schuiling, 1976; Buick and Holland, 1989; Keay et al., 2001). Within the high-grade dome of the Naxos core complex, there is evidence for NNE-SSW extensional fabrics coeval with M_3 conditions (Ring et al., 2007b), indicating a switch in tectonic regime during this period. Understanding the timing of this switch from compression to extension is fundamental to understanding the formation of the Aegean MCCs.

Geology of Naxos

Naxos is the largest island in the Cyclades and shows evidence for having experienced multiple tectono-metamorphic events (see Figs. 3 and 4). It is composed of a NNE-SSW–elongated dome in the exhumed footwall of a major low-angle normal fault, the NPDS, which developed in response to regional Aegean extension (Cao et al., 2013, 2017). The hanging wall mainly consists of ophiolitic rocks with a mélange of disrupted Miocene–Pliocene sediments (Jansen, 1973), which are possibly synextensional (Urai et al., 1990; Gautier and Brun, 1994a, 1994b). Upper Pliocene conglomerates containing pebbles of footwall material were deposited on the flanks of the dome during unroofing (Lister et al., 1984; Buick, 1991a, 199b; Gautier and Brun, 1994a, 19914b). The lower unit represents a Barrovian-type metamorphic sequence that developed during M_2 (Jansen, 1973; Jansen and Schuiling, 1976; Buick and Holland, 1989; Buick, 1991a, 1991b; Urai et al., 1990), reaching upper-greenschist facies in the east (biotite zone: ~5 kbar and ~400 °C) and overprinting relict (M_1) blueschist assemblages along the southeast coastline (Avigad, 1998; Peillod et al., 2017), and reaching upper-amphibolite (M_3) anatectic conditions in the core (sillimanite zone: ~7 kbar and ~700 °C). In the west, an I-type granodiorite pluton with a U-Pb age of ca. 12.2 Ma intrudes the metamorphic sequence and developed a narrow metamorphic aureole (M_4; Keay et al., 2001; Koukouvelas and Kokkalas, 2003; Jansen and Schuiling, 1976).

The core region consists of highly strained M_3 sillimanite-bearing migmatites and gneisses, with intercalated marbles and leucogranites, which are separated from a lower-grade deformed sequence of Mesozoic shelf carbonates by a major ductile shear zone, forming the carapace (the attenuated metamorphic sequence structurally above the migmatite core) to the migmatite dome. Top-to-the-NNE kinematic indicators are associated with this ductile shear zone, which formed during exhumation of the core complex. Due to this complex deformation and metamorphic history, the development of most of the footwall structures and fabrics is poorly understood, and there is confusion as to whether they formed during crustal extension or predate the extensional movements and were reactivated by them (Ring et al., 2007b). Recent work has shown that the blueschist rocks on southeast Naxos experienced a contrasting metamorphic history to the underlying higher-grade rocks (Peillod et al., 2017), and there has been confusion about whether the entire island experienced (M_1) blueschist-facies conditions or whether there are discrete tectono-stratigraphic units. Furthermore, the cause of regional M_2 and M_3 kyanite-sillimanite–grade metamorphism, the pre-extensional, prograde evolution of the core complex, and the relative timing of peak metamorphism in relation to the onset of extension have remained controversial. Two contrasting models have been proposed for the initiation of extension. Wijbrans et al. (1993) and Parra et al. (2002) argued that extension commenced at 30 Ma (see also Jolivet et al., 2003) due to slab roll-back, followed by M_2 heating of the Cycladic blueschists (Bröcker and Franz, 1998). Alternatively, others argued for the concept of synorogenic extension during underthrusting and compression in the Cyclades until 21 Ma, followed by postorogenic extension and crustal thinning (Peillod et al., 2017; Ring and Layer, 2003; Ring et al., 2007a, 2007b, 2010).

Competing models have been proposed to explain the decompression of migmatites and the formation of the doubly plunging migmatite dome making up the core of Naxos. These include diapirism (Jansen and Schuiling, 1976; Vanderhaeghe, 2004), exhumation during regional extension (Gautier and Brun, 1994b), and superimposed folding from E-W shortening followed by top-to-the-NNE shearing (Urai et al., 1990; Buick, 1991a, 1991b), as well as a combination of buoyancy- and isostasy-driven flow during crustal extension (Kruckenberg et al., 2011). This study presents a systematic characterization of the tectonic and metamorphic evolution of Naxos that addresses the role of compressional and extensional tectonics in formation of the core complex.

FIELD RELATIONSHIPS

Geological mapping was carried out (Figs. 3 and 4), building on previous detailed work (e.g., Jansen and Schuiling, 1976; Buick, 1991a, 1991b; Buick and Holland, 1989; Urai et al., 1990; Vanderhaeghe, 2004; Kruckenberg et al., 2011), but with new and important structural interpretations (Figs. 4–10). In this section, we describe each tectono-stratigraphic unit in descending structural order and discuss the major fabrics, folds, and mineral growth (Figs. 4–10) in relation to the deformation.

Tectono-Stratigraphy

Zas Unit (Retrogressed Cycladic Blueschists)

Retrogressed blueschists exposed in the SE corner of the island (Avigad, 1998) represent the highest structural level of the metamorphic carapace. These are composed of (M_1) blueschist- and (M_2) greenschist-facies rocks derived from proximal to distal shelf and slope metasediments including turbidites, dolomitic marbles, pelites, meta-conglomerates, and metavolcanics. The existence of deeper-sea clays is indicated by piemontite-bearing schists, which together have similarities to the Cycladic Blueschist Unit exposed on Syros, Ios, Andros, and Tinos. Additional exposures of blueschist-facies assemblages can be found toward the top of the sequence, spanning the entire eastern coastline (see Figs. 3 and 4). Within this unit, there are two types of top-to-the-NNE extensional shear fabrics. S_1 is defined by blueschist-facies assemblages including glaucophane, phengitic mica, and paragonite that are preserved within only partially retrogressed high-pressure boudins, bearing many similarities to the fabric seen throughout the Cycladic Blueschist Unit. This extensional fabric is associated with synorogenic extrusion from a NE-dipping subduction zone during the Eocene by synorogenic passive-roof normal faults such as the Vari detachment on Syros and Sifnos (e.g., Ring et al., 2003; Roche et al., 2016; Laurent et al., 2016).

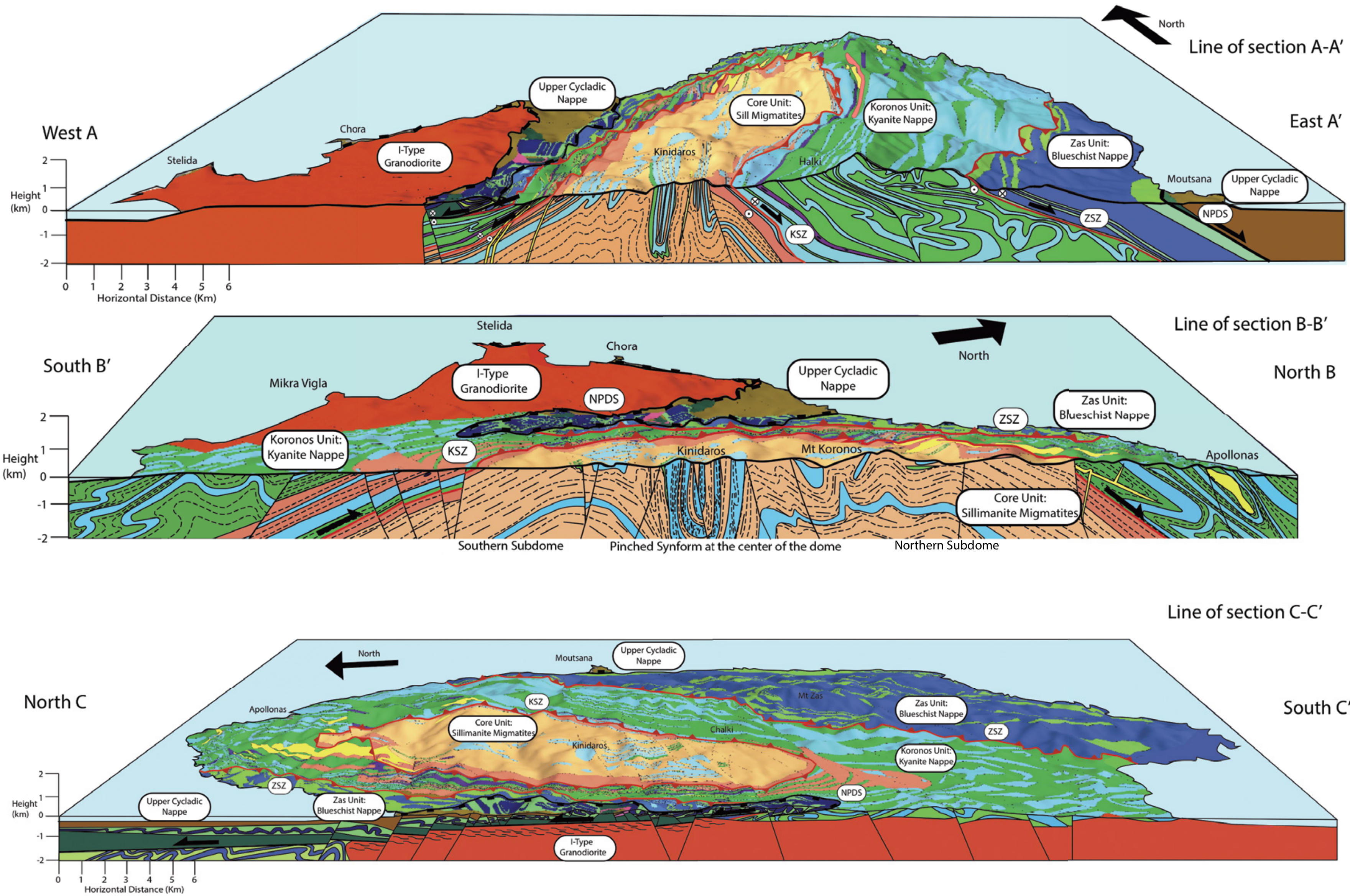

Figure 4. Three-dimensional models of the Naxos metamorphic core complex illustrating structural and crosscutting relationships, produced using the QGIS plugin 2threejs with superimposed cross section, scale 1:1, using same color scheme for geological units as in Figure 3. NPDS—Naxos-Paros detachment system; ZSZ—Zas shear zone; KSZ—Koronos shear zone.

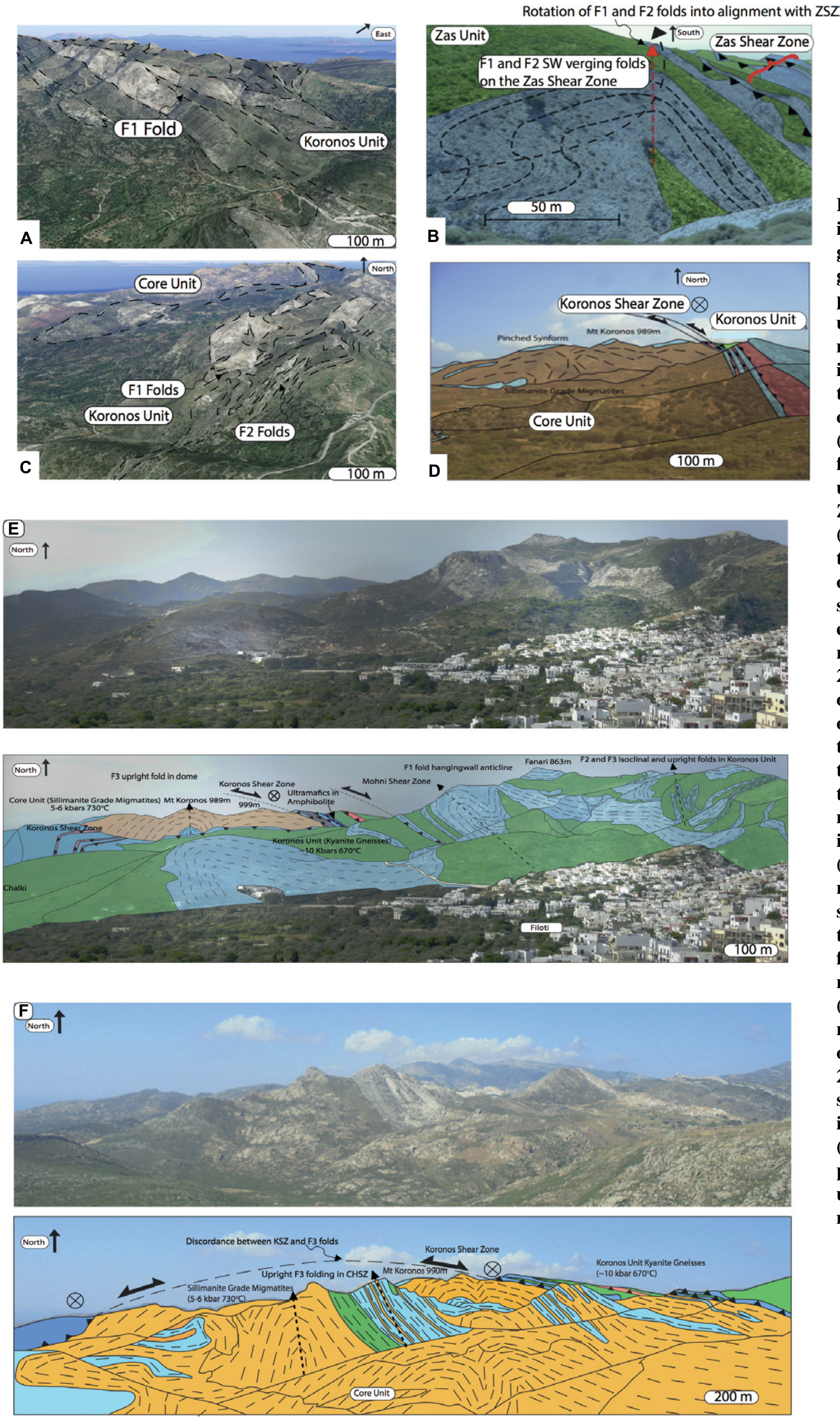

Figure 5. Panoramic photos of folding styles on Naxos (color scheme: green—schist, blue—marble, pink—gneiss, tan—migmatite, purple—amphibolite). (A) Google Earth imagery using three-dimensional (3-D) view mode to show an F_1 NE-SW–verging recumbent isoclinal fold within the Koronos Unit north of the town of Filoti (37.066816°N, 25.507647°E). (B) F_1 and F_2 isoclinal and sheath folding on the Zas shear zone under the western flank of Mount Zas (37.031232°N, 25.497227°E). (C) Google Earth 3-D view of intense F_1 and F_2 folding to the east of Filoti, illustrating the F_2 isoclinal sheath-type folds superimposed on early F_1 NE-SW–trending isoclinal recumbent folds (37.057519°N, 25.504086°E). (D) Annotated and overlaid field sketch of the interior of the migmatite dome and the mantling Koronos shear zone (KSZ) on the eastern margin of the migmatite dome, showing the repetition of marble bands due to intense shearing (37.092747°N, 25.493531°E). (E) Panoramic photograph and annotated photograph of the folding styles within the Koronos Unit and their contrast to the underlying F_3 folds within the Core Unit looking north (37.042451°N, 25.498678°E). (F) Panoramic photograph and annotated photograph from the top of Apano Kastro (37.066894°N, 25.459924°E), showing the interior structure of the migmatite dome, including the Core high-strain zone (CHSZ), marked by vertically dipping marble bands representing tight upright F_3 folds at the center of the migmatite dome.

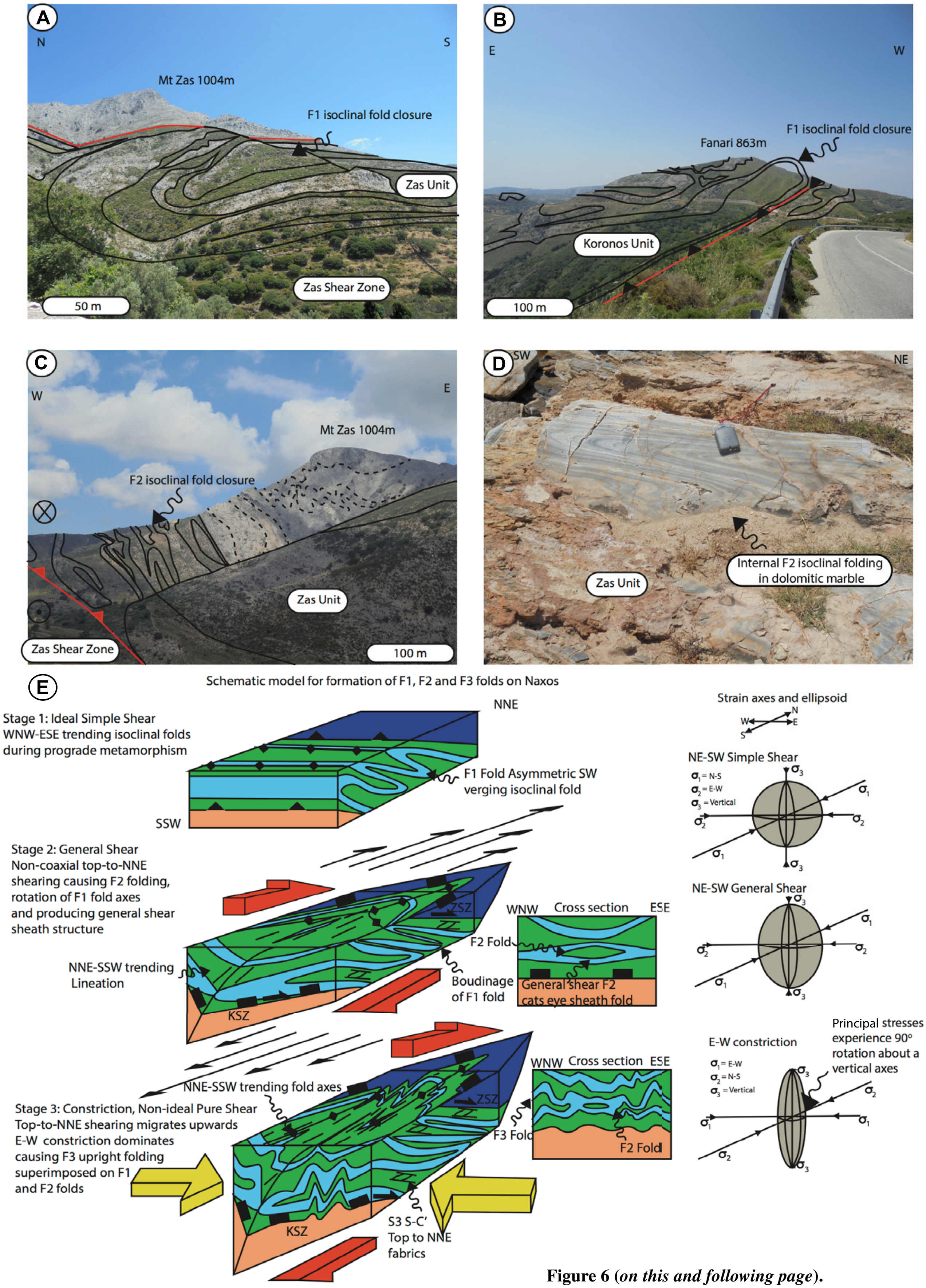

Figure 6 (*on this and following page*).

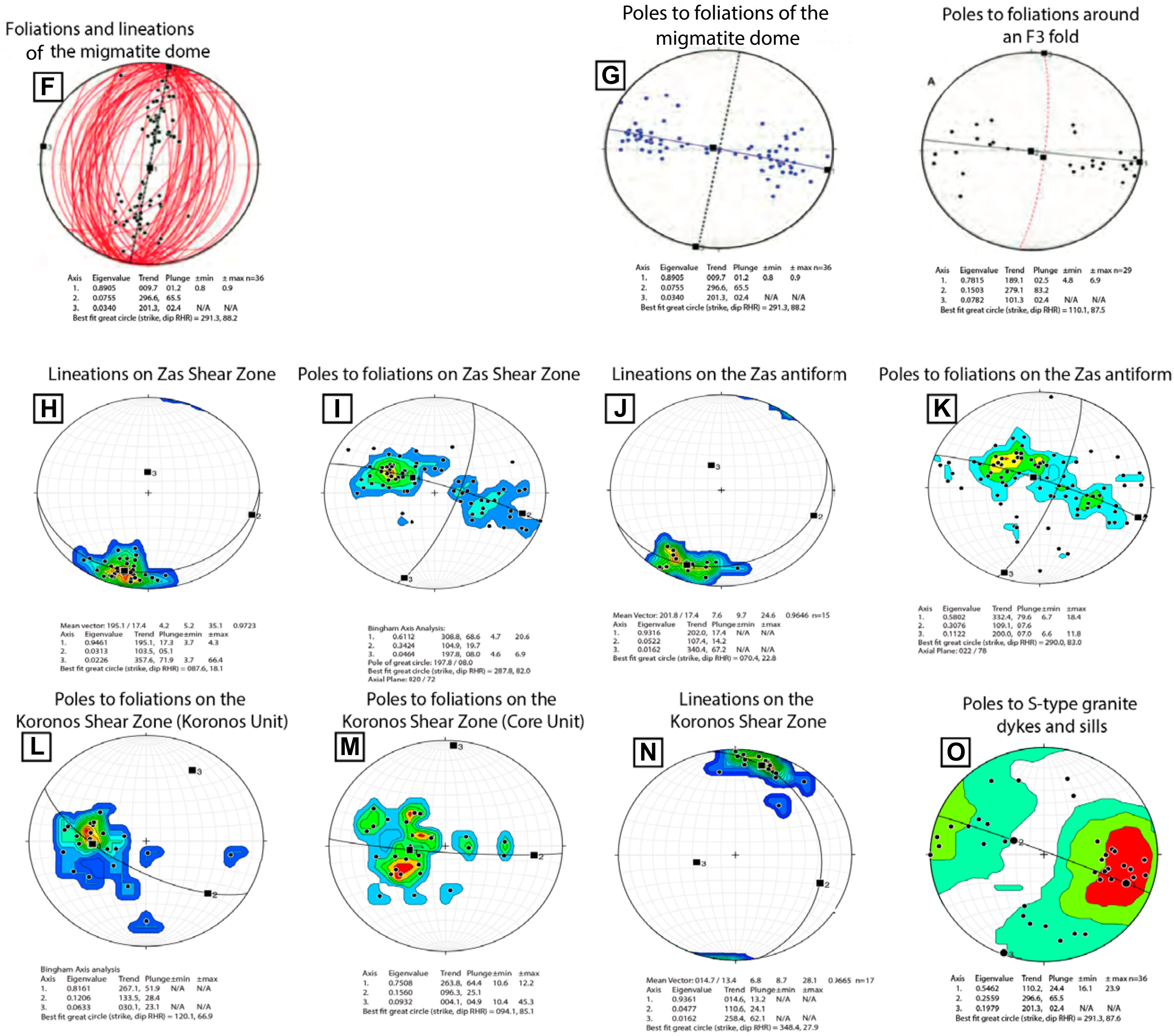

Figure 6 (*continued*). Mesoscale annotated photographs of the folding geometries within the metamorphic carapace and schematic model to explain their structural relationships. (A) Boudinaged F_1 isoclinal fold closures of marble bands within the Zas shear zone (ZSZ) under the western flank of Mount Zas (37.035727°N, 25.495403°E). (B) Overview of folding geometries crosscutting Fanari (863 m; N37.107506°N, E25.527892°E), showing late upright F_3 folds superimposed on early recumbent and isoclinal folds. (C) Panorama looking north along strike of the ZSZ, showing tight F_2 isoclinal folds overprinting the limbs of F_1 folds, with the western face of Mount Zas to the right of the image (37.013864°N, 25.480907°E). (D) Internal isoclinal folding within dolomitic marble of the Zas Unit near Kalatados Bay (36.935074°N, 25.468323°E), the limbs of which are detached following ductile shearing. (E) Schematic cartoon showing the development of F_1, F_2, and F_3 folds on Naxos. Stage 1—NE-SW–verging isoclinal folds form during the prograde evolution. Stage 2—Non-coaxial top-to-the-NNE general shearing initiates and produces F_2 folds that overprint the limbs of F_1 folds, and sheath-type structures develop with "cat's-eyes." Stage 3—Rotation of principal stress axes causes late-stage E-W constriction to produce E-W–trending open to tight folds. KSZ—Koronos shear zone. See text for more discussion. (F–K) Lower-hemisphere equal-area stereonets of structural data from the Zas, Koronos, and Core Units: (F) Foliations of the migmatite southern subdome demonstrating a symmetric morphology to the dome. (G) Poles to foliations of the migmatite dome southern subdome, demonstrating its upright symmetrical and doubling plunging nature along a NNE-SSW axis, and poles to foliations of an F_3 fold within the Koronos Unit, highlighting its upright and isoclinal nature with a fold axes trending: 189°, 83°. (H) Lineations on the ZSZ, with mean lineation: 195.4°, plunge 17.4°. (I) Poles to foliations on ZSZ, with best-fit great circle: 020°, 78°. (J) Lineations on the Zas anticline on the western flank of Mount Zas, with mean lineation: 201.8°, 17.4°. (K) Poles to foliations on the Zas anticline, with best-fit axial plane: 022°, 78°. (L) Poles to foliation for Koronos Unit, with best-fit great circle: 120.1°, 66.9°. (M) Poles to foliations for Core Unit from KSZ, with best-fit great circle: 094.1°, 84.1°. (N) Lineations on the northern segment of the KSZ, with mean lineation: 014.7°, 13.4° plunge. (O) Poles to S-type granite dikes and sills emanating from the migmatite dome. On the eastern side of the Core Unit, granite dikes dip to the west and crosscut the KSZ shear fabric, and in the center of the Core Unit, dikes dip vertically, whereas on the western side of the dome, they rotate into alignment with the Naxos-Paros detachment system foliation and strike subparallel with the lineation.

Pelitic horizons have highly strained contacts with dolomitic marbles that preserve internal folding and centimeter-scale crenulation cleavage (S_{2a}). These are overprinted and truncated by a subparallel, highly localized extensional S-C′ shearing fabric (S_3), exclusively defined by greenschist-facies assemblages. The intensity of shearing increases toward the boundaries of the unit, where major normal-sense shear zones, the Moutsana detachment and Zas shear zone (ZSZ) (Fig. 7), have developed. Along these shear zones, some discontinuous horizons of serpentinite enclaves crop out (Katzir et al., 1999, 2002, 2007), which are also affected by the (S_3) extensional foliation. These are interpreted as fragments of serpentinized mantle from the overlying ophiolitic thrust sheet that where incorporated at low temperature during extensional shearing (S_3).

Figure 7 (*on following page*). Representative outcrop photographs of key features from the Upper Cycladic Nappe and Naxos-Paros detachment system (NPDS), with small-scale cross section through the NPDS. (A) Silicified and altered pillow basalt from the trench mélange within the Upper Cycladic Nappe (37.075998°N, 25. 416638°E). (B) Exotic marble cataclasite within the trench mélange, marked by pink coloring, diagnostic of piemontite (manganese epidote) representing interlayered distal oceanic oozes (37.077357°N, 25.420516°E). (C) Outcrop of serpentine cataclasite and fault breccia and blocks from the brittle Moutsana detachment of the NPDS (37.071605°N, 25.416424°E). (D) Ultramylonitized dolomitic marble of the Zas Unit directly under the Moutsana detachment on west Naxos (37.070526°N, 25.415716°E), 50 m from photo C. (E) Brittle cataclasite and fault gouge of dolomitic marble from the Zas Unit against brecciated serpentinites of the Upper Cycladic Nappe, separated by the Moutsana detachment (37.079374°N, 25.428907°E). (F) S-type leucogranite sills intruding syntectonically into the NPDS ductile shear zone on NW Naxos (37.183128°N, 25.506907°E). (G) Simplified cross section through the NPDS on western Naxos representing extreme telescoped isograds with metamorphic field gradients of up to 700 °C km^{-1}. Outcrop photos are projected into the line of section. (H) Lineations of mylonites from the Moutsana detachment, with mean lineation: 011.4°, 10.1° plunge. (I) Rose diagram of slickenslides along normal faults in the hanging wall of the Moutsana detachment, with most faults slipping on ESE-WNW–trending or ENE-WSW–trending planes. (J) Poles to foliations of mylonites from the Moutsana detachment, western Naxos, with best-fit great circle, representing a synform with its hinge line striking 012° and plunging at 14° to the NNE, which formed due to late-stage E-W shortening.

Koronos Unit (Kyanite-Grade Mesozoic Shelf Carbonates)

The Koronos Unit is a 4-km-thick metasedimentary sequence of intercalated marble and schists that represents a proximal Mesozoic shelf carbonate cover to the Cycladic basement (Durr et al., 1978; Andriessen et al., 1979). This unit is characterized by M_2 amphibolite-facies Barrovian metamorphic rocks, in contrast to the overlying Zas Unit. In coarse-grained dolomitic marbles at the top of the unit, corundum (emery) and magnetite horizons represent paleosols that formed during sedimentation and subaerial exposure of the continental margin during the Jurassic (Altherr et al., 1982). Within the succession, meter-scale amphibolite bodies trend parallel to the regional foliation and represent doleritic sills that intruded along bedding prior to burial and metamorphism. M_2 kyanite gneisses, marbles, and schists crop out at the deepest levels, and the metamorphic grade dramatically decreases up structural section to staurolite and garnet grade. At the base of this unit, slices of continental basement are exposed and are structurally repeated in a sequence overlying semipelitic schists and marbles of the shelf carbonate sequence. This indicates structural repetition of the shelf sequence, which could only be achieved by thick-skinned thrusting of the shelf and basement over more-proximal continental shelf metasediments. Garnet- and clinopyroxene-bearing amphibolites outcrop 100 m below this horizon, within the metasedimentary sequence, as a semicontinuous layer along strike. These enclose partially serpentinized peridotite lenses (Katzir et al., 2002, 2007) that remained stronger during deformation as the amphibolites flowed and deformed around them during top-to-the-NNE ductile shearing (see Fig. 7). The intensity of top-to-the-NNE shearing within the unit increases toward the base, where the Koronos shear zone (KSZ) separates this unit from the underlying migmatites.

Core Unit (Kyanite- to Sillimanite-Grade Migmatites)

The Core Unit is composed of M_2 kyanite-grade to M_3 sillimanite-grade migmatites, gneisses, and leucogranites, which make up the deepest levels of the core complex. The first-order dome structure contains second-order subdomes (Kruckenberg et al., 2011), which are separated by a high-strain zone (Core High-Strain Zone [CHSZ]) of tight upright and isoclinally folded marbles, amphibolites, and migmatites that have been subsequently boudinaged. The Core Unit is separated from the overlying carapace by the KSZ along the dome margins (see below; Figs. 4 and 5). Within the anatectic core, the extent of partial melting varies with bulk composition, as well as with increasing metamorphic grade. There is lithological variation throughout the migmatite zone, with banded leucocratic gneisses representing continental basement commonly interleaved between pelitic and semipelitic protoliths and marbles of the shelf carbonate cover sequence. This structural repetition in lithology again provides further evidence for thick-skinned ductile thrusting and imbrication of the shelf-basement contact during crustal thickening. Stromatic migmatites (Fig. 9), representing the first appearance of melt, outcrop along the perimeter of the dome or adjacent to metasedimentary rafts and are characterized by a continuous foliation marked by alternating quartzofeldspathic and biotite layers with distinct leucosomes and melanosomes (see also Kruckenberg et al., 2011). Leucosomes occur along the foliation marked by biotite, muscovite, and kyanite in aluminum-rich domains, increase in abundance with depth, and become concentrated in fold hinges, where they display magmatic textures. Leucosomes also occur in boudin necks and in shear bands that crosscut compositional layering (S_0). At deeper structural levels, both coarse quartzofeldspathic horizons and pockets of melt are ptygmatically folded, with melt distributed along fold hinges, indicating it accumulated in dilatant structural sites during compression (Brown, 2002; Sawyer, 2001; Holness, 2008). Where evidence of melting becomes locally more extensive, particularly in pelitic horizons, diatexites are characterized by magmatic textures containing enclaves of the host rocks, and they are heterogeneous at outcrop and thin section scales. They include schollen, and schlieren-structured varieties (Fig. 9) with a magmatic foliation defined by schlieren of biotite or alignment of schollen (see also Kruckenberg et al., 2011). Although these features can be locally extensive, our observations and data reveal they are not as widespread as Kruckenberg et al. (2011) implied. We suggest that most of the gneisses previously described as diatexites are instead granitic basement with Variscan metamorphic ages (presented in a future study). Although some diatexites do locally occur, they are confined to fertile lithologies upon crossing the K-feldspar isograd at the deepest levels of the migmatite dome.

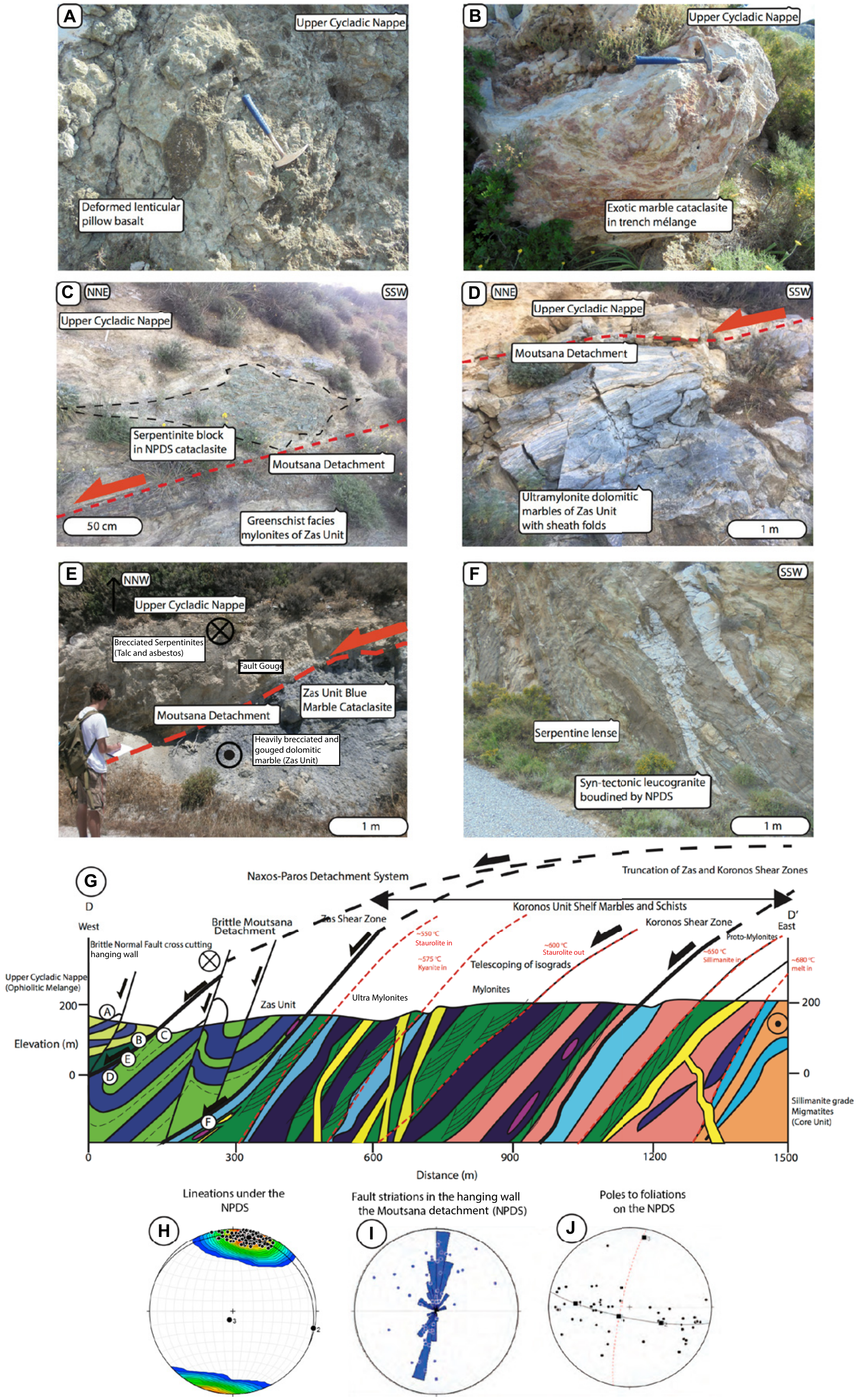

A
Upper Cycladic Nappe
Deformed lenticular pillow basalt
B
Upper Cycladic Nappe
Exotic marble cataclasite in trench mélange
C
NNE
SSW
Upper Cycladic Nappe
Serpentinite block in NPDS cataclasite
Moutsana Detachment
50 cm
Greenschist facies mylonites of Zas Unit
D
NNE
SSW
Upper Cycladic Nappe
Moutsana Detachment
Ultramylonite dolomitic marbles of Zas Unit with sheath folds
1 m
E
NNW
Upper Cycladic Nappe
Brecciated Serpentinites (Talc and asbestos)
Fault Gouge
Zas Unit Blue Marble Cataclasite
Moutsana Detachment
Heavily brecciated and gouged dolomitic marble (Zas Unit)
1 m
F
SSW
Serpentine lense
Syn-tectonic leucogranite boudined by NPDS
1 m
G
Naxos-Paros Detachment System
Truncation of Zas and Koronos Shear Zones
Koronos Unit Shelf Marbles and Schists
D
West
D'
East
Brittle Moutsana Detachment
Zas Shear Zone
Koronos Shear Zone
Proto-Mylonites
Brittle Normal Fault cross cutting hanging wall
~550 °C Staurolite in
~575 °C Kyanite in
~600 °C Staurolite out
~650 °C Sillimanite in
~680 °C melt in
Telescoping of isograds
Upper Cycladic Nappe (Ophiolitic Melange)
Zas Unit
Ultra Mylonites
Mylonites
200
0
Elevation (m)
Sillimanite grade Migmatites (Core Unit)
0
300
600
900
1200
1500
Distance (m)
H
Lineations under the NPDS
I
Fault striations in the hanging wall the Moutsana detachment (NPDS)
J
Poles to foliations on the NPDS

Figure 7.

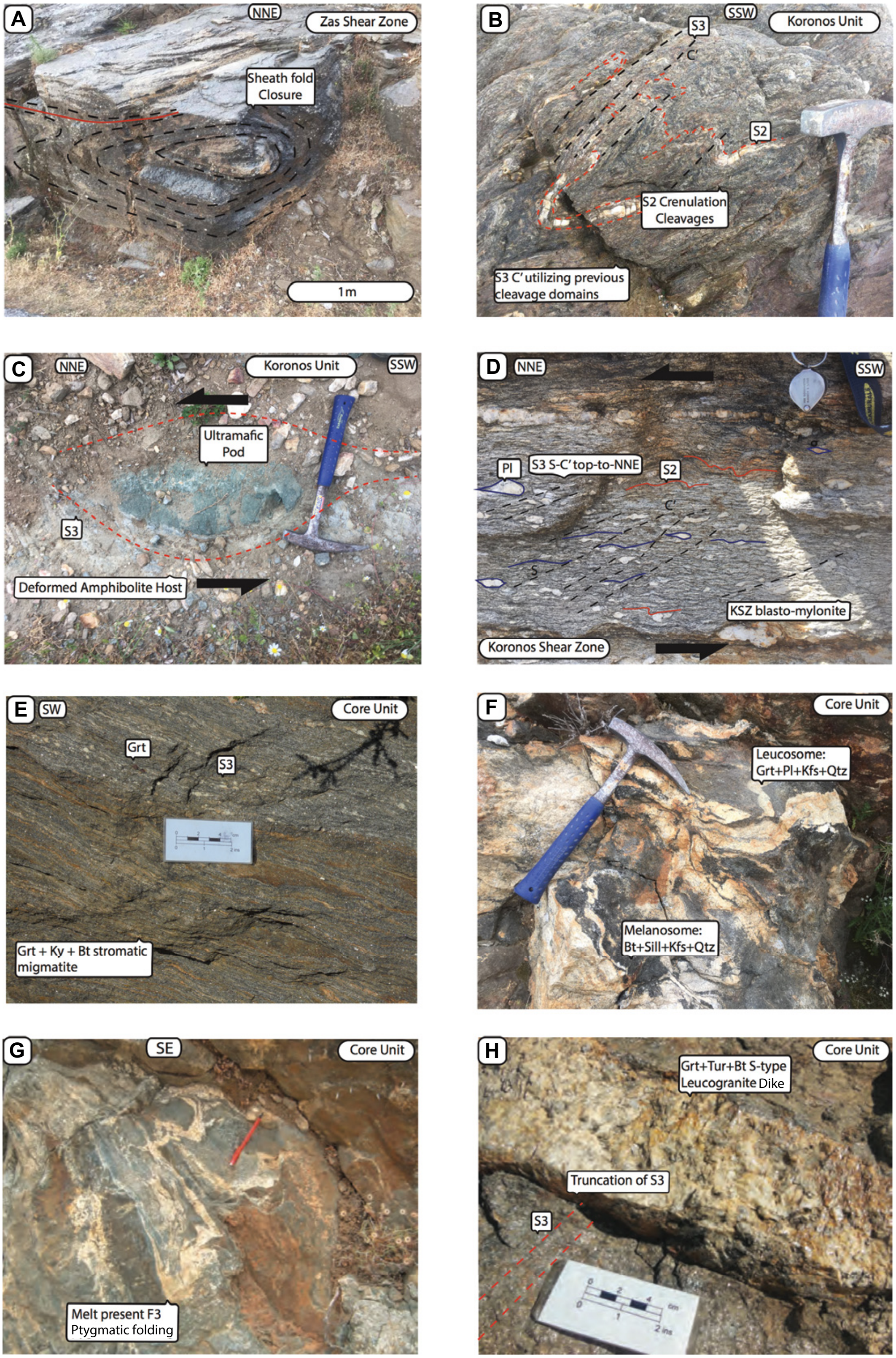

Figure 8. Representative field outcrop photographs from intermediate levels of the Naxos metamorphic core complex. (A) Cat's-eye sheath fold within the Zas shear zone (37.037370°N, 25.492597°E) indicative of non-coaxial general shear with fold hinge plunging to the NNE. (B) S_2 crenulation cleavages within micaceous schist from the Koronos Unit with S_3 C′ planes overprinting S_2 cleavage domains (36.932450°N, 25.429476°E). (C) Ultramafic partially serpentinized pod within host foliated amphibolite from the Main Ultramafic Horizon (Katzir et al., 1999, 2002, 2007), directly structurally above the Koronos shear zone (KSZ), also characterized by top-to-the-NNE shear fabrics (37.104116°N, 25.510806°E). (D) Blastomylonite basement gneiss from the KSZ (37.047572°N, 25.455538°E) displaying diagnostically S-C and S-C′ top-to-the-NNE kinematic indicators and quartz rods that form σ and δ porphyroclasts with consistent shear senses. Pl—plagioclase. (E) Foliated kyanite-grade stromatic migmatite from the perimeter of the migmatite dome (37.060807°N, 25.452099°E) showing coarsening textures and representing the first appearance of partial melt. (F) Diatexite migmatite marked by extensive melting destroying all previous fabrics, characteristic of fertile lithologies and locally extensive anatexis (37.090701°N, 25.460878°E). (G) Ptygmatically folded partial melt indicative of contractional deformation in the presence of extensive melting (37.091540°N, 25.459035°E). (H) Garnet + tourmaline + biotite leucogranite sill crosscutting the extensional top-to-the-NNE S_3 shear fabric at the perimeter of the migmatite dome (37.067065°N, 25.447091°E). Mineral abbreviations follow Whitney and Evans (2010).

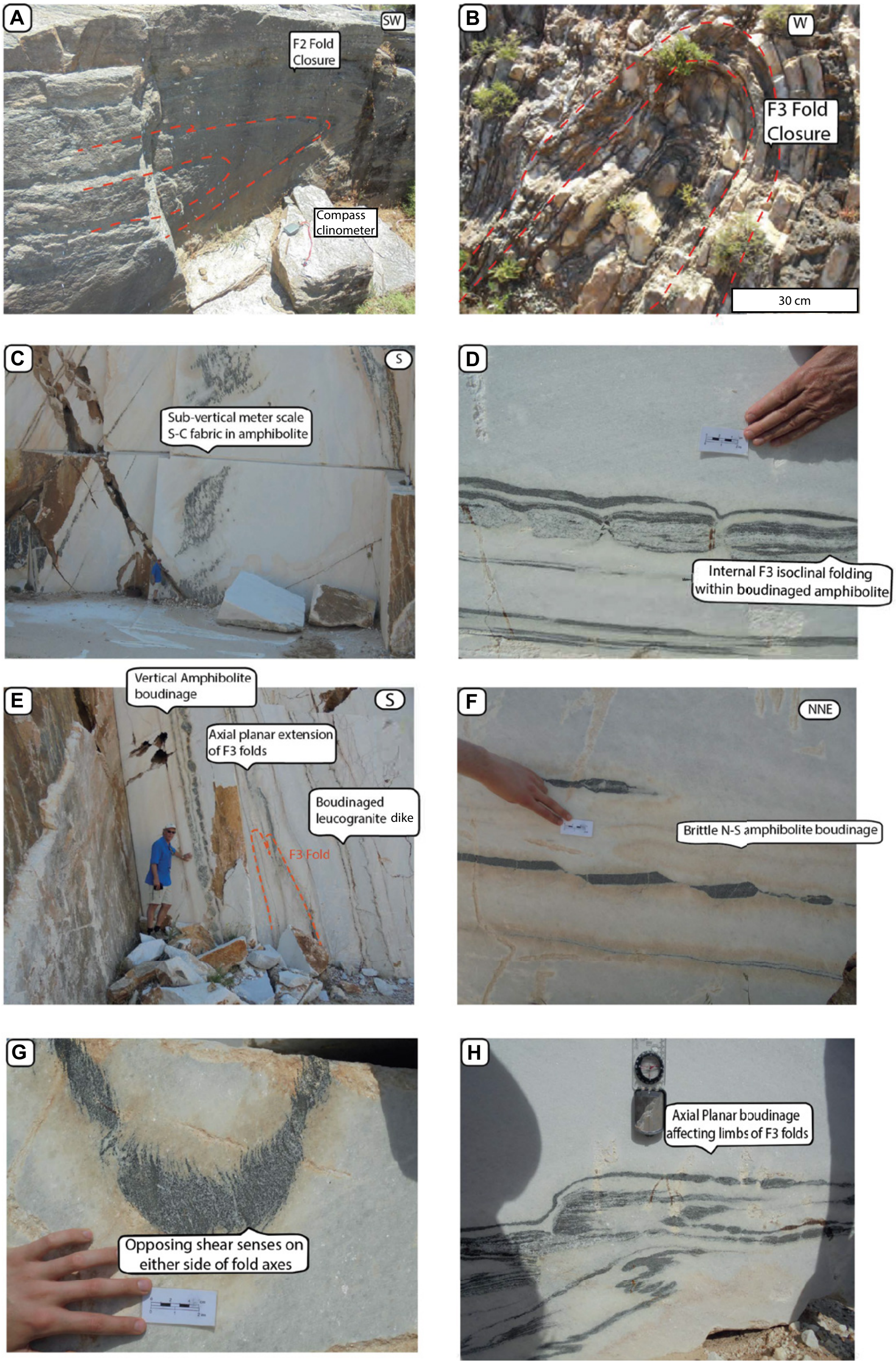

Figure 9. Outcrop photographs of characteristic deformation from deep levels of the core complex. (A) F_2 fold closure within graphitic schist of the Koronos Unit looking NNE (37.100354°E, 25.517359°E). (B) F_3 upright isoclinal fold closure trending NNE-SSW within the migmatite dome (37.095943°N, 25.468734°E). (C) Deformation within the Core high-strain zone (CHSZ; 37.106237°N, 25.482500°E), with subvertical meter-scale S-C fabrics in amphibolites that have been later boudinaged both vertically and horizontally in the N-S direction. (D) Horizontally boudinaged amphibolites and leucogranites from the Core high strain zone (37.107807°N, 25.482510°E), showing internal centimeter-scale isoclinal folds. (E) Upright folded amphibolites along NNE-SSW axes, with vertically boudinaged amphibolites and also a leucogranite dike diagnostic of horizontal constriction (37.108102°N, 25.483013°E) within the center of the Naxos migmatite dome. (F) Horizontal extension and boudinage indicated by amphibolites show ~50% pure shear and brittle simple shear in the amphibolites, with counterclockwise rotation. (G) S-C extensional fabrics overprinting F_3 folds of amphibolites, aligned axial planar with the vertical fold. (H) Extensional axial planar boudinage and shearing fabrics overprinting F_3 intensely and isoclinally folded amphibolites (37.107807°N, 25.482510E).

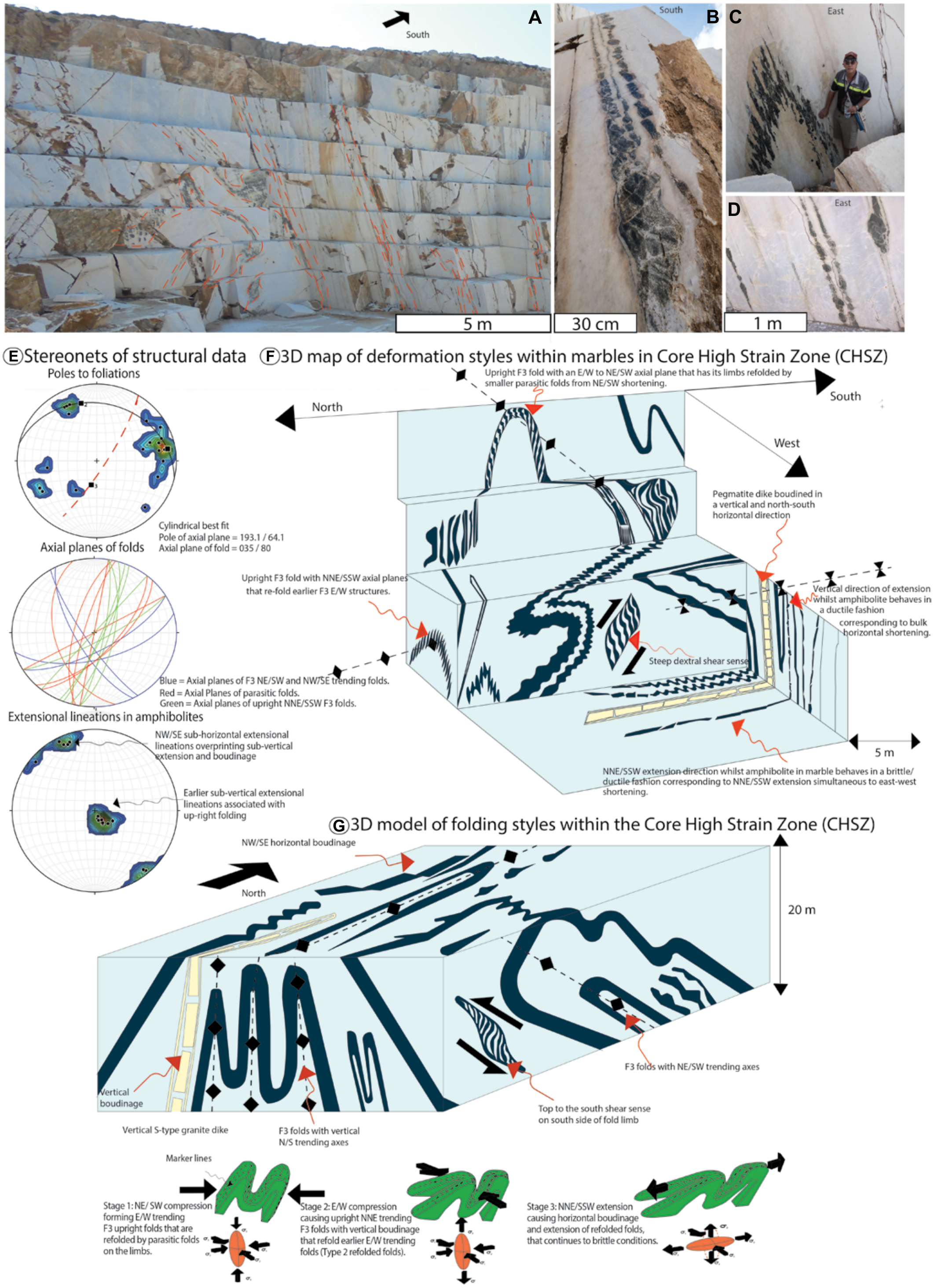

Figure 10. Core High-Strain Zone (CHSZ) at the center of the migmatite dome (37.108102°N, 25.483013°E). (A) Overview photograph showing the three-dimensional exposure of the Kinidaros Quarry and deformation in the CHSZ. (B) Vertical ductile boudinage of amphibolites, with a domino-style more brittle overprint. (C) Upright E-W–trending F_3 fold with vertical boudinage overprinting its limbs. (D) Pinch-and-swell boudinage affecting limbs of an E-W–trending F_3 fold. (E) Stereonets of structural data displaying poles to foliations, axial planes of folds, and extensional lineations. Note that the intersections of axial planes of folds represent an overall vertically orientated sheath fold with bimodal vertically and NNW-SSE–orientated stretching lineations and boudinage. (F) Three-dimensional map of deformation within the CHSZ, highlighting the structural superposition of three fold generations in relation to the intrusion of a leucogranite dike and vertical and horizontal stretching. Note that dike intrusion postdates all folding and predates shearing and vertical and horizontal boudinage. (G) Three-dimensional block model of deformation structures within the CHSZ, where F_1 and F_2 isoclinal folding is overprinted by F_3 tight-isoclinal upright folds along NNE-SSW–trending axes.

Structures within the Metamorphic Core Complex

The large-scale structure of Naxos consists of a complex superimposition of three generations of kilometer- to meter-scale isoclinal and sheath folds, which are overprinted and truncated by a series of normal-sense shear zones (Jansen, 1973; Buick and Holland, 1989; Urai et al., 1990; Buick, 1991a, 1991b). Three-dimensional models, panoramic sketches, and accompanying interpretations are presented in Figures 4–6, while structural analyses of these folds and shear zones are displayed in Figures 6 and 7.

F_1 and F_2 Folds

Isoclinal, recumbent, and noncylindrical (F_1) folds occur mainly within the metamorphic carapace (Zas and Koronos Units), up to kilometer scale, and trend along NNE-SSW fold axes. They are characterized by subhorizontal hinge lines that strike parallel to the fold axes and display a SW vergence direction and hanging-wall anticline geometries above discrete detachments (e.g., on the western flank of Mount Zas; Figs. 5 and 6). The limbs of these folds are refolded by smaller tight to isoclinal, also NNE-SSW–trending (F_2) folds and sometimes produce an overall sheath fold–type geometry with their noses trending NNE-SSW, parallel to the lineation and shear direction, and these are particularly well developed along the ZSZ (Figs. 5, 6, and 8A). Sheath folds form by progressive rotation of fold hinges and are defined by curvilinear fold axes with more than 90° of curvature (Ramsay and Huber, 1987). They initially form as isoclinal folds with axes aligned orthogonal to shear and rotate toward the transport direction under progressive non-coaxial, high-strain deformation (e.g., Cobbold and Quinquis, 1980; Ramsay and Huber, 1987; Alsop and Holdsworth, 2006). Sheath fold formation involves (1) initial buckling of layers, largely controlled by lithological contrasts such as between marble and schist; and (2) amplification and rotation of fold axes as shear strain increases (Alsop and Holdsworth, 2006). It has been shown that sheath folds can form under both constrictional (e.g., Ez, 2000) and "nonconstrictional" regimes (e.g., Cobbold and Quinquis, 1980; Alsop and Holdsworth, 2006). Under constriction, a bull's-eye sheath fold pattern is predicted with ellipticity of the innermost ring less than that of the outermost ring, whereas under general shear, a cat's-eye geometry is predicted with innermost ring ellipticity greater than that of the outer ring. During simple shear, innermost and outermost rings have similar ellipticities, producing an analogous eye pattern.

F_2 tight to isoclinal fold closures commonly do not show eye patterns. However, along the ZSZ, cat's-eye geometries occur, indicative of general shear (a combination of simple shear and pure shear flattening). Along the perimeter of the migmatite dome, these folds strongly rotate into alignment with the strong (S_3) top-to-the-NNE shearing fabric in the KSZ, indicating the structures formed during top-to-the-NNE shearing (Alsop and Holdsworth, 2006). These folds preserve S_2 crenulation cleavages in their limbs with axial planar kyanite, indicating that these structures formed during M_2 conditions. Kyanite is also aligned with the pervasive S_3 NNE-SSW stretching lineation, and therefore we interpret that the folds formed in two stages: (1) F_1 isoclinal folds developed during prograde burial and thickening. (2) This was followed by non-coaxial top-to-the-NNE general shear during exhumation, synchronous with (M_2) Barrovian conditions forming F_2 folds that produce the sheath-type geometries as shown in Figure 6E.

F_3 Folds

Upright isoclinal folds (F_3; Figs. 4–10) also occur along NNE-SSW axes parallel to the NNE-SSW lineation and have been noted by several workers on Naxos (Urai et al., 1990; Buick, 1991a, 1991b) and other Aegean islands, including Tinos, Andros, Syros, Paros, and Mykonos (e.g., Virgo et al., 2018, and references therein). These folds outcrop across all units despite spatially contrasting in style. Within the migmatitic core, an earlier generation of upright, E-W–trending isoclinal folds is refolded by orthogonal to NNE-SSW–trending upright structures. These structures are defined by vertically dipping marble bands and pelitic horizons that sometimes enclose boudinaged amphibolites, which have experienced polyphase micro- and macroscale folding. Although meter-scale folds in the migmatites do occur, they do not have a consistent axial trend and were probably formed by flow of partial melts (Jansen and Schuiling, 1976). Within the migmatite dome, our observations suggest that F_3 folds are completely discordant to the overlying structures and are truncated by normal faults and the NPDS that bounds the metamorphic footwall. Within migmatite, the leucosomes and kyanite blades are folded with the foliation (Figs. 8, 13B, and 13C) by F_3 folds. This differs from the overlying carapace, where these structures range from open to tight and refold the limbs of F_1 and F_2 folds, but also have their fold axes trending parallel to the lineation (NNE-SSW; Fig. 6H). Therefore, F_3 folds must postdate peak M_2 kyanite-grade conditions and F_1 and F_2 folding, yet they must have formed in the presence of melt and simultaneous to doming as they wrapped around the core (Buick, 1991a, 1991b).

The origin of these folds has been the subject of considerable debate. Some workers have suggested that F_3 folds formed during E-W compression responsible for gentle island-scale postmetamorphic E-W doming of the isograds (Buick and Holland, 1989; Urai et al., 1990; Buick, 19911, 1991b), while other studies inferred their origin to be a result of extensional shearing, as similar features are present in other extensional terrains (Hodges et al., 1987). Rey et al. (2011, 2017) and Kruckenberg et al. (2011) argued that folds in the migmatite dome developed during convergent flow and the viscous collision of two weak channels of the lower crust during regional NE-SW crustal extension. However, this mechanism cannot explain the earlier isoclinal folding, top-to-the-NNE–related sheath folding, and upright F_3 fold geometries within the metamorphic carapace. Alternatively, Buick (1991a, 1991b) proposed F_3 folds within the carapace originated in their current orientation under greenschist-facies conditions, as rotation into alignment with top-to-the-NNE shearing would cause flattening. Because F_3 structures fold ductile mylonite fabrics, have NNE-SSW boudinaged limbs (see Fig. 10), and have upright fold axes that are truncated by the NPDS, we suggest they must have formed due to significant E-W shortening that predated NNE-SSW crustal extension.

Core High-Strain Zone

Three-dimensional relationships of polyphase folding can be spectacularly observed in amphibolite bands within marble in the CHSZ of the Boulibas and Kinidaros Quarries, where ductile pinching and boudinage of tight upright F_3 antiforms and synforms crop out (Figs. 9 and 10). These amphibolite horizons act as strain markers and show evidence for superimposition of multiple F_3 fold geometries, vertical boudinage (i.e., boudinage with subhorizontal neck lines), horizontal NNE-SSW boudinage (i.e., boudinage with neck lines orientated subvertically), flattening, brittle fracture, and S-C shear fabrics with opposing shear senses on opposite limbs of folds. Boudinage and shear bands with opposing shear senses are orientated in the vertical and NNE-SSW horizontal planes, symmetrically arranged on the limbs of F_3 folds and aligned with their axial surfaces (Fig. 9 and 10). These indicate directions of maximum extension in the vertical and NNE-SSW horizontal planes. F_3 fold interference patterns suggest that E-W–trending upright isoclinal folds are refolded by tight to isoclinal NNE-SSW–trending folds with vertically plunging hinge lines, which in turn are refolded by several scales of upright parasitic folds with N-S–trending hinge lines. Intersection of these three fold axes about a vertical point (Fig. 10E) suggests this structure is a Ramsay type-2 fold interference feature. Vertical boudinage affects the limbs of these folds and vertically intruded pegmatites and indicates the minimum principal stress (σ_3) was vertically orientated and much less than the horizontal stresses. These observations lead us to suggest the maximum and intermediate principal stresses (σ_1 and σ_2) must have been almost equal and orientated in the horizontal plane at the time of F_3 folding and shortly thereafter. This indicates that bulk horizontal shortening and constriction coincided with sillimanite-grade partial melting. During this constrictional regime, the maximum principal stress σ_1 must have been initially oriented N-S to produce E-W–trending folds and was subsequently rotated about a vertical axis into an E-W orientation to produce NNE-SSW–trending fold axes. Finally, NNW-SSE horizontal stretching lineations, horizontal boudinage, and horizontal fracture, indicative of a horizontal NNE-SSW–oriented σ_3, postdated the folding and vertical boudinage and occurred while the amphibolite was starting to behave in a brittle manner during cooling. These NNE-SSW horizontally boudinaged amphibolites indicate NNE-SSW extensional strains of ~50% by dominantly pure shear (Fig. 9F), with a component of simple shear as demonstrated by domino boudins (Fig. 9D). The boudins show opposing shear senses on opposite limbs of F_3 folds, suggesting the shearing postdated folding (Fig. 9G; Virgo et al., 2018). Based on this evidence, we propose that NNE-SSW stretching, which is definitively related to horizontal crustal extension, must have postdated upright F_3 folding and horizontal constriction, but it commenced while the rocks were still hot enough to deform in a plastic manner shortly following peak anatectic conditions, but at temperatures when amphibolite starts to deform in a brittle manner (e.g., <640 °C at 6.5 kbar; Cao et al., 2017).

These interpretations agree with Virgo et al. (2018) and Von Hagke et al. (2018), who demonstrated that there are five generations of boudinage and that the first vertical boudins are overprinted by later NNE-SSW horizontal boudins. Vertical boudinage includes two generations of pinch and-swell boudins, the first with a longer and the second with a shorter wavelength. These features are followed by NNE-SSW horizontal domino boudins, torn boudins, and hairline veins reflecting embrittlement of the amphibolite layers associated with retrograde cooling and exhumation. These studies also demonstrated that outcrop-scale parasitic asymmetric folds predate torn boudins and hairline veins, whereas domino boudins indicate locally deviating shear sense on opposite limbs of F_3 folds (Fig. 9G). Virgo et al. (2018) and Von Hagke et al. (2018) concluded that long-wavelength pinch-and-swell boudins (i.e., vertically orientated boudinage) are consistent with syn-migmatitic flow and F_3 folding in the surrounding rocks and noted that static recrystallization in the amphibolite must have postdated vertical boudinage. Based on this reasoning and the synchronicity among upright F_3 folding, vertical boudinage, and migmatization, we also agree that static recrystallization must have postdated upright F_3 folding and horizontal constriction at the center of the migmatite dome, but annealing was due to high temperatures outlasting contractional deformation during M_3, and prior to NNE-SSW extensional deformation. We therefore propose that the CHSZ documents a major rotation in principal stress axes from bulk horizontal shortening and constriction to NNE-SSW extension during the close of the M_3 event in the presence of partial melt.

Extensional Shear Zones

Although extensional (S_3) top-to-the-NNE shearing is penetrative throughout the entire metamorphic carapace (Zas and Koronos Units), there is petrological and geochronological evidence that the fabrics formed at different times and at different conditions across Naxos. Discrete shear zones, represented by mylonites and show microstructures displayed in Figures 11–13, separate each tectono-stratigraphic unit and are truncated by the geometry of the NPDS. These are now described in chronological order from structurally deep to shallow.

Koronos Shear Zone

The KSZ is a normal-sense NNE-SSW–trending shear zone that wraps around and is folded by the underlying migmatite dome. It represents the basal contact of the highly strained metamorphic carapace mantling the migmatite dome and places the kyanite-grade Koronos Unit against relatively less sheared migmatites of the Core Unit. Immediately around the dome margins, the migmatitic foliation is concordant with the overlying carapace; however, less than 100 m down structural section, this foliation becomes highly discordant, where F_3 upright folds and kilometer-scale subdomes can be traced along the migmatitic foliation (Kruckenberg et al., 2011). This abrupt truncation in foliation and its gradual rotation into alignment with the enveloping Koronos Unit suggest the presence of a major tectonic boundary along the migmatite-gneiss contact, characterized by extreme grain-size reduction. High-temperature blastomylonites, feldspar plasticity, grain boundary migration, and chessboard extinction of quartz indicate deformation temperatures exceeding 600 °C (Figs. 8 and 12). Strain analysis of kinematic indicators implies overall general shear (a combination of NNE-SSW simple shear and E-W pure shear), suggesting a large component of flattening perpendicular to this shear zone coeval with definitively top-to-the-NNE kinematics on all dome margins in both northern and southern Naxos. This strongly indicates this shear zone is folded by the doming migmatites, and therefore its movement predates migmatite dome formation.

Along the east and west margins of the migmatite dome, leucogranitic sills and dikes increase in abundance and emanate from the underlying migmatites (Vanderhaeghe, 2004). These sills and dikes commonly truncate the S_3 mylonite foliation, suggesting they intruded synchronously with or postdate high-temperature shearing on the KSZ. However, on western Naxos, they rotated about a NNE-SSW horizontal axis into alignment with the NPDS (see below; Fig. 6P). These dikes appear to have been rotated by ~45° due to later doming of all fabrics. Domains of less-strained material unaffected by penetrative (S_3) S–C′ fabrics reveal earlier folding, i.e., (S_{2a}) crenulation cleavages and (S_{2b}) cleavage domains that display top-to-sigma porphyroclasts with opposing top-to-the-SW shear senses (see Fig. 8), signifying structural reactivation at high-grade conditions. Structural imbrication and preservation of relict thrust features are inferred from thin marble bands along the KSZ that display tight to isoclinal internal folding bounded by highly strained intercalated schists that have localized the deformation due to their competency contrast with the stronger marbles (see Fig. 8). Imbricated slices of the same marble horizon can be identified by an abrupt change in foliation across strike, and they splay off the main detachment horizon.

Slices of orthogneisses basement underlying the shelf sequence are structurally repeated and overlie metasediments and amphibolites at the upper levels of the shear zone. This, combined with microstructural evidence, suggests that the KSZ possibly represents a relict SW-verging thick-skinned thrust that was one of presumably many thrusts responsible for thickening of the continental margin. These structures imply crustal shortening and thickening was extensive across Naxos and possibly led to regional Barrovian metamorphism. The compressional features and thrusts were then reactivated as normal-sense shear zones during the exhumation of the migmatites from (M_2) kyanite-grade to (M_3) sillimanite-grade conditions in the footwall.

Zas Shear Zone

A NE-SW–trending greenschist-facies shear zone cuts through the flank of Mount Zas, juxtaposing the greenschist-facies (relict blueschists) Zas Unit against the underlying kyanite-grade Koronos Unit, and it can be traced over 20 km along strike (Figs. 3 and 4). This structure is associated with an increase in mylonitization over a 500 m zone, overprinting and truncating F_1 and F_2 structures. These folds rotate into alignment with the shear zone, producing sheath folds with their noses pointing parallel to the lineation (NE-SW), in agreement with Buick (1991a, 1991b). This structure could represent a reactivated thrust originally placing the Cycladic Blueschist Unit onto the underlying, more-proximal sedimentary cover (Koronos Unit), as relict (F_1) hanging-wall anticlines, S_2 crenulation cleavages, and relict top-to-the-SW S-C fabrics are preserved in micaceous domains and within greenschist-facies porphyroblasts (see Figs. 6 and 11). S-C′ mylonites are associated with top-to-the-NNE (S_3) shearing and exclusively affect greenschist-facies assemblages.

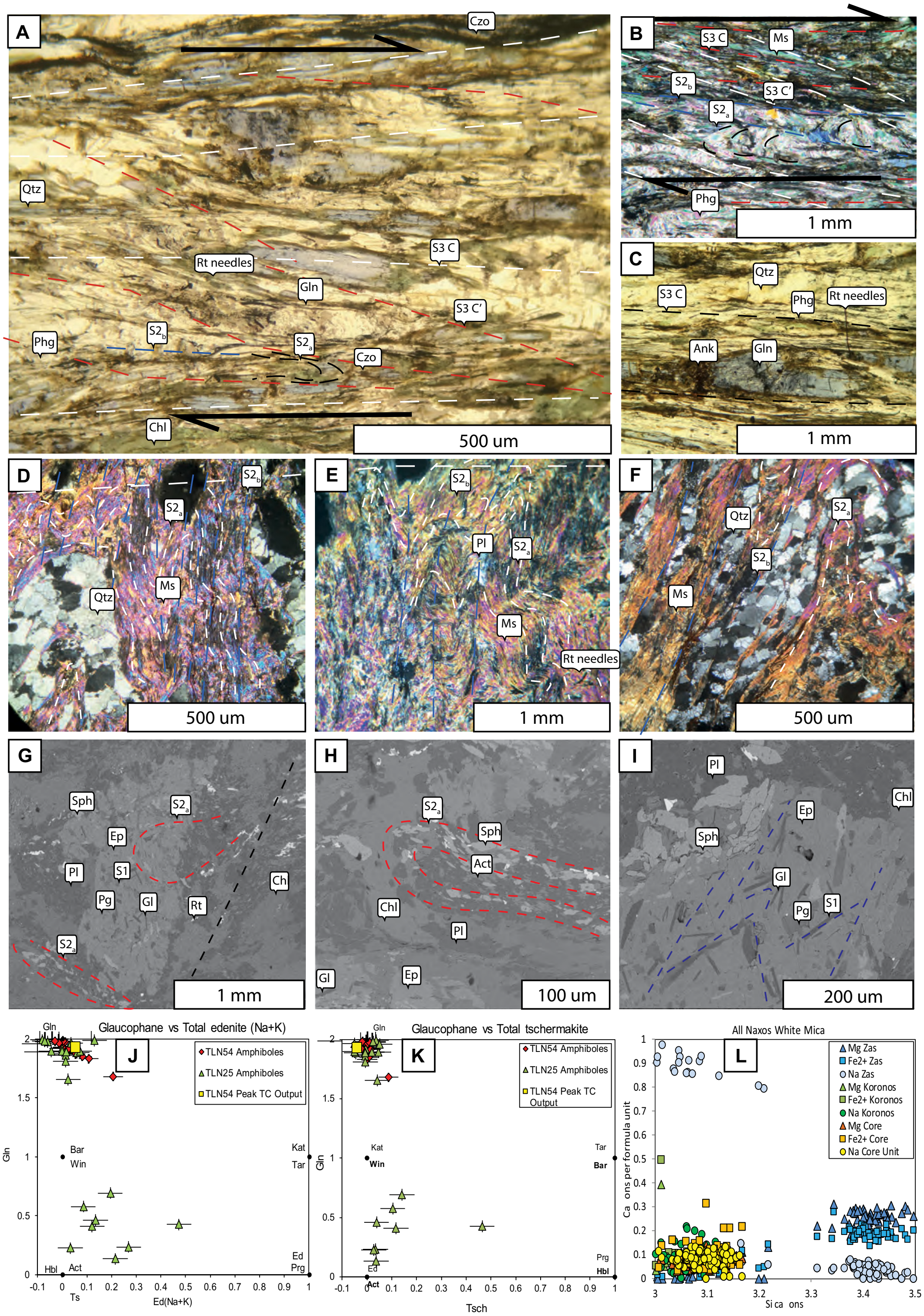

Figure 11. Representative photomicrographs and backscattered electron images of Zas Unit microstructures and mineral chemistry. Mineral abbreviations follow Whitney and Evans (2010). (A–C) TLN54 (meta-tuff) glaucophane phengite schist displaying well-preserved glaucophanes aligned with S_1 top-to-the-NNE shearing fabrics, but also affected by S_3 top-to-the-NNE S-C′ fabrics that affect both M_1 and M_2 assemblages. In lower-strain domains, S_{2a} and S_{2b} crenulation cleavages can be identified by folded bands of rutile needles, titanite phengite, and plagioclase, suggesting S_2 postdated high-pressure conditions. (D–F) Quartz mica schist displaying well-developed S_2 microstructures including millimeter-scale isoclinal folds and S_{2a} crenulation cleavages, with no evidence for S_3. This greenschist assemblage implies that S_2 fabrics also developed during M_2. (G) TLN25 (Zas Unit) backscattered image showing calc-schist, where epidote traps earlier S_{2a} fabric, and microfolding is defined by phengitic mica, actinolite, and titanite. Inclusions of glaucophane and paragonite in epidote represent M_1 conditions and outline S_1 fabrics. S_3 top-to-the-NNE extensional S-C′ fabrics affect matrix assemblages including actinolite, chlorite, and plagioclase. (H) TLN25 backscattered image showing S_2 microfolded fabric that is defined by grains of titanite that formed after peak M_1 conditions and predate greenschist-facies shearing. This implies that S_2 crenulation cleavages formed at upper-greenschist-facies conditions on the retrograde part of the pressure-temperature loop. (I) TLN25 close-up backscattered image of M_1 inclusions in epidote defined by glaucophane and paragonite, which preserve S_1 S-C shear fabric. Small inclusions of sphene are also included in epidote, although coarse sphene grows externally. (J) Glaucophane vs. total edenite for Zas Unit samples plotting solely in the bottom left-hand corner diagnostic of low-temperature–high-pressure amphibole. TC output—Thermocalc output. (K) Glaucophane vs. total tschermakite for Zas Unit samples TLN54 and TLN25 showing the range from actinolite to glaucophane compositions, with TLN54 modeled glaucophane composition for comparison. (L) All Naxos white mica; note the distinctive trimodal population of data, where high Si (>3.4 pfu) represents high-pressure phengite solely within the Zas Unit, high Na (>0.9 pfu) is characteristic of paragonite, again only within the Zas Unit, and where Koronos and Core Units represent one mica population characteristic of Barrovian M_2 conditions.

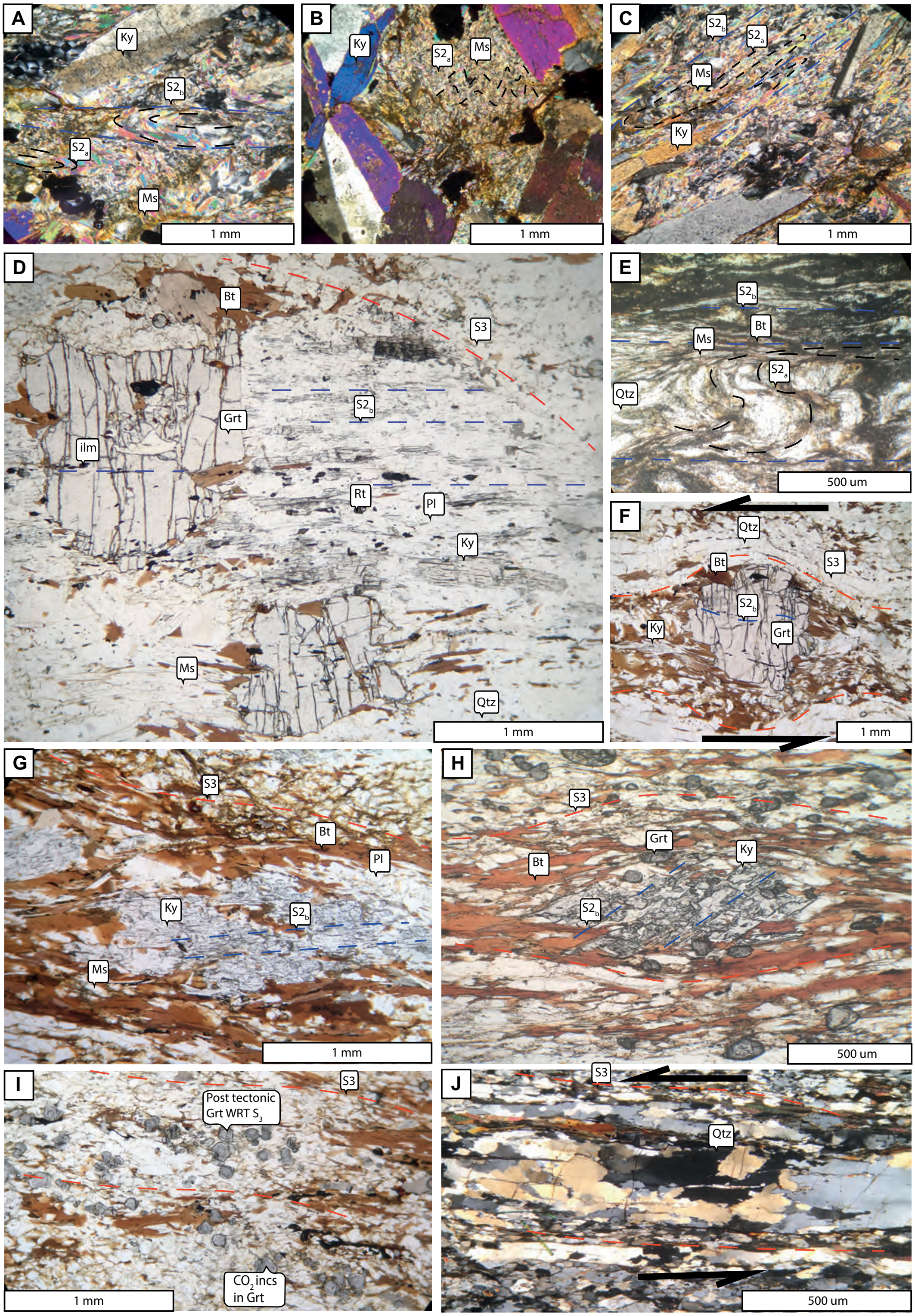

Figure 12. Collection of photomicrographs from the Koronos Unit to demonstrate key microstructures and fabrics during prograde and peak M_2 conditions. Mineral abbreviations follow Whitney and Evans (2010). (A–C) 17TL110, a kyanite muscovite schist with coarse millimeter-sized kyanite blades that overgrow the S_{2a} crenulation cleavages defined by muscovite and are aligned subparallel to the subsequent S_{2b} foliation. (D) TL67 (Koronos Unit) peak M_2 Grt-Ky-Rt-Ilm-Ms-Pl enclave that is pretectonic with respect to S_3, which deforms around it. Garnet is posttectonic to S_{2b}, which developed along cleavage domains of previous S_{2a} crenulations, seen as inclusion trails through garnet. Ky and Rt grew simultaneously with S_{2b}, as they are aligned parallel to the fabric, but discordant to the external S_3 fabric. (E) TLN47, a kyanite mica schist preserving S_{2a} crenulations. (F) Garnet porphyroclast showing sinstral top-to-NE shearing fabric (S_3), which is subparallel to the inclusion trails that define the S_{2b} foliation. (G) TLN13 (Koronos Unit), plane-polarized light (PPL) image showing enclaves of pretectonic Ky + Ms breaking down to Bt, which is affected by S_3 S-C′ fabric. Small garnets (<100 µm) are found as inclusions within kyanite, preserving peak assemblage Grt-Ky-Bt-Ms-Plag-Qtz. (H) TLN22 (Koronos Unit) showing early kyanite enclaves that preserve S_1 and S_2, which have been rotated counterclockwise associated with development of S_3. Small posttectonic garnets have idioblastic faces and crosscut the S_3 fabric, and they show fluid inclusion bubbles, many of which are dark, indicating a mixed CO_2-H_2O fluid during garnet growth after top-to-the-NNE shearing. (I) TLN22 clearly showing small postkinematic garnets that crosscut the S_3 fabrics, implying high temperatures outlasted deformation and were possibly associated with hydration at M_3 sillimanite-grade conditions. WRT—With respect to. (J) TL67 blastomylonite quartz microstructures showing sweeping subgrain boundaries consistent with grain boundary migration followed by static recrystallization and coarsening.

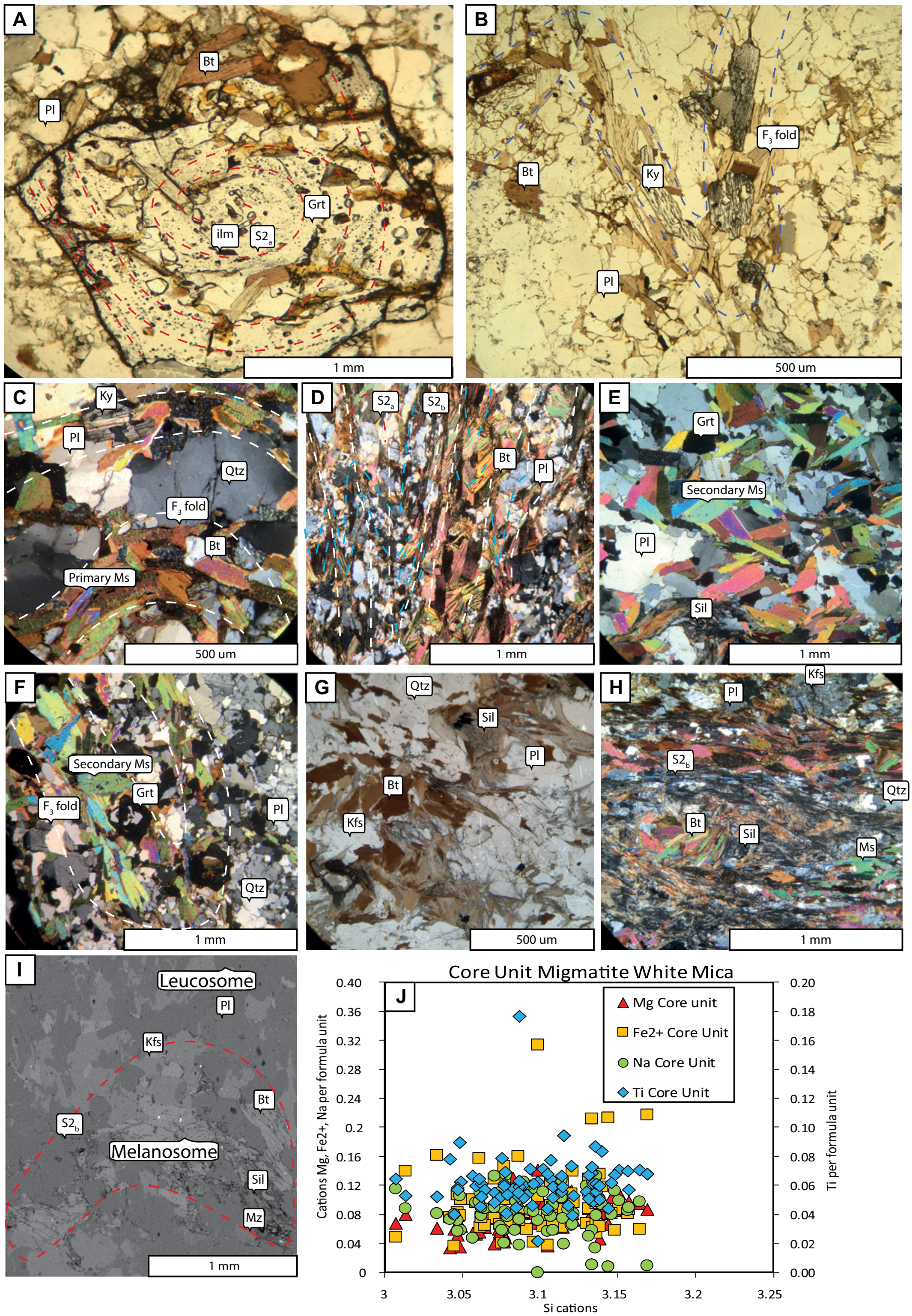

Figure 13. Representative photomicrographs and back-scattered-electron images and mineral data from Core Unit samples. Mineral abbreviations follow Whitney and Evans (2010). (A) TL15 garnet kyanite migmatite showing prograde garnet with a rotational inclusion trail that rotates into alignment with the external S_{2b} matrix fabric, indicating that garnet formed coeval with S_{2a} and S_{2b}. (B) TL15 kyanite folded with the S_{2b} foliation by an upright F_3 fold, clearly implying that kyanite predates F_3 folding. (C) TL15, showing another example of an F_3 fold closure affecting biotite kyanite muscovite folia, with some primary prismatic muscovite preserved. (D) TLN34 showing well-developed S_{2b} foliations with S_{2a} crenulations preserved by the interlocking habit of biotite. (E–F) TL66 garnet sillimanite migmatite showing coarse crosscutting secondary muscovite in both leucosome and melanosomes, with atoll garnets. Sillimanite-biotite intergrowths show decussate textures diagnostic of kyanite to sillimanite transformation and coarse crosscutting secondary muscovite indicative of re-equilibration and back reaction through the muscovite dehydration melting reaction. (G) TLN34 sillimanite garnet K-feldspar migmatite with peritectic K-feldspar adjacent to biotite and sillimanite, indicative of incongruent melting. It also shows a range of deformation microstructures from brittle fracture to dynamic recrystallization and extensive grain-size reduction with chessboard extinction in quartz following anatexis, indicative of deformation temperatures from 700 °C to 350 °C. (H) TLN20A biotite sillimanite migmatite with peritectic K-feldspar and well-developed S_{2b} fabrics, where there is a very small amount of primary muscovite preserved. (I) TLN34 showing inclusions of monazite within biotite, and sillimanite quartz intergrowths within melanosomes, which will be dated in a future paper. (J) Core Unit white mica data, showing the spectrum of muscovite compositions, where Si <3.10 pfu and Ti >0.06 pfu are diagnostic of secondary muscovite.

These structures signify extensional reactivation during the close of regional (M_2) conditions at temperatures of 280–450 °C, as demonstrated by subgrain rotation and bulging of quartz grain microstructures (Stipp et al., 2002b).

Naxos-Paros Detachment System

The NPDS records the evolution of a ductile shear zone from solely brittle deformation at the top to completely ductile deformation beneath a few hundred meters (Buick, 1991a, 1991b). This detachment horizon truncates all compressional structures (Fig. 3) and is gently folded along a NNE-SSW axis, bounding the entire island. The brittle fault (Moutsana detachment; Cao et al., 2013, 2017), and its associated deformation, is best exposed in the NW and central Naxos (near the towns of Melanes and Galanado; Fig. 3) and on the eastern coastline at Moutsana peninsula. Numerous brittle high-angle faults root into the fault horizon, which is associated with a 20 m cataclasite and fault breccia zone, including pseudotachylytes, that grades into ductile mylonites. The fault surface is commonly steeply dipping at ~40° perpendicular to the transport direction and is associated with a shallowly NNE-plunging lineation, which is oblique to the foliation, consistent with a lateral ramp geometry. In central Naxos, the detachment is folded into a gently northerly plunging synform (see Fig. 7G), causing the nonmetamorphic hanging wall to be exposed in a graben-type structure that is bounded by steep late crosscutting E-W–trending normal and NE-SW– and NW-SE–trending strike-slip faults (see Fig. 3), juxtaposing the granodiorite to the west and the metamorphic sequence to the east (see Figs. 3 and 4). This doming also affects the Pliocene–Pleistocene sedimentary successions within the hanging wall of the NPDS and requires a component of E-W shortening during and after movement on this structure, which was also responsible for folding the isograds and development of minor brittle thrust faults.

Beneath this low-angle normal fault, right-way-up regional metamorphic isograds are telescoped and affected by flattening, indicating the fault cut through metamorphic stratigraphy (Fig. 7G). On west Naxos, brittle deformed cataclasites and sediments are juxtaposed against upper-amphibolite-grade migmatites, a transition of ~700 °C within 1000 m across strike, revealing frozen-in metamorphic field gradients of up to ~700 °C km^{-1}. Although S-C′ fabrics (S_3) affect all structural levels of the footwall, there is a larger intensity of shearing fabric development on this structure. Quartz microstructures indicate dynamic recrystallization occurred via a spectrum of deformation mechanisms, from subgrain rotation and bulging to brittle deformation, indicative of deformation temperatures less than ~500 °C (Stipp et al., 2002a). Over 95% of samples demonstrate top-to-the-NNE kinematic indicators by asymmetrical alpha and delta porphyroclasts of biotite, kyanite, plagioclase, and garnet, in agreement with Urai et al. (1990) and Buick (1991a, 1991b). We interpret this brittle-ductile shear zone to be related to crustal extension and exhumation, as brittle normal faults root into it, and it clearly postdates, is discordant to, and truncates all compressional and metamorphic features. The west Naxos I-type granodiorite is mylonitized on its eastern margin, indicating the fault was active during crystallization at ca. 12.2 Ma (Keay et al., 2001). The NPDS presumably represents a similar structure to the North Cycladic Detachment System on Mykonos, Tinos, and Andros (e.g., Jolivet et al., 2010; Jolivet and Brun, 2010) in accommodating regional crustal extension by top-to-the-NNE shearing along a localized zone on the brittle-ductile transition.

In contrast to the NPDS, the extensional fabrics in the ZSZ and the KSZ and condensed right-way-up high-grade metamorphic isograds are purely ductile features that are concordant to the island-scale foliation. The structural discordance between these internal shear zones and the brittle-ductile NPDS (Fig. 3) suggests that movement on the KSZ and ZSZ predated movement on the NPDS and therefore records the early stages of exhumation in the mid- to lower crust prior to migmatite doming and regional NNE-SSW Aegean extension.

Structures Outside the Metamorphic Core Complex

Upper Cycladic Nappe (Trench Mélange)

In western central Naxos, a largely dismembered sequence of ophiolitic material composed of hydrothermally altered pillow basalts, serpentinites, and oceanic sediments, including cherts with manganese nodules, outcrops in the hanging wall of the NPDS that transects central Naxos (Jansen and Schuiling, 1976; Vanderhaeghe, 2004). Structurally above this, there is a disturbed sequence of *Nummulite*-bearing dolomitic limestones/marbles, chloritized schists, and randomly orientated exotic blocks of marble and volcanic debris (Fig. 7). These field relations have been previously attributed to a "km-scale gravity slide" derived from the footwall of this detachment system (Vanderhaeghe, 2004; Kruckenberg et al., 2011). Although this could explain the wide variety of rock types, randomly orientated metamorphic boulders, and evidence for paleo-karstification, the extreme folding and entrainment of a variety of ophiolitic and distal oceanic material as blocks within a serpentine matrix bear many similarities to the ophiolitic mélanges of the Oman–United Arab Emirates ophiolite (Searle and Cox, 1999, 2002). We tentatively suggest that this sequence represents a tectonic mélange formed in a trench environment and was deformed during SW obduction of an ophiolite prior to Eocene subduction of the continental margin. Although scattered remains of upper ophiolitic material are distributed across the Cyclades at high structural levels (Katzir et al., 1996; Hinsken et al., 2017), ophiolite stratigraphy, including mantle peridotite, gabbro, plagiogranite, and a metamorphic sole, is exposed on Tinos (Lamont, 2018), implying that the ophiolite may have been widespread as the highest structural nappe across the entire Cyclades. The Miocene to Pleistocene sedimentary successions are unconformably laid on top of this mélange, and they are composed of fluvial conglomerates, in some cases with boulders and clasts of a variety of ophiolitic and metamorphic material derived from the footwall. The sedimentary rocks dip at ~30° away from the core complex, which is inconsistent with the dip predicted by normal faulting. Clearly, these sediments must have been rotated by gentle doming of the island during the Pliocene–Pleistocene and therefore indicate a significant component of E-W shortening after the core complex was exhumed. The I-type granodiorite has aplitic sills that are folded along an N-S–trending axis (see Data Repository Item[1]), also suggesting significant E-W shortening during and following crystallization at ca. 12.2 Ma.

PETROGRAPHY AND MINERAL CHEMISTRY

Blueschist, gneiss, and migmatite samples used in this study were collected at various structural levels of the Naxos MCC to investigate spatial variations in the pressure-temperature (*P-T*) conditions of peak metamorphism. Previous thermobarometric *P-T* results from studies of the Naxos MCC are presented in Table 1. The analytical techniques and procedures utilized to collect mineral composition data are outlined in the Data Repository Item (see footnote 1). Mineral abbreviations follow the guidelines of Whitney and Evans (2010), and migmatite terminology is after Ashworth (1975). Anhydrous phase compositions were calculated to standard numbers of oxygen per formula unit (pfu; Deer et al., 1992), micas were recalculated to 11 oxygens, and chlorite was recalculated to 28 oxygens. Where present, H_2O content was assumed to oc-

[1]GSA Data Repository item 2019167, Additional field and petrological observations and data, is available at http://www.geosociety.org/datarepository/2019 or by request to editing@geosociety.org.

TABLE 1. COMPILATION OF PREVIOUS PRESSURE-TEMPERATURE (*P-T*) ESTIMATES FOR VARIOUS STAGES OF DEFORMATION AND METAMORPHISM ON NAXOS

Stage	Lithology	Location	Unit	*P-T* conditions (kbar, °C)	Associated uncertainty (kbar, °C)	Method	Study
Peak M2	Metapelite	Migmatite dome	Core	6–7, 670	±2, ±50	Conventional thermobarometry	Jansen and Schuiling (1976)
Peak M2	Metapelite	Carapace	Koronos-Zas	5–7, 400–670	±2, ±50	Conventional thermobarometry	Jansen and Schuiling (1976)
Prograde M2	Metapelite	Migmatite dome	Core	8.0–9.7, 600	±2, ±50	Powell and Holland (1988)	Buick and Holland (1989)
Peak M2	Metapelite	Migmatite dome	Core	6–8, 690	±2, ±50	Powell and Holland (1988)	Buick and Holland (1989)
Prograde M2	Metapelite	Carapace	Koronos-Zas	10, 500	±1–2, ±50	Grt-Bt, GASP	Deuchêne et al. (2006)
Peak M2	Metapelite	Migmatite dome	Core	6–7, 700	±1–2, ±50	Grt-Bt, GASP	Deuchêne et al. (2006)
Peak M2	Ultramafic	Carapace	Koronos	–, 700–800	±50	Opx-Cpx thermometry	Katzir et al. (1999)
Peak M1	Metabasite	SE Naxos	Zas	12, 470	±2, ±50	THERMOCALC Average P-T	Avigad (1998)
Peak M1	Diaspore	East Naxos	Zas	>12, 450	±2, ±50	Diaspore-Corundum	Feenstra (1985)
Peak M1	Metabaite	SE Naxos	Zas	15.5, 576	±0.5, ±16	THERMOCALC Average P-T	Peillod et al. (2017)
Peak M2	Metabaite	SE Naxos	Zas	16.5, 619	±0.9, ±32	THERMOCALC Average P-T	Peillod et al. (2017)
Retrograde M2	Metabaite	SE Naxos	Zas	3.8, 384	±1.1, ±30	THERMOCALC Average P-T	Peillod et al. (2017)

Note: Mineral abbreviations follow Whitney and Evans (2010).

cur in stoichiometric amounts. The proportion of Fe^{3+}/Fe_{total} was calculated using AX (Holland, 2009), and amphibole exchange vectors were calculated using the method of Holland and Blundy (1994). Representative photomicrographs, backscattered electron images, and mineral compositions are shown for the Zas Unit in Figure 11, the Koronos Unit in Figure 12, and the Core Unit in Figure 13. A summary of the relative timings of fabric development is displayed in Figure 14, and garnet maps and line profiles from samples TL67, TL15, and TL66 are presented in Figure 15, Tables 2–4, and the Data Repository Item (see footnote 1). Summary *P-T* results of all samples are presented in Table 5.

Petrography of the Zas Unit

All samples in this unit display microstructural evidence for M_2 greenschist-facies overprinting of older M_1 blueschist-facies mineral assemblages and fabrics, with replacement spatially concentrated along zones of fluid alteration. M_1 high-pressure precursors occur as prograde inclusions or as relict matrix phases that have been pseudomorphed or trapped inside late lower-grade minerals. Glaucophane is unzoned and is preserved within the cores of epidote grains, with phengitic and paragonitic white mica, clinozoisite, and no plagioclase, and also along unaltered microstructural domains and foliations (Figs. 11A, 11C, 11G, and 11I).

All mineral compositional trends are displayed in Figures 11J, 11K, and 11L and highlight the high Na and low Al contents of primary amphibole, high Si pfu of mica, indicative of phengitic compositions, and paragonite that is characteristic of blueschist-facies conditions. A subsidiary population of actinolite is confined to the matrix, and it characterizes the M_2 greenschist-facies overprint. Late crosscutting greenschist-facies minerals are well developed in lesser-strained domains within the preexisting foliation, presumably from the breakdown of large porphyroblasts such as garnet to form epidote, plagioclase, chlorite, tremolite, and actinolite (Figs. 11G and 11H). Sodic amphiboles occur mainly as small prismatic inclusions in epidote and commonly display decussate-shear textures that could be associated with top-to-the-NE shearing during exhumation from blueschist facies (S_1; Figs. 11A, 11C, 11G, and 11I). This is aligned subparallel to the pervasive greenschist-facies top-to-the-NNE extensional fabric (S_3), which solely affects the surrounding quartz-mica–rich matrix. In low-strain domains, blueschist- to greenschist-facies assemblages containing phengitic muscovite, paragonite, biotite, plagioclase, green amphibole, and cloudy plagioclase are deformed in crenulation cleavages (S_2) that form a continuous fabric as inclusions throughout epidotes, with preserved microlithons (S_{2a}) and cleavage domains (S_{2b}; Figs. 11B and 11D–11H). These grains are rimmed by retrograde plagioclase and chlorite, indicating they are most likely associated with decompression from high-pressure conditions. S_{2a} is also associated with centimeter-scale isoclinal folding, with well-developed microlithons that act as parasitic folds on the limbs of larger-scale folds (see Fig. 11F). S_{2a} and S_{2b} presumably formed by shortening along two orthogonal axes at upper-greenschist-facies conditions but predate the characteristic lower-pressure retrograde M_2 greenschist assemblage. We therefore relate S_2 fabrics to overthrusting and ductile stacking of high-pressure nappes at crustal depths that postdated high-pressure conditions.

S_2 fabrics contrast to the more localized top-to-the-NNE S-C′ shearing fabric (S_3), which purely affected the greenschist-facies assemblages, including quartz, mica, plagioclase, and chlorite–rich domains. S_3 mylonite fabrics are heterogeneous and localized along discrete shear zones. S_3 is particularly developed in samples taken from the ZSZ, in a parallel orientation to the fold axial planes, and appears to utilize S_{2b} cleavage domains. Microstructurally, S_3 deforms the quartz and fine-grained mica-rich matrix around pretectonic greenschist-facies porphyroclasts, including clinozoisite, epidote, and late crosscutting muscovites, creating strain shadows, asymmetrical boudinage, and rotation of the porphyroclasts (Figs. 11A, 11B, and 11C). Dynamic recrystallization via subgrain rotation and bulging is persistent within quartz-rich domains, indicating deformation temperatures must not have exceeded 450 °C (Stipp et al., 2002a, 2002b). Due to these relationships, we interpret S_3 as a purely retrograde feature postdating (M_1) high-pressure and (M_2) greenschist-facies conditions, and it was related to exhumation of the core complex through the brittle-ductile transition (Buick and Holland, 1989; Urai et al., 1990; Avigad, 1998).

Petrography of the Koronos Unit (Kyanite-Grade Gneisses)

M_2 kyanite-grade schists reveal that this unit attained a contrasting metamorphic history to the overlying Zas Unit, with no petrographic evidence for (M_1) blueschist-facies conditions (Figs. 12 and 15). High-grade deformational textures are present throughout this unit, with evidence for prograde, peak, and retrograde microstructural fabrics that developed over a large temperature range from lower- to upper-amphibolite-facies conditions (Buick and Hol-

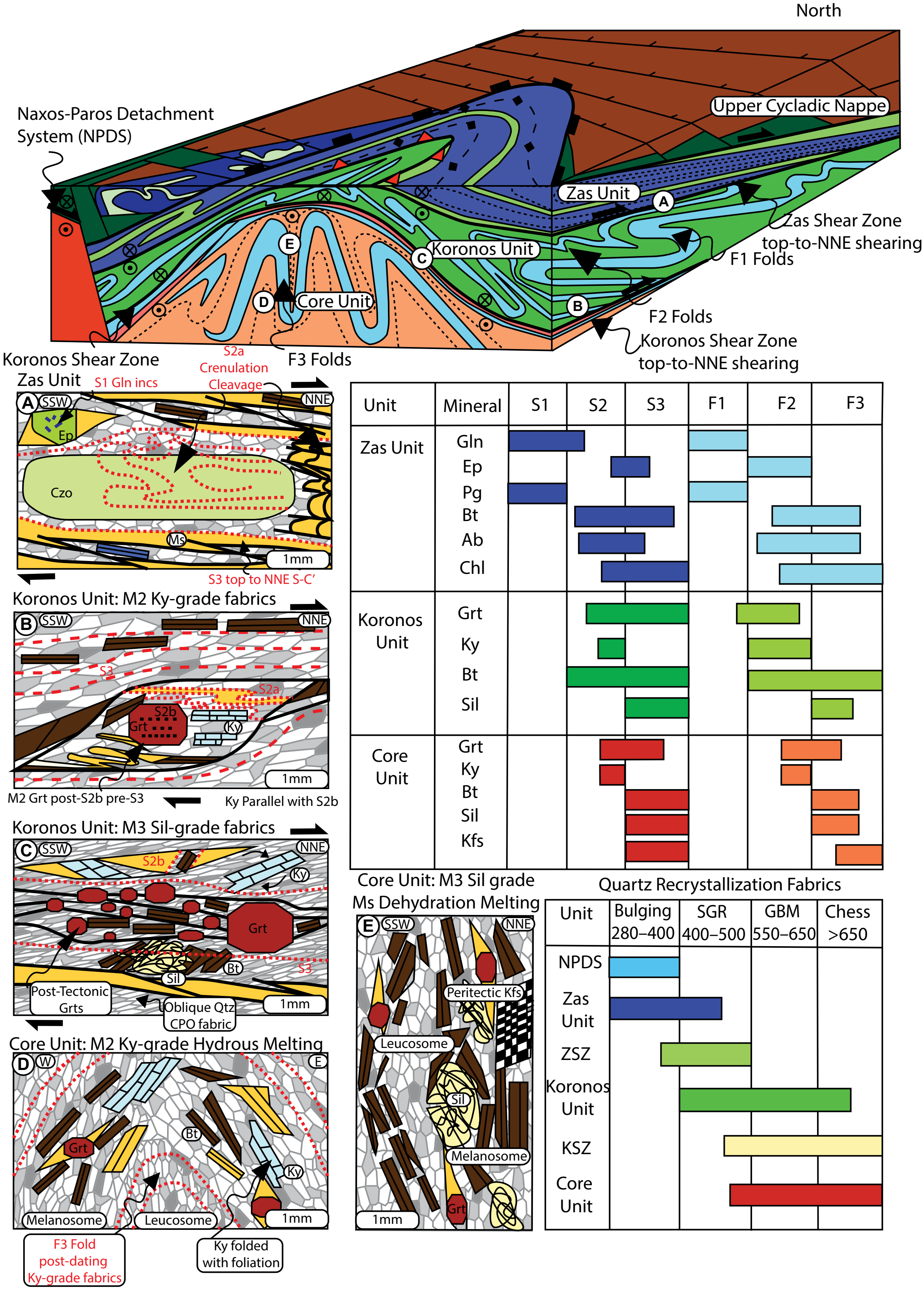

Figure 14. Schematic illustration of the deformation macrostructures and microstructures on Naxos, showing fabrics, order of mineral growth, deformation temperatures, and sequence of shearing and simplified sketches of microstructures. Mineral abbreviations follow Whitney and Evans (2010). GBM—grain boundary migration; SGR—subgrain rotation; KSZ—Koronos shear zone; ZSZ—Zas shear zone; CPO—Crystal preferred orientation. See text for discussion.

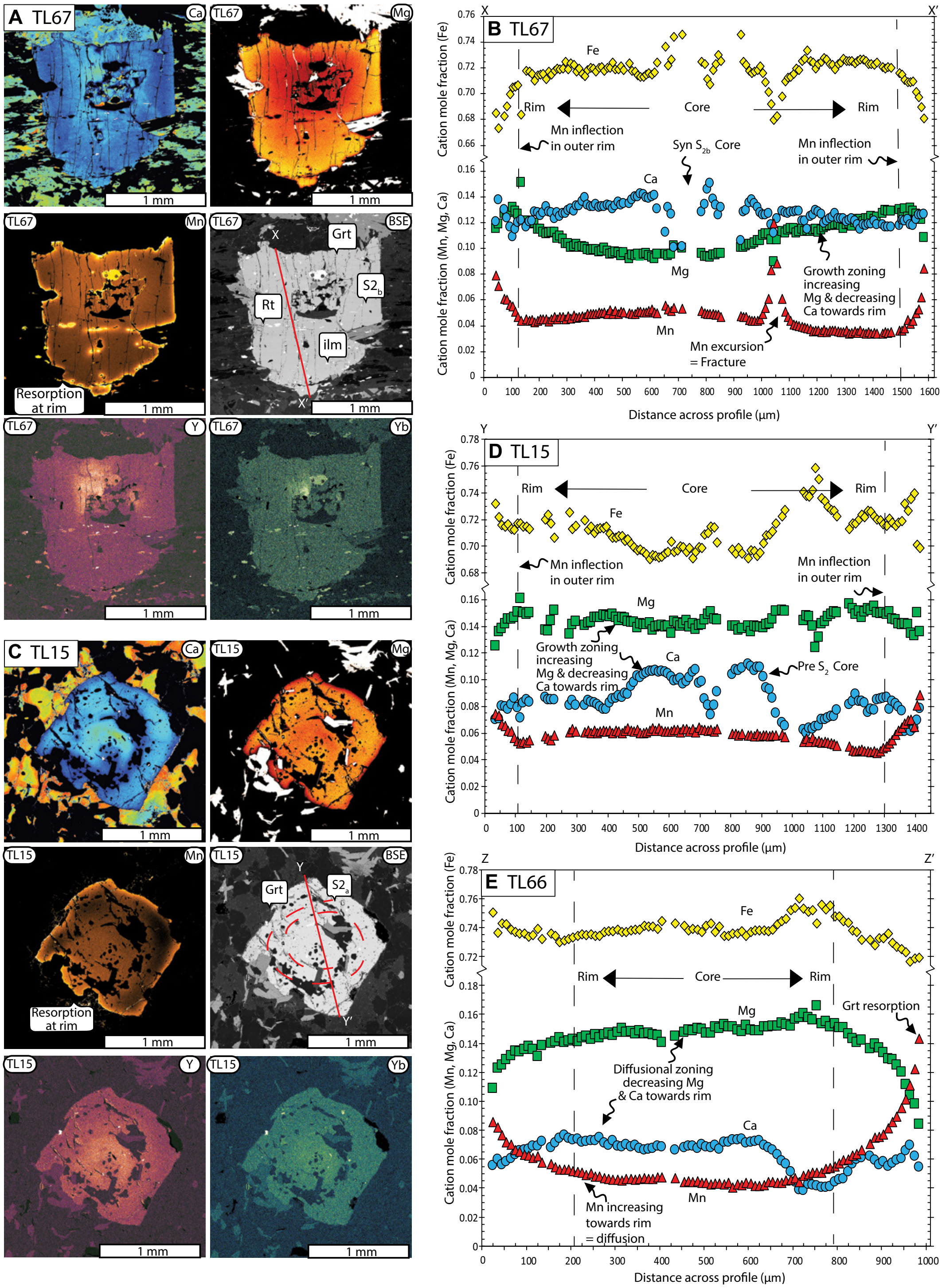

Figure 15. Representative fully quantitative electron microprobe maps and line profiles of garnet for samples TL15, TL67, and TL66 showing cation mole fractions of grossular, almandine, pyrope and spessartine (see text and Data Repository Item [text footnote 1] for discussion). Gaps in the profiles exist from crossing fractures and inclusions. Mineral abbreviations follow Whitney and Evans (2010). (A) TL67 maps of Ca, Mg, Mn, Y, and Yb showing prograde growth zoning and a backscattered-electron (BSE) image showing line profile X–X′ across the internal S_{2b} fabric. Note brighter color corresponds to larger element abundances. (B) TL67 profile X–X′ showing prograde growth zoning with increasing Mg from core to rim and decreasing Ca. An Mn inflection ~120 µm from the garnet rim is indicative of partial modification of the outer rim by diffusion. (C) TL15 element maps and backscattered-electron image (BSE) of a garnet with line Y–Y′ crosscutting the S_{2a} rotational inclusion trails. (D) TL15 profile Y–Y′ showing a slight increase in Mg and an abrupt stepwise decrease in Ca from core to rim indicative of a two-stage garnet growth history. An inflection in Mn indicates only the outermost 100 µm rim is somewhat modified by diffusion. (E) TL66 profile Z–Z′ showing diffusional zoning with a decrease in Mg from core to rim and generally decreasing Ca with an enrichment in Mn toward the rim (see Data Repository Item [text footnote 1] for trace of line profile).

land, 1989; Urai et al., 1990). In metapelitic lithologies, major phases include quartz, plagioclase, Ti-rich biotite, muscovite, garnet aluminosilicate, and minor K-feldspar (Figs. 13A–13J), and accessory minerals include tourmaline, apatite, chlorite, rutile, ilmenite, magnetite, monazite, and zircon. In aluminum-rich bands, up to centimeter-scale kyanite blades and euhedral garnet grains occur in close proximity, with the matrix separated into quartzofeldspathic domains and biotite and muscovite folia (see Figs. 12A–12D). The rare occurrence of staurolite is attributed to the semipelitic nature of the protoliths, with only relict fragments remaining following breakdown to produce garnet and kyanite:

$$\text{staurolite + muscovite + quartz} \rightarrow \text{biotite + kyanite + garnet} + H_2O. \quad (1)$$

This unit also shows contrasting microstructural fabrics to the overlying Zas Unit. S_1 is aligned parallel to bedding and is preserved as inclusions within kyanite and garnet cores, whereas crenulation cleavages (S_{2a} and S_{2b}) can be found in less-strained enclaves and as inclusions in garnet. Isoclinal folding occurs on a millimeter scale and is associated with microlithons (S_{2a}) and utilizes compositional

TABLE 2. REPRESENTATIVE QUANTITATIVE ANALYSES OF ZAS UNIT SAMPLES DERIVED FROM ELECTRON MICROPROBE

Sample:	TLN25	TLN25	TLN25	TLN25	TLN25	TLN25	TLN25	TLN25	TLN25	TLN25	TLN25	TLN25
Mineral:	Prg	Prg	Ms	Ms	Ep	Pl	Bt	Ta	Ta	Amp	Amp	Amp
SiO_2	49.12	47.82	49.40	48.01	38.53	62.30	40.82	62.68	63.05	58.66	59.65	56.89
TiO_2	0.28	0.25	0.32	0.17	0.00	0.00	0.78	0.07	0.20	0.07	0.08	0.03
Al_2O_3	38.60	39.79	25.81	26.60	25.34	20.73	15.80	0.70	0.25	9.77	8.48	1.51
FeO	0.66	0.62	3.63	3.98	8.53	2.43	14.42	7.02	6.83	12.87	13.23	10.64
MnO	0.03	0.00	.00	0.00	0.28	0.09	0.18	0.00	0.00	0.17	0.00	0.00
MgO	0.56	0.08	2.98	2.72	0.25	0.45	16.28	26.73	26.50	8.91	10.26	17.23
CaO	0.21	0.31	0.00	0.22	23.48	5.65	0.34	0.18	0.14	0.31	0.38	11.75
Na_2O	7.10	7.41	0.70	0.36	0.09	8.06	0.20	0.12	0.32	7.99	7.05	0.96
K_2O	1.69	0.86	10.02	10.17	0.07	0.10	8.82	0.43	0.00	0.07	0.00	0.00
Totals	98.25	97.14	92.86	92.23	96.57	99.81	97.64	97.93	97.29	98.81	99.13	99.01
Oxygens	11	11	11	11	12.5	8	11	11	11	23	23	23.00
Si	2.898	2.843	3.208	3.149	2.922	2.653	2.749	3.769	3.802	8.039	8.061	7.939
Ti	0.012	0.011	0.016	0.008	0.000	0.000	0.040	0.003	0.009	0.007	0.008	0.004
Al	2.685	2.789	1.976	2.057	2.266	1.041	1.254	0.050	0.018	1.578	1.352	0.249
Fe^{3+}	0.390	0.393	0.430	0.434	0.502	0.282	0.446	0.398	0.399	0.229	0.583	0.059
Fe^{2+}	0.033	0.031	0.197	0.218	0.541	0.087	0.812	0.353	0.344	1.246	0.912	1.183
Mn	0.001	0.000	0.000	0.000	0.018	0.003	0.010	0.000	0.000	0.019	0.000	0.000
Mg	0.049	0.007	0.288	0.266	0.028	0.029	1.634	2.396	2.381	1.819	2.068	3.584
Ca	0.013	0.020	0.000	0.015	1.908	0.258	0.025	0.012	0.009	0.045	0.055	1.758
Na	0.812	0.854	0.088	0.046	0.013	0.665	0.026	0.014	0.037	2.124	1.847	0.259
K	0.127	0.065	0.830	0.851	0.007	0.005	0.758	0.033	0.000	0.013	0.000	0.000
Sum	7.02	7.013	7.033	7.044	8.205	5.023	7.754	7.028	6.999	15.119	14.886	15.033
X_{Mg}	0.598	0.184	0.594	0.550	0.049		0.668	0.872	0.874	0.593	0.694	0.752
Fe^{3+}%	92.2	92.7	68.6	66.6	48.1		35.5	53.0	53.7	15.5	39.0	4.7
Alm%												
Sps%												
Prp%												
Grs%												
X_{Ca}						0.278						
Pl Al/Si						0.059						

Sample:	TLN54	TLN54	TLN54	TLN54	TLN54	TLN54	TLN54	TLN54
Mineral:	Amp	Amp	Amp	Chl	Ph	Ph	Prg	Pl
SiO_2	55.94	57.04	56.66	25.63	50.10	49.01	48.22	68.59
TiO_2	0.13	0.08	0.11	0.07	0.52	0.27	0.10	0.07
Al_2O_3	10.71	10.89	10.92	19.50	26.49	27.02	37.73	18.80
FeO	15.48	14.51	14.67	29.91	3.53	3.41	0.14	0.45
MnO	0.07	0.00	0.06	0.32	0.00	0.00	0.06	0.00
MgO	6.65	6.85	6.98	11.43	1.89	1.86	0.63	0.17
CaO	0.24	0.19	0.22	0.00	0.14	0.01	0.07	0.18
Na_2O	7.03	7.25	7.06	0.03	0.36	0.46	7.33	11.27
K_2O	0.03	0.05	0.00	0.06	10.29	10.37	0.40	0.05
Totals	96.27	96.85	96.70	86.95	93.32	92.41	94.68	99.58
Oxygens	23.00	23.00	23.00	14	11	11	11	8
Si	7.975	8.018	7.998	2.776	3.408	3.464	3.027	2.993
Ti	0.014	0.008	0.012	0.006	0.027	0.004	0.000	0.002
Al	1.800	1.805	1.817	2.490	2.124	2.045	2.911	0.967
Fe^{3+}	0.096	0.159	0.090	0.075	0.047	0.048	0.046	0.030
Fe^{2+}	1.750	1.547	1.642	2.709	0.201	0.165	0.030	0.016
Mn	0.008	0.000	0.008	0.029	0.000	0.003	0.000	0.000
Mg	1.412	1.435	1.469	1.845	0.192	0.287	0.000	0.011
Ca	0.037	0.028	0.034	0.000	0.010	0.008	0.008	0.008
Na	1.942	1.977	1.933	0.006	0.047	0.027	0.897	0.953
K	0.005	0.009	0.000	0.008	0.893	0.898	0.047	0.003
Sum	15.038	14.985	15.003	9.944	6.949	6.949	6.966	4.983
X_{Mg}	0.447	0.481	0.472	0.405	0.489	0.635	0.000	
Fe^{3+}%	5.2	9.3	5.2	2.7	19.0	22.5	60.5	
Alm%								
Sps%								
Prp%								
Grs%								
X_{Ca}								0.008
Pl Al/Si								−0.034

Sample:	TLN26	TLN26	TLN26	TLN26	TLN26	TLN26
Mineral:	Chl	Ph	Ph	Ms	Prg	Pl
SiO_2	24.84	50.64	50.96	49.12	47.20	68.08
TiO_2	0.23	0.15	0.00	0.63	0.28	0.00
Al_2O_3	20.27	25.39	25.21	26.66	33.35	19.59
FeO	28.20	3.64	3.56	2.86	1.31	0.00
MnO	0.00	0.00	0.14	0.15	0.06	0.05
MgO	12.40	2.69	2.55	2.67	1.13	0.33
CaO	0.01	0.11	0.00	0.00	0.15	0.18
Na_2O	0.11	0.01	0.00	0.50	1.13	11.20
K_2O	0.01	10.53	10.77	9.84	9.56	0.07
Totals	86.07	93.16	93.19	92.43	94.17	99.50
Oxygens	14	11	11	11	22	8
Si	2.716	3.475	3.498	3.386	3.089	2.980
Ti	0.019	0.008	0.000	0.033	0.014	0.000
Al	2.613	2.054	2.040	2.166	2.573	1.011
Fe^{3+}	0.000	0.000	0.000	0.000	0.179	0.010
Fe^{2+}	2.578	0.209	0.204	0.165	0.072	0.000
Mn	0.000	0.000	0.008	0.009	0.003	0.002
Mg	2.020	0.275	0.261	0.274	0.110	0.022
Ca	0.001	0.008	0.000	0.000	0.011	0.008
Na	0.023	0.001	0.000	0.067	0.143	0.951
K	0.001	0.922	0.943	0.865	0.798	0.004
Sum	9.971	6.952	6.954	6.965	6.992	4.988
X_{Mg}	0.439	0.568	0.561	0.624	0.604	
Fe^{3+}%	0.0	0.0	0.0	0.0	71.3	
Alm%						
Sps%						
Prp%						
Grs%						
X_{Ca}						0.008
Pl Al/Si						0.011

Note: Mineral abbreviations follow Whitney and Evans (2010).

layering between quartzofeldspathic and pelitic domains (see Figs. 12A–12C and 12E). Cleavage domains (S_{2b}) are superimposed on S_{2a} and in places completely overprint the microlithons to produce a strong spaced foliation defined by biotite-muscovite foliation (Figs. 12D and 12E). Large kyanite porphyroblasts are aligned coaxial with the foliations (S_{2a} and S_{2b}) and sometimes crosscut them, indicating these are prograde features. In numerous samples (e.g., TL67), euhedral garnets overgrow kyanite-bearing S_{2b} fabrics preserved in aluminum-rich domains, whereas in other samples (e.g., TLN22), garnets are enclosed by large kyanite porphyroblasts, suggesting simultaneous prograde growth of kyanite at peak M_2 conditions. In sample TLN21, garnets are up to several millimeters in diameter and distributed uniquely along tight isoclinally folded pelitic layers (S_{2a}), whereas in TL67, euhedral garnet porphyroblasts show straight faces truncating both S_{2a} and S_{2b} foliations, indicating garnet growth in this sample postdated initial thrusting and folding (Fig. 12D). Within some of these garnet porphyroblasts, dark fluid inclusions indicate garnet growth in a mixed saline CO_2/H_2O fluid, as noted previously (Baker and Matthews, 1994; Baker et al., 1989; Bickle and Baker, 1990; Kruelen, 1980). Kyanite has commonly broken down to biotite and is confined to pelitic domains with garnet. These domains form enclaves that are partially recrystallized as an extensional blastomylonitic top-to-the-NNE shear fabric (S_3) affecting the matrix and deforming around stronger kyanite-biotite-muscovite-plagioclase-garnet–rich enclaves, indicating these M_2 kyanite-grade assemblages are pretectonic with respect to S_3 (Figs. 12D, 12G, and 12H). S_3 was accommodated via grain boundary migration of quartz and ductile deformation of plagioclase associated with temperatures exceeding 600 °C (Stipp and Kunze, 2008). This was followed by coarsening and Ostwald ripening of grain boundaries, revealing static recrystallization. Annealing postdated deformation at close to peak conditions (Fig. 13J).

Toward the base of this unit along the KSZ, many samples display evidence for a thermal and static, lower-pressure overprint on a blastomylonitic S_3 fabric. This is demonstrated by posttectonic growth of (M_3) sillimanite and garnet (e.g., TLN21 and TLN22), which truncate the top-to-the-NNE S_3 fabric, indicating that high temperatures outlasted deformation. Peak (M_2) kyanite-bearing assemblages are overprinted by (M_3) sillimanite, and biotite intergrowths occur with plagioclase and quartz in dilational strain zones, demonstrating that the transition from kyanite to sillimanite occurred via a Carmicheal-type reaction scheme (Carmicheal, 1969) that postdated shearing (Figs. 12H and 12I).

TABLE 3. REPRESENTATIVE QUANTITATIVE MINERAL ANALYSES FROM THE KORONOS UNIT SAMPLES DERIVED FROM ELECTRON MICROPROBE

Sample:	TL67	TL67	TL67	TL67	TL67	TL67	TL67	TL67	TL67	TL67
Minerals:	Grt	Grt	Grt	Bt	Bt	Ms	Ms	Pl	Kfs	Kyanite
Location:	Inner rim	Core	Int	Matrix	with Ky	Matrix	with Ky	Matrix	with Grt	Matrix
SiO_2	37.97	37.51	37.20	36.29	35.07	46.30	46.88	61.41	65.34	36.03
TiO_2	0.10	0.08	0.20	3.27	3.40	1.05	1.29	0.00	0.18	0.09
Al_2O_3	20.75	21.29	20.24	19.54	18.36	34.79	34.44	24.33	18.64	62.45
FeO	31.11	28.77	31.66	19.13	21.08	1.85	1.65	0.03	0.01	0.77
MnO	2.22	4.73	2.10	0.23	0.16	0.00	0.00	0.01	0.00	0.02
MgO	3.57	2.71	3.28	9.70	8.09	0.60	0.61	0.00	0.00	0.00
CaO	4.83	5.72	5.07	0.00	0.05	0.06	0.00	5.58	0.00	0.01
Na_2O	0.01	0.00	0.07	0.05	0.31	0.85	0.60	8.34	0.40	0.00
K_2O	0.00	0.03	0.00	9.84	9.64	10.54	10.23	0.22	16.71	0.14
Totals	100.56	100.84	99.82	98.05	96.17	96.03	95.70	99.91	101.28	99.51
Oxygens	12	12	12	11	11	11	11	8	8	5
Si	3.010	2.970	2.978	2.679	2.678	3.073	3.107	2.728	2.987	0.982
Ti	0.006	0.010	0.012	0.182	0.195	0.052	0.064	0.000	0.006	0.002
Al	1.939	1.990	1.910	1.700	1.653	2.722	2.691	1.274	1.005	2.007
Fe^{3+}	0.031	0.060	0.120	0.000	0.000	0.000	0.000	0.001	0.000	0.000
Fe^{2+}	2.032	1.850	2.000	1.181	1.346	0.103	0.091	0.000	0.000	0.018
Mn	0.149	0.320	0.142	0.014	0.010	0.000	0.000	0.000	0.000	0.000
Mg	0.422	0.320	0.391	1.067	0.921	0.059	0.060	0.000	0.000	0.000
Ca	0.410	0.490	0.435	0.000	0.004	0.004	0.000	0.266	0.000	0.000
Na	0.002	0.000	0.011	0.007	0.046	0.109	0.077	0.718	0.035	0.000
K	0.000	0.000	0.000	0.927	0.939	0.892	0.865	0.012	0.975	0.005
Sum	8.001	8.001	7.999	7.757	7.792	7.014	6.955	4.999	5.008	3.015
X_{Mg}	0.172	0.148	0.164	0.475	0.406	0.364	0.397			
Fe^{3+}%	0	0	0.1	0	0	0	0			
Alm%	67.3	62.5	67.7							
Sps%	5.0	10.6	4.7							
Prp%	14.1	10.7	13.0							
Grs%	13.7	16.2	14.5							
X_{Ca}								0.267	0.000	
Pl Al/Si								0.273	0.005	

Sample:	TLN21	TLN21	TLN21	TLN21	TLN21	TLN21	TLN21	TLN21
Minerals:	Grt	Grt	Grt	Grt	Bt	Bt	Ms	Pl
Location:	Int	Core	Inner rim	Outer rim	Matrix	Matrix	Matrix	Matrix
SiO_2	37.72	36.90	37.70	36.82	36.11	35.56	46.75	61.23
TiO_2	0.28	0.00	0.32	0.13	3.74	3.99	1.28	0.08
Al_2O_3	20.37	20.84	20.67	20.73	19.10	18.23	34.11	23.69
FeO	31.17	33.56	32.60	30.93	19.98	19.64	1.52	0.30
MnO	1.78	3.27	2.20	6.12	0.00	0.22	0.00	0.06
MgO	4.16	2.98	3.47	2.57	8.09	8.13	1.19	0.00
CaO	3.43	2.59	3.37	2.08	0.24	0.00	0.08	5.23
Na_2O	0.13	0.24	0.07	0.59	0.07	0.19	0.75	8.96
K_2O	0.00	0.01	0.00	0.07	8.32	9.75	10.89	0.14
Totals	99.05	100.41	100.38	100.05	95.65	95.70	96.58	99.71
Oxygens	12	12	12	12	11	11	11	
Si	3.028	2.952	3.005	2.954	2.720	2.707	3.106	2.734
Ti	0.017	0.000	0.019	0.008	0.212	0.228	0.039	0.003
Al	1.928	1.966	1.943	1.961	1.696	1.636	2.741	1.247
Fe^{3+}	0.002	0.169	0.019	0.213	0.000	0.000	0.000	0.000
Fe^{2+}	2.091	2.077	2.154	1.862	1.259	1.250	0.059	0.011
Mn	0.121	0.222	0.149	0.416	0.000	0.014	0.000	0.002
Mg	0.498	0.355	0.412	0.307	0.908	0.922	0.060	0.000
Ca	0.295	0.222	0.288	0.179	0.019	0.000	0.000	0.250
Na	0.020	0.037	0.011	0.092	0.010	0.028	0.098	0.776
K	0.000	0.001	0.000	0.007	0.800	0.947	0.859	0.008
Sum	8.000	8.001	8.000	7.999	7.624	7.732	6.962	5.032
X_{Mg}	0.192	0.146	0.161	0.142	0.419	0.424	0.504	
Fe^{3+}%	0	0.1	0	0.1	0	0	0	
Alm%	69.5	73.4	71.7	69.9				
Sps%	4.0	7.4	5.0	13.9				
Prp%	16.6	11.8	13.7	10.2				
Grs%	9.8	7.4	9.6	6.0				
X_{Ca}								0.242
Pl Al/Si								0.252

Sample:	TLN22	TLN22	TLN22	TLN22	TLN22	TLN22	TLN22	TLN22	TLN22
Minerals:	Grt	Grt	Grt	Grt	Ms	Ms	Bt	Pl	Pl
Location:	Core	Inner rim	Outer rim	Int	Matrix	Matrix	Matrix	Matrix	Matrix
SiO_2	38.57	37.46	38.94	37.97	46.06	47.45	36.52	60.95	61.94
TiO_2	0.00	0.05	0.18	0.00	1.07	1.30	1.95	0.02	0.00
Al_2O_3	21.03	20.46	19.56	20.69	35.45	35.35	19.50	24.19	23.77
FeO	29.98	31.53	31.83	31.03	0.72	0.95	17.60	0.54	0.45
MnO	2.76	4.14	6.28	3.16	0.44	0.00	0.17	0.17	0.00
MgO	3.32	3.83	2.02	4.25	1.09	0.61	11.16	0.13	0.00
CaO	4.27	2.80	1.50	3.60	0.00	0.00	0.55	4.86	5.04
Na_2O	0.00	0.26	0.01	0.20	1.13	1.12	0.00	8.61	8.68
K_2O	0.01	0.00	0.02	0.00	9.37	9.81	8.89	0.20	0.00
Totals	99.94	100.54	100.34	100.90	95.33	96.60	96.33	99.67	99.87
Oxygens	12	12	12	12	11	11	11	8	8
Si	3.060	2.976	3.129	2.991	3.091	3.079	2.710	2.718	2.748
Ti	0.000	0.003	0.011	0.000	0.045	0.058	0.109	0.001	0.000
Al	1.967	1.916	1.853	1.921	2.737	2.717	1.706	1.272	1.243
Fe^{3+}	0.000	0.166	0.000	0.128	0.000	0.000	0.000	0.020	0.017
Fe^{2+}	1.989	1.928	2.139	1.916	0.078	0.074	1.092	0.000	0.000
Mn	0.185	0.279	0.427	0.211	0.021	0.008	0.011	0.006	0.000
Mg	0.393	0.453	0.242	0.499	0.048	0.074	1.234	0.009	0.000
Ca	0.363	0.238	0.129	0.304	0.000	0.009	0.044	0.232	0.240
Na	0.000	0.040	0.002	0.031	0.186	0.132	0.000	0.744	0.747
K	0.001	0.000	0.002	0.000	0.767	0.838	0.842	0.011	0.000
Sum	7.958	7.999	7.934	8.001	6.973	6.989	7.748	5.013	4.995
X_{Mg}	0.165	0.190	0.102	0.207	0.381	0.500	0.531		
Fe^{3+}%	0	0.1	0	0.1	0	0	0		
Alm%	68.6	67.7	73.4	66.2					
Sps%	6.2	9.3	14.2	7.0					
Prp%	13.1	15.1	8.1	16.6					
Grs%	12.1	7.9	4.3	10.1					
X_{Ca}								0.235	0.243
Pl Al/Si								0.275	0.245

Note: Mineral abbreviations follow Whitney and Evans (2010). Int—interior.

Within metapelitic samples, garnet shows a variety of compositional profiles that correlate directly with their microstructural relationships (Fig. 15; Data Repository Item [see footnote 1]). Garnet in TL67 preserves prograde growth zoning associated with a smooth transition from core to rim, increasing pyrope content, and homogeneous to slightly decreasing grossular content, as shown in Figure 15B. An inflection in the spessartine content on the outermost rim is indicative of some garnet resorption following peak conditions. In contrast, TLN22 has small garnets that crosscut the S_3 fabric and in places are engulfed by kyanite. These garnets show either a general decrease in the grossular component from core to rim, or the pyrope content slightly increases toward the inner rim followed by a decrease toward the outer rim, which is indicative of late garnet growth at lower pressure and temperature or homogeneous garnet profiles due to re-equilibration at lower pressures.

Along the KSZ, there is a band of ultramafic rock that is enclosed within foliated garnet-bearing amphibolites that are semicontinuous along strike and wrap around the dome. The metaperidotite enclaves enclosed within the amphibolites show partial serpentinization to anthopyllite, talc, and actinolite, but they preserve in situ olivine and orthopyroxene. Katzir et al. (1999) provided a detailed description of the petrography and geochemistry of these lenses and noted bimodal temperatures of ~700 °C and 1200 °C from pyroxene thermometry, suggesting they remained hot as they were emplaced into the shelf carbonate sequence. Within these amphibolites, there is some degree of hydrous M_2 migmatization but no petrographic evidence whatsoever to suggest they attained M_1 blueschist-facies conditions.

Petrography of the Core Unit

Samples from the migmatite dome preserve a petrologic record of kyanite- to sillimanite-grade (M_2–M_3) partial melting, and they display no evidence for having experienced Eocene M_1 conditions. Careful textural examination revealed that hydrous melting was the dominant melting process occurring within the Naxos dome, capable of producing between 1% and 7% volume melt based on reaction stoichiometry. However, at the deepest levels in pelitic lithologies, incongruent muscovite dehydration melting was the major melting process associated with growth of peritectic K-feldspar, removal of muscovite, and melt segregation from larger melt fractions (>20% melt), which eventually pooled to form S-type leucogranites that crosscut and intruded into the mantling carapace.

TABLE 4. REPRESENTATIVE QUANTITATIVE MINERAL ANALYSES FROM CORE UNIT SAMPLES DERIVED FROM ELECTRON MICROPROBE

Sample:	TL15	TL15	TL15	TL15	TL15	TL15	TL15	TL66	TL66	TL66	TL66	TL66	TL66	TL66	TLN34	TLN34	TLN34	TLN34	TLN34	TLN34
Mineral:	Grt	Grt	Grt	Grt	Bt	Ms	Pl	Grt	Grt	Grt	Ms	Bt	Pl	Pl	Grt	Grt	Kfs	Ms	Pl	Sill
Location:	Core	Inner rim	Outer rim	Int	Melanosome	Primary	Matrix	Rim	Core	Int	Secondary	Melanosome	Melanosome	Leucosome	Rim	Core	Matrix	Secondary	Matrix	Melanosome
SiO_2	37.08	38.64	37.55	37.67	36.31	47.07	62.45	37.12	37.27	37.12	45.95	35.07	56.95	61.66	37.10	37.23	65.12	46.34	65.79	36.16
TiO_2	0.00	0.00	0.03	0.07	3.29	1.37	0.00	0.00	0.20	0.00	1.20	3.40	0.00	0.10	0.00	0.13	0.47	1.57	0.00	0.00
Al_2O_3	20.60	20.07	20.27	20.60	18.80	33.67	23.45	20.58	20.33	20.63	34.62	18.36	29.84	24.87	20.73	20.71	19.01	34.86	20.94	62.16
FeO	31.56	31.12	33.73	32.56	20.28	1.54	0.26	32.92	33.90	32.68	1.78	21.08	0.07	0.04	28.07	30.00	0.00	0.73	0.00	0.62
MnO	1.85	1.27	2.48	1.68	0.08	0.06	0.00	4.03	1.77	4.22	0.01	0.16	0.00	0.00	10.78	7.41	0.00	0.00	0.19	0.27
MgO	2.60	4.49	3.45	3.47	8.49	0.88	0.00	2.94	3.78	3.02	0.51	8.09	0.00	0.00	3.07	4.58	0.00	0.66	0.00	0.00
CaO	6.09	3.55	2.48	3.83	0.10	0.00	5.08	2.25	2.24	2.31	0.02	0.05	6.64	6.23	0.55	0.45	0.00	0.00	2.20	0.13
Na_2O	0.00	0.31	0.00	0.00	0.32	0.44	8.72	0.13	0.00	0.00	0.44	0.31	6.80	7.66	0.00	0.00	1.40	0.44	10.03	0.00
K_2O	0.14	0.23	0.00	0.02	9.12	10.06	0.08	0.10	0.00	0.02	10.46	9.64	0.36	0.18	0.00	0.02	14.59	11.03	0.14	0.24
Totals	99.910	99.677	99.991	99.901	96.777	95.096	100.040	100.06	99.49	100.00	95.00	96.17	100.66	100.73	100.30	100.53	100.59	95.63	99.29	99.58
Oxygens	12	12	12	12	11	11	8	12	12	12	11	11	8	8	12	12	8	11	8	5
Si	2.969	3.067	3.017	3.015	2.722	3.134	2.766	2.985	3.003	2.989	3.076	2.678	2.521	2.715	2.989	2.965	2.973	3.075	2.909	0.986
Ti	0.000	0.000	0.002	0.004	0.185	0.069	0.000	0.000	0.012	0.000	0.060	0.195	0.000	0.003	0.000	0.008	0.016	0.078	0.000	0.000
Al	1.945	1.878	1.920	1.944	1.662	2.643	1.224	1.951	1.931	1.958	2.732	1.653	1.558	1.291	1.969	1.945	1.023	2.728	1.091	1.999
Fe^{3+}	0.131	0.059	0.043	0.021	0.000	0.000	0.010	0.111	0.037	0.065	0.000	0.000	0.003	0.001	0.054	0.111	0.000	0.000	0.000	0.000
Fe^{2+}	1.982	2.006	2.223	2.159	1.271	0.086	0.000	2.103	2.247	2.135	0.100	1.346	0.000	0.000	1.837	1.887	0.000	0.041	0.000	0.014
Mn	0.125	0.085	0.169	0.114	0.005	0.003	0.000	0.274	0.121	0.288	0.001	0.010	0.000	0.000	0.736	0.500	0.000	0.000	0.007	0.006
Mg	0.310	0.531	0.413	0.414	0.949	0.087	0.000	0.352	0.454	0.362	0.051	0.921	0.000	0.000	0.369	0.544	0.000	0.065	0.000	0.000
Ca	0.523	0.302	0.213	0.328	0.008	0.000	0.241	0.194	0.193	0.199	0.001	0.004	0.315	0.294	0.047	0.038	0.000	0.000	0.104	0.004
Na	0.000	0.048	0.000	0.000	0.047	0.057	0.749	0.020	0.000	0.000	0.057	0.046	0.584	0.654	0.000	0.000	0.124	0.057	0.860	0.000
K	0.014	0.023	0.000	0.002	0.872	0.854	0.005	0.010	0.000	0.002	0.893	0.939	0.020	0.010	0.000	0.002	0.850	0.934	0.008	0.008
Sum	7.999	7.999	8	8.001	7.721	6.933	4.995	8.000	7.998	7.998	6.971	7.792	5.001	4.968	8.001	8.000	4.986	6.978	4.979	3.018
X_{Mg}	0.135	0.209	0.157	0.161	0.427	0.503		0.143	0.168	0.145	0.338	0.406			0.167	0.224		0.613		
Fe^{3+}%	0.1	0	0	0	0	0		0.1	0	0	0	0			0	0.1		0		0
Alm%	68.1	69.4	73.5	71.5				72.7	74.4	71.7					61.6	63.9				
Sps%	4.2	2.8	5.6	3.8				9.1	4.0	9.6					24.5	16.7				
Prp%	10.3	17.7	13.8	13.8				11.7	15.1	12.1					12.3	18.1				
Grs%	17.4	10.1	7.1	10.9				6.5	6.4	6.6					1.6	1.3				
X_{Ca}							0.242						0.343	0.307			0		0.107	
Pl Al/Si							0.226						0.517	0.289			0.023		0.091	

Note: Mineral abbreviations follow Whitney and Evans (2010). Int—intermediate.

There is evidence for a heterogeneous degree of melting throughout the Core Unit, due to lithological and bulk compositional controls because of repetition of infertile orthogneissic basement along with more fertile metasedimentary horizons, due to prograde thrusting. Samples TL66 and TL15 outcrop as stromatic migmatites with centimeter-scale folded leucosome and melanosome banding, whereas samples TLN18 and TLN20A represent diatexites. Melanosome foliations are defined mostly by muscovite, biotite, fibrolite (fibrous sillimanite), relict kyanite, and in some samples peritectic K-feldspar (Figs. 13G–13I). Leucosome segregations contain around equal proportions of quartz and plagioclase, with lesser amounts of biotite, muscovite, fibrolite, garnet, and ilmenite, while K-feldspar occurs in other samples (e.g., TL59, TLN18, TLN34, TLN35). Accessory minerals include tourmaline, apatite, magnetite, pyrite, zircon, and monazite. Leucosome segregations comprise ~10%–20% of the migmatite sequence in outcrop. Diatexite only occurs at the deepest levels and has foliations defined by schollen of biotite and some relict muscovite, with leucosomes characterizing larger volumes of the rock (>20%).

Garnet occurs in both the leucosome and melanosomes as small idioblastic porphyroblasts <1 mm in diameter, displaying subhedral to anhedral faces (Figs. 13A, 13E, and 13F). In sample TL15, leucosome garnet preserves rotational inclusion trails, which define the S_{2a} fabric, that rotate into alignment with the external matrix S_{2b} fabric toward its rims (Figs. 14A and 14J), indicating garnet grew synkinematically with the development of these prograde features. However, many of these porphyroblasts in sillimanite-grade samples are fractured and filled by biotite and muscovite intergrowths (Fig. 13F). In samples TLN34 and TL66, garnet is almost compositionally homogeneous (Fig. 15F; Data Repository Item [see footnote 1]). Muscovite in sample TL59 and TL66 occurs similarly as laths with associated fibrolite or as symplectic intergrowths with quartz (Figs. 13E–13H). These intergrowths are often associated with either biotite-quartz symplectite or myrmekite (plagioclase-quartz intergrowths). Secondary muscovite in leucosomes is oriented randomly relative to the foliation and fibrolitic sillimanite in the matrix, and on the margins of leucosomes, it is typically surrounded by coarse-grained, crosscutting muscovite (Figs. 14E–14F; Spear et al., 1990). Biotite occurs as individual crystals in the leucosome, as part of the melanosome foliation, and also as symplectic intergrowths with quartz, but it shows no significant compositional variation between these petrographic positions with Mg/(Mg + Fe). In kyanite-grade

TABLE 5. SUMMARY PRESSURE-TEMPERATURE (*P-T*) RESULTS FROM THERMOBAROMETRY AND THERMOCALC DS-62 AV-PT AND PSEUDOSECTION CALCULATION FOR ALL NAXOS SAMPLES

Summary *P-T* results					Thermocalc AvPT							Ti-in-Bt	Pseudosection	
Unit	Sample	Rock type	Mineralogy	Location	Notes	XH_2O	End members included	avT ± 1 S.D. (°C)	avP ± 1 S.D. (kbar)	Corr	*P-T* interpretation	temp. range (°C)	*P* ± 1 S.D. (kbar)	*T* ± 1 S.D. (°C)
Zas Unit	TLN54	Glaucophane rutile schist	Gln, Czo, Qtz, Ms, Phg, Pg, Chl, Cal, Rt, Sph, Pl	37.036781°N, 25.493024°E	with ab	0.99	gln-fgln-ms-cel-fcel-pa-clin-ab-q-H_2O-CO_2-cc-rt-sph	483 ± 13	12.6 ± 0.8	0.951	Postpeak M1 albite in	–	14.5 ± 0.5	470 ± 30
Zas Unit	TLN25	Epidote-calc-schist	Gln, Act, Tc, Czo, Qtz, Ms, Pg, Ep, Chl, Cal, Rt, Sph, Bt, Pl	36.999229°N, 25.486564°E	with ab	0.99	gln-fgln-rieb-tr-ts-daph-ames-ep-ta-fta-tats-clin-ab-q-H_2O-CO_2-cc-rt-sph	465 ± 34	10.1 ± 1.9	0.979	Retrograde M1 albite in	–	–	–
Zas Unit	TLN26	Mica-calc-schist	Act, Czo, Ms, Phg, Ep, Bt, Chl, Cal, Rt, Sph, Qtz, Pl	36.935434°N, 25.475521°E	with ab	0.99	mu-cel-fcel-pa-phl-ab-ilm-sph-rt-cc-CO_2-H_2O	473 ± 35	11.6 ± 2.2	0.988	Postpeak M1 albite in	–	–	–
Koronos Unit	TL67	Kyanite gneiss	Grt, Ky, Bt, Ms, Kfs, Pl, Rt, Qtz, Tur, ilm	37.08808°N, 25.49797°E	Grt rim	0.50	prp-grs-alm-mu-cel-fcel-phl-ann-east-an-ky-q	682 ± 38	11.4 ± 1.0	0.686	Peak M2	616–731	10.0 ± 0.5	670 ± 20
					Grt core-int	0.90	prp-alm-phl-ann-east-mu-ky-sill-q-rt-ilm	622 ± 68	9.4 ± 1.3	0.778	Prograde M2	616–732	6.1 ± 0.5	600 ± 15
					Grt rim	1.00	prp-grs-phl-ms-cel-an-q-ky	675 ± 83	10.8 ± 1.6	0.854	Peak M2	616–733	10.0 ± 0.5	670 ± 20
Koronos Unit	TLN22	Kyanite schist	Grt, Ky, Bt, Ms, Kfs, Pl, Rt, Qtz, Tur, ilm	37.127084°N, 25.524576	Grt rim	1.00	prp-grs-alm-mu-cel-fcel-phl-ann-an-ky-q	607 ± 67	9.3 ± 1.3	0.770	Prograde-peak M2	458–699	–	–
Koronos Unit	TLN16	Biotite-schist	Grt, Bt, Kfs, Pl, Qtz, Rt, Ilm	37.100794°N, 25.515643°E	Grt rim	0.50–1.00	prp-grs-alm-phl-ann-east-mu-cel-fcel-an-ky-ilm-rt	534 ± 134	7.2 ± 2.1	0.61	Prograde M2	578–740	–	–
					Grt rim	0.50–1.00	prp-grs-alm-phl-ann-east-mu-cel-fcel-an-ky-sill-ilm-rt	678 ± 122	7.3 ± 2.5	0.986	Postpeak M2-high temp (M3)	578–740	–	–
Koronos Unit	TLN21	Kyanite-sillimanite-gneiss	Grt, Ky, Sill, Bt, Ms, Kfs, Pl, Rt, Qtz, Tur, ilm, Ap, Chl	37.125787°N, 25.518516°E	Grt rim	1.00	prp-alm-phl-ann-east-mu-cel-fcel-ky-sill-q-rt-ilm	695 ± 67	7.6 ± 1.4	0.984	Postpeak M2-high temp (M3)	586–713	–	–
					Grt rim	1.00	prp-alm-phl-ann-east-mu-ky-sill-q-rt-ilm	625 ± 48	6.1 ± 1.0	0.985	Postpeak M2 re-equilibration (M3)	586–713	–	–
Koronos Unit	17TL75	Garnet amphibolite	Grt, Hb, Pl, ilm, Qtz, Chl, Rt	37.125993°N, 25.517824°E	Grt int-rim	1.00	prp-alm-grs-tr-fact-ts-parg-rt-q-an-ab	703 ± 69	8.9 ± 1.1	0.819	Peak M2	–	–	–
Core Unit	TL66	Sillimanite-migmatite	Grt, Sill, Bt, Ms(secondary), Pl, ilm, Qtz, Kfs	37.08880°N, 25.47022°E	Grt rim	1.00	prp-grs-alm-phl-ann-east-mu-cel-fcel-an-ky-sill-ilm-rt	742 ± 39	7.5 ± 1.2	0.812	Peak M3 sillimanite-grade melting	651–751	5.5 ± 0.6	720 ± 25
					Grt core	1.00	prp-grs-alm-phl-ann-east-mu-cel-fcel-an-ky-sill-ilm-rt	726 ± 37	7.8 ± 1.1	0.774	M2 kyanite-grade melting	651–751	6.0 ± 0.6	725 ± 25
Core Unit	TL15	Kyanite-migmatite	Grt, Ky, Bt, Ms, Pl, ilm, Qtz	37.08022°N, 25.47802°E	Grt rim	1.00	prp-alm-phl-ann-east-ms-cel-q-ky-rt-ilm	710 ± 31	9.7 ± 1.1	0.693	Peak M2 kyanite-grade melting	589–690	8.0 ± 0.4	690 ± 15
					Grt int	1.00	prp-grs-alm-phl-ann-east-ms-cel-fcel-an-q-ky-rt-ilm	684 ± 118	8.1 ± 1.3	0.517	Prograde M2 onset of melting	589–690	7.5 ± 0.3	710 ± 20
Core Unit	TL59	Garnet-biotite gneiss	Grt, Bt, Pl, Ms, ilm, Qtz, Tur	37.06824°N, 25.44170°E	Grt rim	1.00	prp-grs-alm-phl-ann-east-ms-cel-fcel-an-q-rt-ilm	675 ± 32	7.7 ± 1.1	0.673	Peak M2 onset of melting	612–674	7.7 ± 0.5	690 ± 25
Core Unit	TLN35	Muscovite-dehydration migmatite	Grt, Bt, Kfs, Pl, Qtz, ilm, Ap, minor secondary Ms	37.16228°N, 25.50452°E	Grt int	1.00	prp-grs-alm-phl-ann-east-ms-cel-fcel-an-q-ky-sill-rt-ilm	629 ± 47	6.2 ± 1.0	0.983	Postpeak M3 retrograde re-equilibration	615–709	–	–
Core Unit	TLN34	Sillimanite-migmatite	Grt, Sill, Bt, Kfs, Pl, Qtz, ilm, Ap, minor secondary Ms	37.16236°N, 25.50238°E	Grt int	1.00	prp-grs-alm-phl-ann-east-ms-cel-fcel-an-q-ky-sill-rt-ilm	598 ± 66	5.5 ± 1.3	0.98	Postpeak M3 retrograde re-equilibration	570–712	–	–

Note: Mineral abbreviations follow Whitney and Evans (2010). See Henry et al. (2005) for details of Ti-in-biotite thermometry. Pseudosection results using Thermocalc v.3.40i and dataset62 (Powell and Holland, 1988; Holland and Powell, 2011), see text for further details on activity models used.

migmatites (e.g., TL15), kyanite is associated with the S_2 foliation, which is folded by F_3 folds (Figs. 14B–14D), indicating upright F_3 folding postdated kyanite growth and occurred after the rocks attained their peak pressures.

Textures of Sillimanite-Grade Migmatites

At midcrustal pressures in the upper amphibolite facies, the first appearance of anatectic melt is usually triggered by the intersection of the wet granite or pelite solidus with destabilization of prograde muscovite through the following hydrous melting reactions (Pëto, 1976; St-Onge, 1984; Patiño Douce and Harris, 1998; Weinberg and Hasalová, 2015):

$$\text{muscovite + quartz + plagioclase + K-feldspar} + H_2O \rightarrow \text{melt}, \quad (2)$$

$$\text{muscovite + quartz + plagioclase} + H_2O \rightarrow \text{aluminosilicate + melt}. \quad (3)$$

However, these reactions produce very small volumes of melt, unless a substantial external supply of fluid is available (Thompson, 1982; Pattison and Tracy, 1991). Nevertheless, volumetrically significant melting can occur with continued prograde metamorphism above the wet solidus via the fluid-absent muscovite dehydration melting reaction (Eq. 4). Due to the positive *P-T* slope of this reaction, at lower temperatures and pressures, K-feldspar is also produced by its vapor-present equivalent reaction (Eq. 5) at subsolidus temperatures. In the field, these reactions are often referred to as the "upper sillimanite" or "second sillimanite isograd" (Evans and Guidotti, 1966) due to the formation of a K-rich neosome (García-Casco et al., 2003):

$$\text{muscovite + quartz} \rightarrow \text{K-feldspar + aluminosilicate + melt}, \quad (4)$$

$$\text{muscovite + quartz} \rightarrow \text{K-feldspar + aluminosilicate} + H_2O. \quad (5)$$

Several authors have observed that K-feldspar is commonly absent from sillimanite-grade migmatites despite being present at peak conditions, due to replacement by secondary muscovite in the back reaction during cooling (Ashworth, 1975; Tippett, 1980). By identifying different generations of muscovite through various petrographic characteristics, secondary muscovite can be distinguished. Tyler and Ashworth (1982) suggested that prograde (primary) muscovite that survives the partial melting process often occurs as flakes orientated in the melanosome foliation. Retrograde muscovite occurs as large lath-like porphyroblasts containing sillimanite, or as symplectic intergrowths with quartz (Figs. 13E–13H; Ashworth, 1975, 1979; Tippett, 1980). Textural features in sample TL66 include muscovite laths containing numerous fibrolite inclusions and muscovite-quartz symplectite and intergrowths of sillimanite-quartz "faserkiesel," which are typical of retrograde replacement of K-feldspar at sillimanite-grade conditions (Figs. 13E–13G; Evans and Guidotti, 1966; Ashworth, 1975; Tippett 1980; Brown, 2002), i.e., the reversal of the muscovite dehydration melting reaction.

Although peritectic K-feldspar is commonly lacking in the Naxos migmatites due to hydrous melting textures and retrograde replacement by secondary muscovite, leucosomes in migmatites from deep levels are volumetrically abundant in outcrop, representing ~15%–25% volume proportion of rock. This volume of melt greatly exceeds the proposed melt connectivity threshold of 7%–10% that allows melt extraction in such lithologies (Rosenberg and Handy, 2005). However, it has been shown that the observed leucocratic component of migmatites does not directly correlate with actual quantities of melting. At shallow dome levels, rocks that have been described as leucosomes, leucogneiss, and diatexites are interpreted here as orthogneiss basement that coarsened upon experiencing small degrees of partial melting (B. Dyck, 2016, personal commun.). This has major implications for the proposed mechanisms that drove migmatite doming, as the weakening effect depending on the extent of partial melting may have been extremely overestimated. At structurally high levels of the dome, the stability of primary muscovite within the melanosomes supports this interpretation, as they did not experience muscovite dehydration melting (the first major melt-producing reaction). Although diatexites occur on Naxos, they are confined to fertile lithologies at deeper levels upon crossing the K-feldspar isograd.

Some inferences about the temperature of mineral growth can be made using the compositional characteristics of different mineral generations. Prograde muscovite commonly contains higher paragonite content than retrograde muscovite that has replaced K-feldspar (Evans and Guidotti, 1966; Ashworth, 1975). Generally, low Si contents (<3.10 pfu per 11 oxygens) combined with high Ti contents (up to 0.08 pfu) are characteristic of high-grade and magmatic muscovite (Miller et al., 1981; Guidotti, 1984). In all analyzed samples, leucosome muscovite is low in Si and contains a moderate to high Ti content (~0.04–0.10; Fig. 15), indicating that they formed during melt crystallization or retrogressively while still at high temperature. Compositional zoning profiles in garnet give further support for high-grade metamorphic conditions, as inferred from compositional and textural characteristics in muscovite. Several authors have demonstrated that garnet compositional zoning profiles form principally as a function of changes in pressure and temperature conditions during growth (e.g., Tracy et al., 1976; Spear and Selverstone, 1983; St-Onge, 1987). During prograde metamorphism in a pelitic bulk composition, garnet preferentially fractionates Mn into core regions, and therefore spessartine content decreases toward rims as a result of progressive Mn depletion in the reacting matrix (Hollister, 1966). However, in the Naxos migmatites, garnet contains spessartine profiles that are homogeneous or concave upward, with increasing Mn content from core to rim. The length scale of Mn (and Mg, Fe, and Ca) zonation within the garnets is less than the diffusional length scale (up to 3 mm) suggested by >5 m.y. residence time at peak temperatures >650 °C (Caddick et al., 2010). These factors indicate that preservation of the prograde growth history will be modified somewhat by diffusion, whereas peak conditions will be preserved by thermal re-equilibration (Woodsworth, 1977; Spear, 1993). Nevertheless, the shape and trends of garnet profiles will be somewhat preserved if peak conditions were attained for only a geologically brief time, and therefore insight into the prograde metamorphic history of the Core Unit may be obtained. Therefore, in the following, we take peak pressure estimates as a minimum depth of burial.

Textures of Kyanite-Grade Migmatites

Kyanite-grade migmatites (e.g., TL15) occur at higher structural levels of the dome and record the earlier prograde history. Texturally, these are stromatic migmatites with distinct leucosomes highlighting centimeter-scale ptygmatic flow folding during anatectic conditions. In these samples, melanosomes preserve the S_{2a} crenulation cleavages and S_{2b} spaced foliations along cleavage domains similar to the overlying Koronos Unit (Figs. 13C, 13D, and 13H). Kyanite is bladed and lies in the folded S_2 foliation, indicating that it grew in Al-rich bands prior to anatectic deformation associated with upright F_3 folding (Figs. 13B–13C). In contrast, some biotite and secondary muscovite in the melanosome are orientated axial planar to and crosscut the folding, indicating they postdate deformation and are mainly retrogressive features associated with hydration contemporaneous with regional NNE-SSW extensional exhumation. This specimen does not exhibit any of the K-feldspar replacement features described above, suggesting that its leucosomes were never of a granitic composition, and consequently their formation must be a result of a K-feldspar–absent melting reaction. When H_2O is in excess, K-feldspar–absent reactions extend to lower temperatures (García-Casco et al., 2001, 2003; Cruciani et al., 2008); increasing pressure also favors fluid-saturated melting reactions before reaching conditions that favor dehydration melting during typical prograde metamorphism (Cruciani et al., 2008). Due to an inverse correlation between pressure and plagioclase stability, an increase in the plagioclase/muscovite ratio consumed in melting reactions with increasing pressure (Patiño Douce and Harris, 1998), and increasing H_2O activity lead to preferential solution of plagioclase components by lowering the plagioclase + quartz solidus (Conrad et al., 1988). These factors result in a significant shift of products of H_2O-fluxed melting toward tonalitic/trondhjemitic compositions and are typical of fluid-rich environments at high-pressure and low-temperature conditions.

Garnet within leucosome segregations in sample TL15 often demonstrates idioblastic faces (Fig. 13J), which, as a microstructural feature in migmatites, is usually interpreted to represent growth in the presence of melt (Whitney and Irving, 1994; Guilmette et al., 2011). This inference is further supported by different core and rim compositions in large porphyroblasts, and evidence for prograde growth zoning during development of S_2 (Figs. 13A, 15C, and 15D), suggesting that garnet growth occurred in two stages, each at different *P-T* conditions (Spear, 1993). In the case of almandine and grossular content in the measured profile, rim compositions are separated from core compositions by an abrupt step and only sometimes show a smooth transition (Figs. 15C and 15D), with the latter interpreted as a diffusion profile that formed between two initially distinct compositional domains (e.g., Caddick et al., 2010). This two-stage growth scenario is further supported by zonation in both Y and Yb (Fig. 15C), which show a stepwise decrease from core to rim, and small leucosome garnet grains that have similar compositions to rims of large porphyroblasts, indicating growth in the presence of melt. Diffusion has only modified the outermost ~100 µm of the rim, as demonstrated by an inflection in spessartine content, suggesting core–inner rim zoning was prograde (e.g., Caddick et al., 2010). For these reasons, we conclude that sample TL15 best records the prograde evolution of the Core Unit and the initial stages of partial melting at higher-pressure M_2 conditions, through the following K-feldspar–absent hydrous reaction as proposed by García-Casco et al. (2001) for similar kyanite-bearing pelitic migmatites:

$$\text{biotite + muscovite + plagioclase + quartz} + H_2O \rightarrow \text{garnet + kyanite + melt.} \quad (6)$$

PRESSURE-TEMPERATURE CONDITIONS OF METAMORPHISM

Several forms of thermobarometry were used in this work to constrain the *P-T* conditions of metamorphism on Naxos, including the Ti-in-biotite thermometer of Henry et al. (2005), the garnet–aluminum silicate–plagioclase–quartz (GASP) barometer, the garnet-biotite thermobarometer (Spear, 1993; Bhattacharya et al., 1992; Holdaway, 2000), and AvPT (Powell et al., 1998) using THERMOCALC version 3.40i, which was employed using characteristic end members for each sample. The results are displayed in Figure 16. Activities of solid-solution end members were calculated (Table 5) using AX (Holland, 2009). The results systematically demonstrate that there are two distinct *P-T* populations on Naxos. M_1 blueschist-facies *P-T* conditions are exclusively confined to the Zas Unit (Fig. 16A, blue circles) and give typical *P-T* results of 12.3 ± 0.8 kbar and 483 ± 13 °C (TLN54). In contrast, an upper-amphibolite-facies M_2-M_3 population is recorded within the Koronos and Core Units (Fig. 16A, green and red circles, respectively). These rocks typically record increasing pressure and temperature conditions from garnet core to rim. Kyanite-bearing M_2 assemblages record higher pressures, up to 11.4 ± 1.0 kbar and 682 ± 38 °C (TL67). Sillimanite-bearing M_3 assemblages record re-equilibration at lower-pressure conditions, i.e., 7.5 ± 1.2 kbar and 742 ± 39 °C (TL66). Within these units, prograde garnet compositions show increases in both pressure and temperature from core to rim diagnostic of crustal thickening and do not represent isobaric heating, as previously inferred (Buick and Holland, 1989; Buick, 1991a, 1991b). However, the nature of the *P-T* path leading up to and during peak anatectic conditions is poorly constrained using this method. This is because conventional thermobarometry is largely ineffective at constraining peak *P-T* conditions in high-grade and/or partially melted rocks (e.g., Halpin et al., 2007; Indares et al., 2008; Palin et al., 2013) owing to changing mineral compositions due to retrograde diffusion (Kohn and Spear, 2000; Pattison and Begin, 1994, 2003), and it has large associated uncertainties (typically ±50 °C and ±1 kbar at 1 standard deviation; Powell and Holland, 2008; Palin et al., 2016). As such, phase diagram modeling (pseudosection construction) was employed herein as the main investigative tool to harness *P-T* information, which has significantly smaller uncertainties.

Pseudosections were constructed using THERMOCALC version 3.40i and internally consistent thermodynamic data set ds-62 (Powell and Holland, 1988; Holland and Powell, 2011). Modeling of metasediments TL67, TL15, and TL66 was performed in the MnO–Na_2O–CaO–K_2O–FeO–MgO–Al_2O_3–SiO_2–H_2O–TiO_2–O (MnNCKFMASHTO) system using the following activity-composition relations: silicate melt (White et al., 2007), cordierite (Mahar et al., 1997; Holland and Powell, 1998), garnet and ilmenite (White et al., 2005), orthopyroxene (White et al., 2002), chlorite (Mahar et al., 1997; Holland et al., 1998), Ti-bearing biotite (White et al., 2007), muscovite (Coggon and Holland, 2002), K-feldspar and plagioclase (Holland and Powell, 2003), and magnetite (White et al., 2002). Modeling of metabasic lithologies in TLN54 was performed in the MnO-absent NCKFMASHTO system, with the additional usage of the omphacitic clinopyroxene and amphibole activity-composition relations of Green et al. (2016). The pure phases andalusite, kyanite, sillimanite, rutile, quartz, and H_2O were considered in all cases. The bulk-rock suprasolidus water content of migmatitic units was fixed on an individual basis in order to allow minimal fluid saturation at the wet solidus, here defined as ~1 mol% free H_2O.

Detailed investigation into the prograde evolution and *P-T* conditions leading up to peak metamorphism was achieved by investigating compositional isopleths for pyrope and grossular content in garnet. Since these isopleths vary to first order with changes in pressure and temperature and commonly intersect at high angles, they specify unique intersection points with a high degree of confidence for tracking garnet composition evolution in *P-T* space. The intersections of isopleths representing measured compositions are represented by shaded boxes indicating uncertainties at the 1σ level calculated by THERMOCALC.

TLN54: Retrogressed Blueschist (M_1 Zas Unit)

Figure 17 shows the calculated *P-T* pseudosection for blueschist-facies sample TLN54. Using the methods described in the Data Repository Item (see footnote 1), and the absence of carbonate phases for the modeled area, the fluid was assumed to have pure H_2O in excess. The observed peak M_1 assemblage Gl-Ms-Chl-Rt-Sph-Qtz was calculated to be stable at ~11–15 kbar and ~400–520 °C. Glaucophane isopleths of z(gl) = 0.96, f(gl) = 0.02–0.03, and a(gl) = 0.05–0.06 suggest that peak M_1 *P-T* conditions reached at least 14.5 ± 0.5 kbar and 470 ± 20 °C. Model amphibole compositions match well with observed sodic amphibole analytical data from both samples TLN54 and TLN25 (Fig. 15). Ranges of AvPT results from samples TLN54, TLN25, and TLN26 from the Zas Unit record

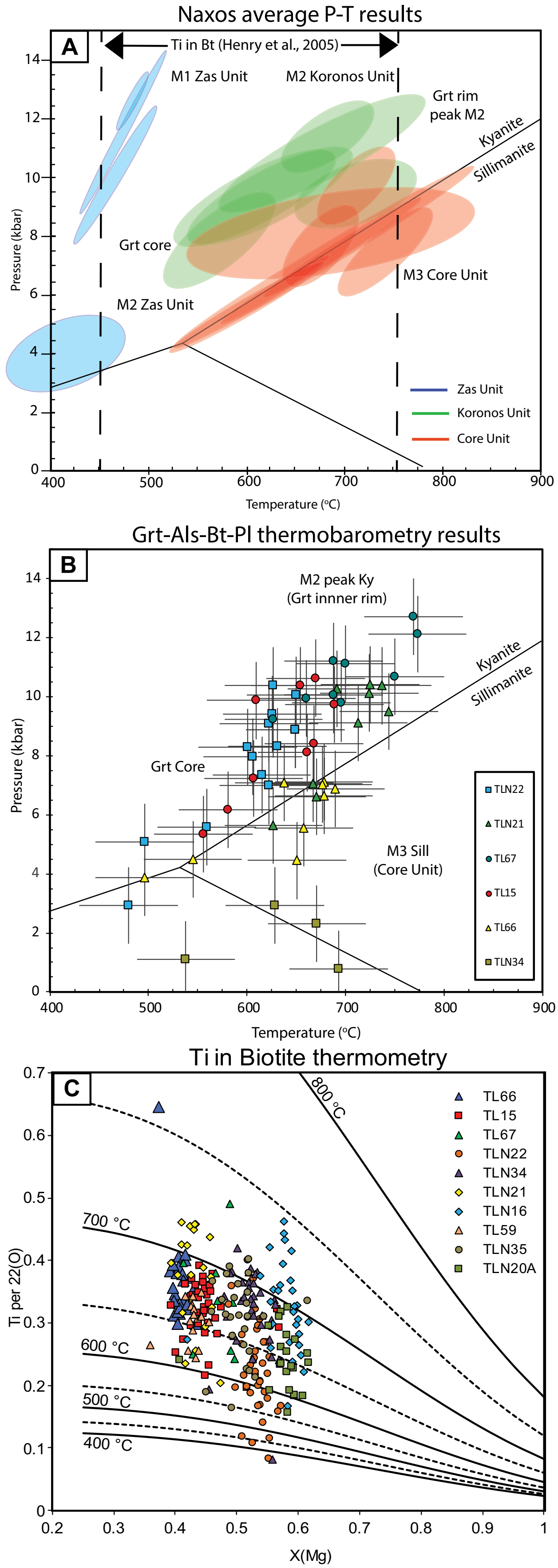

Figure 16. Visualization of thermobarometry results from samples analyzed in this study. (A) Av-PT results using THERMOCALC version 3.40i for all samples with overlaid Ti-in-biotite thermometry results (see Table 5; see Data Repository Item [text footnote 1] for more discussion). (B) Results from Grt-Ky/Sill-Plag-Qtz geobarometry (Spear, 1993) combined with Grt-Bt Fe/Mg exchange thermometry (Bhattacharya et al., 1992) showing an increase in both pressure and temperature from garnet core to rim; TLN34 and TL66 record lower pressures due to diffusional homogenization of garnet compositions. (C) Ti-in-biotite thermometry (Henry et al., 2005) results for Naxos high-grade samples (Koronos and Core Unit); note the range in temperatures due to thermal re-equilibration of particularly high-grade rocks during retrogression. Mineral abbreviations follow Whitney and Evans (2010).

minimum *P-T* conditions of around 12 kbar and 450 °C, i.e., a similar result to peak metamorphic conditions of ~13 kbar and ~450 °C suggested by Avigad (1998) for a jadeite-bearing blueschist within the Zas Unit, and comparable to the recently published results of 15.5 kbar and 576 °C by Peillod et al. (2017).

TL67: Kyanite Gneiss (M_2 Koronos Unit)

Sample TL67 reveals the prograde and peak *P-T* conditions for the Koronos Unit and is shown in Figure 18. Using a pure H_2O aqueous fluid, the predicted assemblages are incompatible with the observed textures and assemblages, particularly, the lack of evidence for melting and subsolidus K-feldspar. Upon careful observation, the existence of graphite and dark CO_2 fluid inclusions in garnet and quartz indicate circulation of CO_2 fluids during peak metamorphism. A reduction in water activity, $a(H_2O)$, causes the dehydration equilibria that underlie prograde processes in metasedimentary rocks to be displaced to lower temperature. Although estimating the actual value of water activity in a rock system is difficult, some constraints can be placed if the rock contains graphite. The coexistence of solid carbon with a C-H-O fluid has three degrees of freedom, so that one further constraint, such as oxygen fugacity, potentially allows the concentration of all C-H-O fluid species to be calculated at any given *P* and *T*. Therefore, an investigation of the effect of water activity on the calculated phase relations was conducted (Fig. 18B). Using this method, a reduced $a(H_2O) = 0.5$ was chosen to represent fluids during peak metamorphism, which corresponds to the findings of previous studies of metamorphic fluids on the island (Kreulen, 1980; Baker et al., 1989). This has been shown to shift the solidus to higher temperatures (Pëto, 1976; Peterson and Newton, 1989; Stevens and Clemens, 1993; Weinberg and Hasalová, 2015), stabilizing K-feldspar at subsolidus temperatures as shown in Figures 18B and 18C (Newton, 1989).

For a localized Al-rich domain, compositional isopleths representative of garnet core domains (~10% pyrope and ~11% grossular) intersect at ~6.5 kbar and 550 °C in the assemblage field Grt–Ms–St–Bt–Pl–Ilm–Qtz–H_2O, and those representative of the inner rim (14%–15% pyrope and 13% grossular) intersect at 10.5 kbar and 675 °C in the assemblage field Grt–Ms–Bt–Pl–Ilm–Rt–Qtz–H_2O. This is consistent with temperature estimates of 630–710 °C calculated from the Ti concentration of biotite (Henry et al., 2005) and similar to pressures calculated by Duchene et al. (2006); therefore, we take these estimates to represent peak M_2 *P-T* conditions. Garnet outermost rims (13%–14% pyrope and 10% grossular) have isopleth intersections at 7.5 kbar and 655 °C and cross the muscovite dehydration reaction to produce K-feldspar. This is associated with an increase in garnet mode, which is consistent with garnet rims crosscutting the S_2 kyanite-grade fabric. Garnet-rim upward inflections in Fe/(Fe + Mg) and spessartine content are also characteristic features of retrograde replacement by biotite (Kohn and Spear, 2000), and they suggest some garnet was resorbed during retrogression.

TL15: Kyanite Migmatite (Core Unit): Peak (M_2) Kyanite-Grade Conditions

Sample TL15 records the prograde evolution of the Naxos migmatites, and the corresponding pseudosection is shown in Figure 19. Isopleths for garnet core compositions (10% pyrope and 13%–16% grossular) indicate prograde metamorphism through the Grt–Ms–Bt–Pl–Ilm–Chl–Qtz–H_2O assemblage field at ~6 kbar and ~550 °C. During prograde metamorphism, significant garnet is predicted to have formed via staurolite breakdown (e.g., Eq. 1). Garnet compositions just within the inner diffusion-affected porphyroblast rims provide minimum constraints on the conditions of peak metamorphism (Caddick et al., 2010). Isopleths for 17% pyrope and 9–10% grossular intersect at ~9.5 kbar and 700 °C in the Grt–Ms–Bt–Pl–Ilm–Qtz–Liq–H_2O–Ky assemblage field, indicating that prograde metamorphism occurred along a heating path that crossed the water-saturated solidus (Eq. 6) at a minimum of 8 kbar and 680 °C. High-pressure melting is in agreement with the presence of prograde muscovite, bladed kyanites, and small proportions (1%–4%) of melt distributed along rounded grain boundaries, although peak pressures may have been higher due to diffusional re-equilibration (Caddick et al., 2010). As this rock lies within the same unit as sillimanite-grade migmatites, it is likely that this rock experienced the same prograde path as the underlying sillimanite-bearing migmatites experienced before obtaining higher temperatures. Due to the lack of sillimanite in this rock, but locations within tens to hundreds of meters of the sillimanite isograd, this rock may have crossed the kyanite-sillimanite transition at peak conditions via an indirect Carmichael reaction scheme, but it preserves no textural evidence owing to its sluggish reaction kinetics. Overall, peak *P-T* conditions of ~730 ± 20 °C and 9.5 ± 0.8 kbar obtained from sample TL15 are consistent with peak conditions for sample TL59 (see Data Repository Item [see footnote 1]). Therefore, burial of the Core Unit occurred under kyanite-

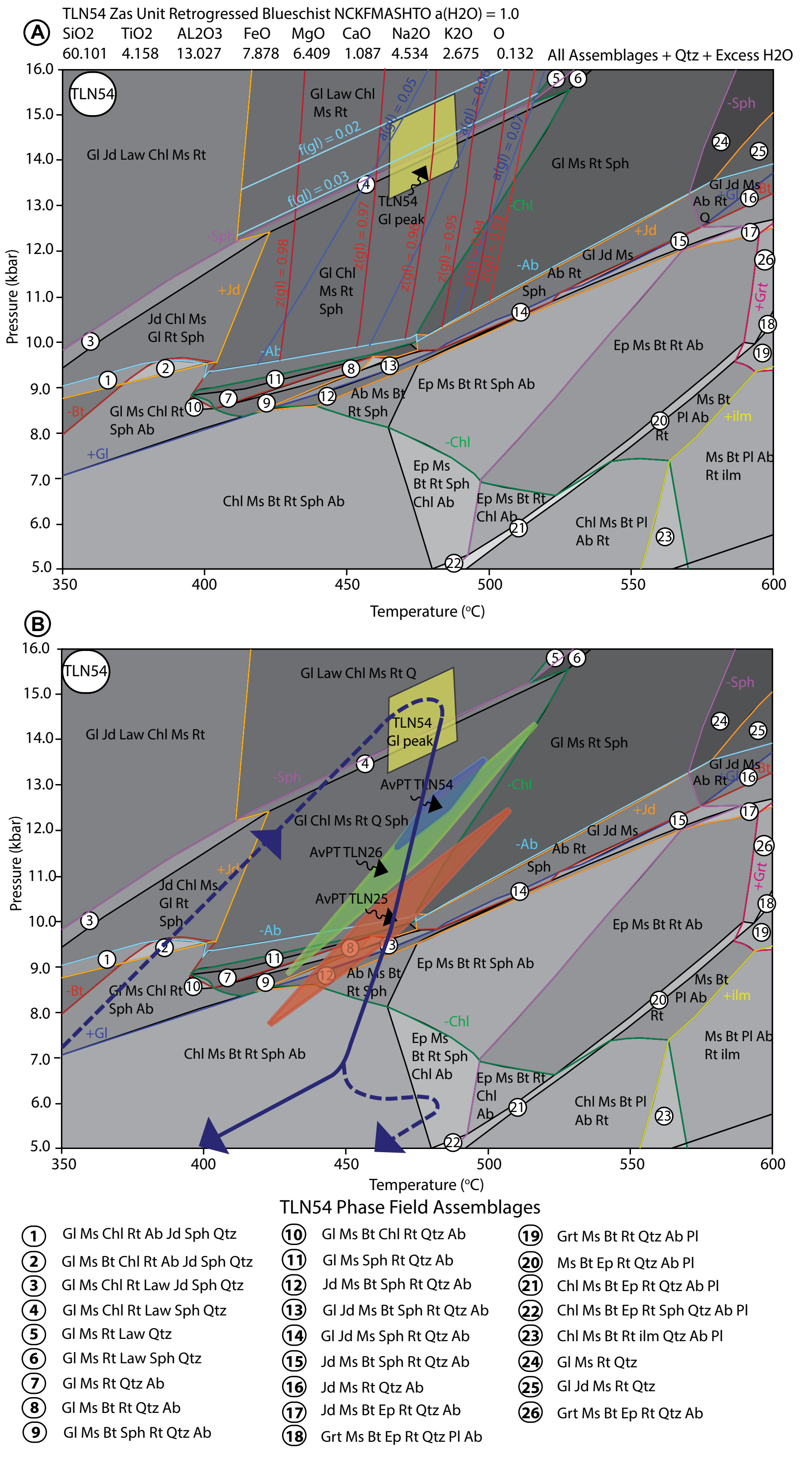

Figure 17. Pressure-temperature (*P-T*) pseudosection for sample TLN54 from the Zas Unit, using the observed bulk composition, where blue arrows and dashed lines present suggested *P-T* paths taken by this rock. (A) Glaucophane compositional isopleths of f(gl), z(gl), and a(gl) intersect at peak conditions of ~14.5 kbar and 470 °C. (B) Overlain Av-PT results from this and other samples from the Zas Unit. Mineral abbreviations follow Whitney and Evans (2010).

grade (M_2) conditions of 680–730 °C and minimum pressures of 8–10 kbar, similar to conditions of 670 ± 31 °C and 10 ± 0.5 kbar in the overlying Koronos Unit. This should be taken as a minimum pressure, and the apparent pressure inversion between the Core Unit and the Koronos Unit could be explained by diffusional homogenization between two contrasting garnet compositions at high-grade conditions. The textural relationships of kyanite aligned and within the upright folded migmatitic foliation suggest that upright (F_3) folding along a N-S axis occurred immediately following peak M_2 kyanite-bearing conditions. Therefore, the E-W–directed compressional deformation that produced these folds took place at lower pressures in the sillimanite stability field (M_3), for which the *P-T* conditions were constrained using garnet rim compositions affected by retrograde equilibration. These compositions (13% pyrope and 6% grossular) suggest *P-T* conditions of ~7 kbar and 710 °C (Fig. 18), signifying an almost isothermal decompression *P-T* path during exhumation, cooling at ~3 °C km^{-1}.

Figure 18 (*on following page*). Calculated pressure-temperature (*P-T*) pseudosections for sample TL67 from the Koronos Unit, using the observed bulk compositions, where compositional isopleths of grossular (Grs) and pyrope (Prp) for garnet are blue and red, respectively. (A) Calculated pseudosection for TL67 in the presence of pure water, predicting peak conditions suprasolidus. (B) Temperature vs. water activity plots at 9 and 10 kbar showing the predicted change in assemblages in response to water activity, where water activity of 0.5 relates to the occurrence of Ms + Ky + Kfs at reasonable temperatures from independent Ti-in-biotite thermometry. (C) *P-T* pseudosection of TL67 for a water activity of 0.5 showing key phase fields. (D) Compositional isopleths for garnet showing core compositions intersecting at ~6 kbar and 560 °C, whereas inner rim compositions representing peak conditions intersect at ~10 kbar and 680 °C. (E) Garnet mode isopleths showing garnet growth with both increasing pressure and temperature, but upon crossing the muscovite dehydration reaction, garnet mode isopleths are almost isothermal, indicating garnet growth by isobaric heating proposed for small posttectonic garnets, e.g., TLTN22. Mineral abbreviations follow Whitney and Evans (2010).

TL66: Sillimanite Migmatite (Core Unit): Peak (M_3) Sillimanite-Grade Conditions

TL66 was collected from the deepest parts of the dome across the K-feldspar isograd, and bulk compositions were calculated from the observed mineral proportions combining both leucosome and melanosome. Leucocratic networks within and radiating from the Naxos high-grade core combined with the partial preservation of garnet suggest that some melt was lost from the rock system during its *P-T* evolution (White and Powell, 2002). Therefore, this bulk composition is appropriate for modeling *P-T* conditions after the loss of that melt fraction (i.e., it is valid for assessment of peak/near-peak and suprasolidus retrograde metamorphism, but not the prograde subsolidus evolution prior to melt loss). Phase equilibria with excess H_2O were calculated for subsolidus and suprasolidus conditions, representing an external flux of water to produce maximum melting. The resulting pseudosections are presented in Figures 19D and 19F, revealing complex subsolidus topologies, whereas the suprasolidus phase relationships are simple, with large areas of *P-T* space without a change in variance. A closed system model, more realistic melting, was calculated by analyzing the water content at the hydrous solidus. It was determined that 7.6% H_2O was required to ensure all H_2O enters melt at the solidus, leaving water undersaturated at suprasolidus conditions. The calculated bulk compositions are shown in the Data Repository (see footnote 1), along with associated pseudosections.

At subsolidus conditions, both models predict low proportions of garnet, consistent with the sample, and a garnet core composition (14% pyrope, 9% grossular) plotting within the Grt–Ms–Bt–Ky–Ilm–Pl–Qtz–H_2O field at 6.0 kbar and 610 °C. This is within 0.3 kbar of the garnet-producing reaction, probably reflecting delayed garnet nucleation. The model predicts a prograde *P-T* path through the kyanite stability field, accounting for kyanite inclusions in muscovite. At suprasolidus conditions, the externally open system H_2O model predicts K-feldspar absence in the presence of high melt fractions, consistent with faserkiesel textures and diatexites. Garnet rim compositions (15% pyrope, 6% grossular) plot at 4.9 kbar and 705 °C with 33% melt. It is unlikely this rock experienced such extensive melting, and the presence of kyanite preserved as inclusions within muscovite suggests little fluid infiltration above the solidus.

For the closed system case, less melt is predicted (20%), and the garnet rim compositions plot at higher pressure and temperature (6.0 kbar, 720 °C), in the stability field of the Grt–Kfs–Bt–Sil–Pl–Ilm–Qtz–Liq assemblage beyond the muscovite dehydration melting reaction. This is consistent with the abundance of secondary muscovite produced through the back reaction by eliminating all K-feldspar shown in Equation 4. Assuming a molar 1:1 ratio between K-feldspar and muscovite, it was calculated that 18% by volume K-feldspar would be required to produce all secondary muscovite (24% by volume). However, only 11% K-feldspar is predicted to coincide with garnet rim compositions, suggesting secondary muscovite formed by a more complicated process. Release of fluids during crystallization through the solidus rehydrates the rock associated with the assemblage Grt–Bt–Ms–Pl–Qtz–Ilm and may account for more muscovite production through retrograde water-conserving reactions such as:

$$\text{biotite + sillimanite + quartz + plagioclase} \rightarrow \text{garnet + muscovite.} \quad (7)$$

In this case, 11% volume K-feldspar could be attained with just 14% volume muscovite in a simple 1:1 molar ratio. Production of secondary muscovite through this reaction would also account for less sillimanite and biotite observed than predicted (8% observed compared to 10% predicted) by production of secondary garnet and muscovite. However, due to diffusional equilibration at high temperature, it is unlikely that garnet rim compositions represent peak temperatures. Ti-in-biotite thermometry also predicted most biotite homogenized at temperatures of 650–700 °C, which is unlikely to represent peak temperatures. However, AvPT predicted garnet innermost rims with representative matrix minerals compositions of 7.5 ± 1.2 kbar and 742 ± 39 °C (Table 5), in agreement with predicted garnet modal proportions. Based on these lines of reasoning, we are confident these results represent peak M_3 sillimanite-grade conditions.

Melt Reintegration (Prograde Evolution)

To account for leucogranites that emanate from and throughout the Core Unit, it is likely that the Naxos migmatites have experienced some degree of melt loss. This occurs because once melt accumulation reaches a critical threshold, a portion may be lost, creating an open-system environment (Vanderhaege, 2004). This melt composition is dependent on the *P-T* conditions of formation (White and Powell, 2002), and melt extraction events may occur in an interrupted or continuous process (Sawyer, 1996). This open-system behavior, combined with the uncertainty concerning the proportion and composition of melt lost, makes recovering a bulk composition of the protolith very unlikely (Palin et al., 2013). However, White and Powell

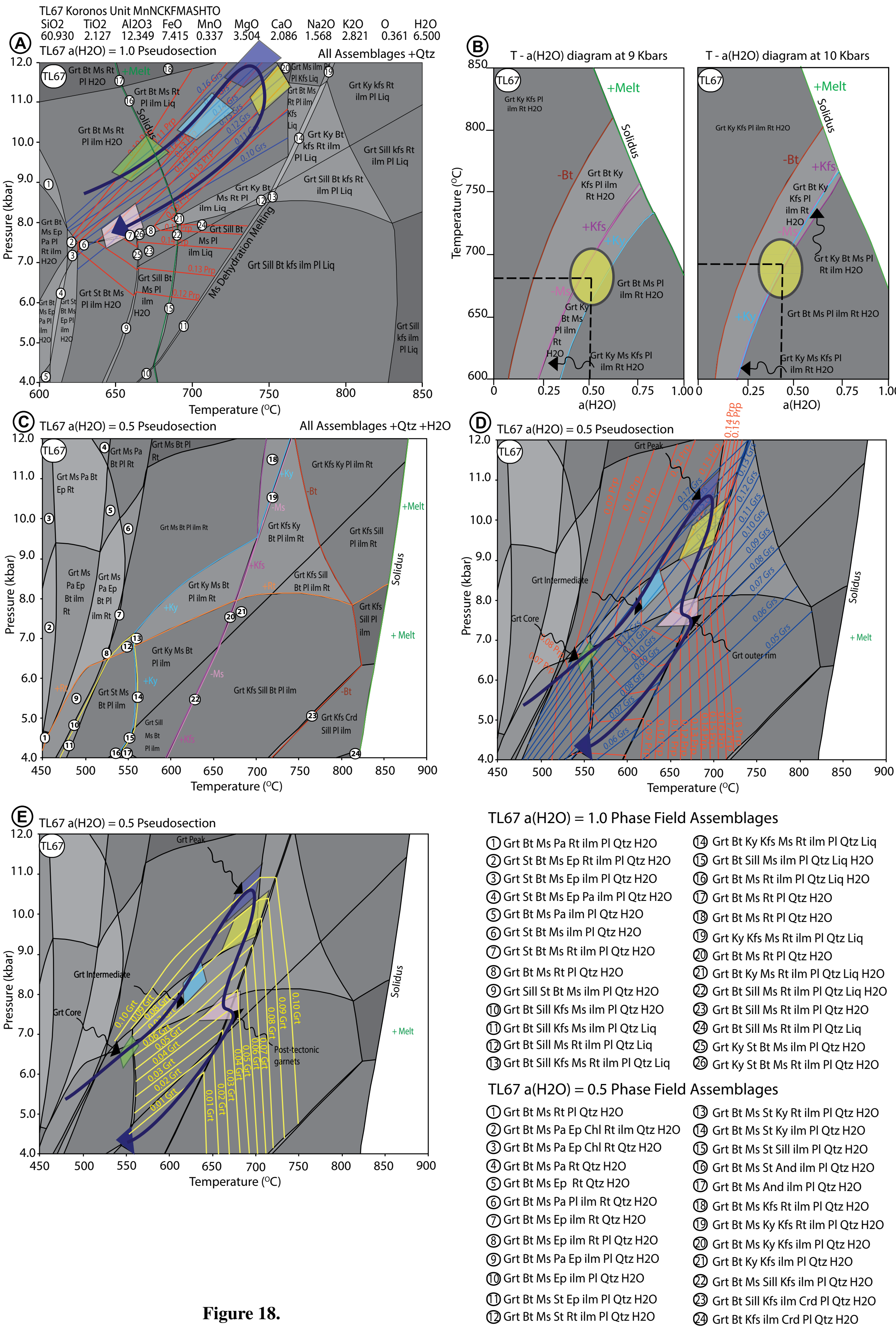
TL67 Koronos Unit MnNCKFMASHTO
SiO2 TiO2 Al2O3 FeO MnO MgO CaO Na2O K2O O H2O
60.930 2.127 12.349 7.415 0.337 3.504 2.086 1.568 2.821 0.361 6.500
A
TL67 a(H2O) = 1.0 Pseudosection
All Assemblages +Qtz
Pressure (kbar)
Temperature (°C)
B
T - a(H2O) diagram at 9 Kbars
T - a(H2O) diagram at 10 Kbars
Temperature (°C)
a(H2O)
+Melt
Solidus
C
TL67 a(H2O) = 0.5 Pseudosection
All Assemblages +Qtz +H2O
D
TL67 a(H2O) = 0.5 Pseudosection
Grt Peak
Grt Intermediate
Grt Core
Grt outer rim
E
TL67 a(H2O) = 0.5 Pseudosection
Post-tectonic garnets
TL67 a(H2O) = 1.0 Phase Field Assemblages
1 Grt Bt Ms Pa Rt ilm Pl Qtz H2O
2 Grt St Bt Ms Ep Rt ilm Pl Qtz H2O
3 Grt St Bt Ms Ep ilm Pl Qtz H2O
4 Grt St Bt Ms Ep Pa ilm Pl Qtz H2O
5 Grt Bt Ms Pa ilm Pl Qtz H2O
6 Grt St Bt Ms ilm Pl Qtz H2O
7 Grt St Bt Ms Rt ilm Pl Qtz H2O
8 Grt Bt Ms Rt Pl Qtz H2O
9 Grt Sill St Bt Ms ilm Pl Qtz H2O
10 Grt Bt Sill Kfs Ms ilm Pl Qtz H2O
11 Grt Bt Sill Kfs Ms ilm Pl Qtz Liq
12 Grt Bt Sill Ms Rt ilm Pl Qtz Liq
13 Grt Bt Sill Kfs Ms Rt ilm Pl Qtz Liq
14 Grt Bt Ky Kfs Ms Rt ilm Pl Qtz Liq
15 Grt Bt Sill Ms ilm Pl Qtz Liq H2O
16 Grt Bt Ms Rt ilm Pl Qtz Liq H2O
17 Grt Bt Ms Rt Pl Qtz H2O
18 Grt Bt Ms Rt Pl Qtz H2O
19 Grt Ky Kfs Ms Rt ilm Pl Qtz Liq
20 Grt Bt Ms Rt Pl Qtz H2O
21 Grt Bt Ky Ms Rt ilm Pl Qtz Liq H2O
22 Grt Bt Sill Ms Rt ilm Pl Qtz Liq H2O
23 Grt Bt Sill Ms Rt ilm Pl Qtz H2O
24 Grt Bt Sill Ms Rt ilm Pl Qtz Liq
25 Grt Ky St Bt Ms ilm Pl Qtz H2O
26 Grt Ky St Bt Ms Rt ilm Pl Qtz H2O
TL67 a(H2O) = 0.5 Phase Field Assemblages
1 Grt Bt Ms Rt Pl Qtz H2O
2 Grt Bt Ms Pa Ep Chl Rt ilm Qtz H2O
3 Grt Bt Ms Pa Ep Chl Rt Qtz H2O
4 Grt Bt Ms Pa Rt Qtz H2O
5 Grt Bt Ms Ep Rt Qtz H2O
6 Grt Bt Ms Pa Pl ilm Rt Qtz H2O
7 Grt Bt Ms Ep ilm Rt Qtz H2O
8 Grt Bt Ms Ep ilm Rt Pl Qtz H2O
9 Grt Bt Ms Pa Ep ilm Pl Qtz H2O
10 Grt Bt Ms Ep ilm Pl Qtz H2O
11 Grt Bt Ms St Ep ilm Pl Qtz H2O
12 Grt Bt Ms St Rt ilm Pl Qtz H2O
13 Grt Bt Ms St Ky Rt ilm Pl Qtz H2O
14 Grt Bt Ms St Ky ilm Pl Qtz H2O
15 Grt Bt Ms St Sill ilm Pl Qtz H2O
16 Grt Bt Ms St And ilm Pl Qtz H2O
17 Grt Bt Ms And ilm Pl Qtz H2O
18 Grt Bt Ms Kfs Rt ilm Pl Qtz H2O
19 Grt Bt Ms Ky Kfs Rt ilm Pl Qtz H2O
20 Grt Bt Ms Ky Kfs ilm Pl Qtz H2O
21 Grt Bt Ky Kfs ilm Pl Qtz H2O
22 Grt Bt Ms Sill Kfs ilm Pl Qtz H2O
23 Grt Bt Sill Kfs ilm Crd Pl Qtz H2O
24 Grt Bt Kfs ilm Crd Pl Qtz H2O

Figure 18.

(2002) showed that various melt-loss scenarios do not change the major subsolidus and suprasolidus topologies or compositions of peritectic phases. It is therefore possible to calculate an approximate bulk composition suitable for prograde modeling. To reduce uncertainty, the melt loss was modeled as a single extraction event, representing a simple end-member case. A melt-reintegrated bulk composition was therefore calculated by the addition of a proportion of melt to the observed bulk composition to displace the solidus down-temperature to H_2O-saturated conditions, maximizing the amount of mica present prior to melting following the method of White et al. (2004). The composition of reintegrated melt was calculated at 7.75 kbar and 680 °C by using the solidus of the original bulk composition in the presence of kyanite. Although higher pressure than final melt crystallization, this *P-T* value was chosen because it accounts for the presence of kyanite-bearing migmatites and inclusions in secondary muscovite at higher structural levels (TL15), allowing for a clockwise *P-T* evolution. It was determined that 10% melt should be added to make the solidus water-saturated.

Contours for modal proportion of silicate melt are presented in the Data Repository material (see footnote 1), and they show that melt production across the wet solidus in garnet-bearing assemblages is negligible (~1%). It is not until fluid-absent muscovite dehydration occurs that melt generation reaches significant volumes, increasing from 4% to 12% over a very small temperature interval. Contours for calculated modal proportion of garnet allow interpretation of probable conditions of garnet core growth with respect to the melting history. Although garnet cores lack prograde compositional zoning, making the early stages of the *P-T* evolution poorly constrained, certain inferences can be made. The presence of muscovite inclusions within garnet suggests garnet nucleated prior to the muscovite dehydration melting reaction in a muscovite-present field. The presence of kyanite relicts within secondary muscovite suggests that garnet grew when kyanite was stable. A possible interpretation involves a *P-T* evolution along an initial continental geotherm of 25–30 °C km^{-1}. This allows initial garnet growth to occur at ~600 °C and 6 kbar in an assemblage containing Bt–Ms–Pl–Ilm–Qtz–H_2O. Contours for modal proportion of garnet reveal that growth in muscovite-bearing assemblages was minor, and significant growth of garnet was delayed until K-feldspar was produced as a result of muscovite dehydration along the effective solidus where the proportion of garnet increases significantly with increasing temperature (see Data Repository material [footnote 1]). However, due to the presence of only ~1.5% garnet, we conclude temperatures did not increase significantly upon passing this melting reaction, and thus it is likely that crossing the effective solidus was largely related to decompression at peak metamorphic conditions.

Figure 19 (*on following page*). Calculated pressure-temperature (*P-T*) pseudosections for samples TL15 and TL66 from the Core Unit, with garnet compositional isopleths for pyrope (Prp) in blue and for grossular (Grs) in pink and modal proportion of garnet plotted in yellow. (A) TL15 pseudosection using the observed assemblage and pure water activity showing key phase fields. (B) Isopleths for garnet compositions show a clockwise *P-T* loop and suggest that the *P-T* path never crossed the muscovite dehydration melting reaction. (C) Isopleths for garnet mode and proportions of melt, note the rapid increase in partial melt upon crossing the muscovite dehydration melting reaction. (D) TL66 pseudosection using the observed assemblage and pure water activity showing phase relations. (E) TL66 isopleths for garnet compositions only showing the retrograde part of the *P-T* path through the sillimanite stability field due to garnet homogenization and resorption. (F) Garnet mode and melt fraction isopleths for TL66; note isothermal decompression through the muscovite dehydration melting reaction is expected to decrease garnet mode and cause resorption. Mineral abbreviations follow Whitney and Evans (2010).

Postpeak Suprasolidus Evolution

Crystallization of the final melt fraction upon crossing the solidus is thought to mark the final retrograde textural evolution of an anatectic rock, if no further episodes of deformation or fluid influx occur (e.g., White and Powell, 2002; Indares et al., 2008; Palin et al., 2013). Nonetheless, postpeak compositional changes may still occur via intracrystalline diffusion, as seen in garnet porphyroblast outer rims in contact with matrix biotite, which have grossular and pyrope contents of ~6% and 15%, respectively. These are lower than the concentrations recorded in core regions, consistent with equilibration at lower temperature and pressure (Spear, 1993). Isopleths for the calculated modal proportions of garnet and melt are presented in Figure 19, and they show that both phases are produced at higher temperature due to the breakdown of muscovite. However, retrograde decompression from our calculated peak *P-T* conditions to the solidus would have involved a reduction in the modal proportion of garnet to form biotite and sillimanite, consistent with observed textures. Taking these factors into consideration reveals that the Naxos migmatites remained at suprasolidus conditions during deep crustal exhumation and crystallized through the water-saturated solidus at ~4.9 kbar and 690 °C.

Summary of *P-T* Results

The *P-T* data clearly demonstrate that two distinct and contrasting clockwise *P-T* loops are recorded within the Naxos core complex (Figs. 16–19). At high structural levels, the Zas Unit records M_1 conditions of ~14.5 kbar and 470 °C followed only by retrograde greenschist-facies conditions at <450 °C. In contrast, at deeper structural levels (Koronos and Core Units), (M_1) high-pressure–low-temperature conditions are not recorded, and instead the rocks experienced a clockwise *P-T* path involving (M_2) prograde burial and heating along a Barrovian metamorphic thermal gradient of ~25 °C km^{-1} to peak (M_2) *P-T* conditions of ~10 kbar and 600–730 °C (TL15, TLN22, TL67). At the deepest levels (Core Unit), the rocks crossed the water-saturated solidus and then experienced hydrous (M_2) kyanite-grade melting (Eq. 6; TL15). They then recorded near-isothermal decompression to (M_3) sillimanite-grade conditions of 5–6 kbar and 700–730 °C (TL66, TLN34, TLN20A). During this process, the hottest and deepest rocks crossed the muscovite dehydration melting reaction to produce larger melt volumes and peritectic K-feldspar. Textural evidence suggests that most melt remained in communication with the rock, and therefore crystallization through the solidus at ~5 kbar and 690 °C released fluids, causing metasomatism and growth of secondary muscovite crosscutting the earlier extensional fabric (S_3). Juxtaposition of the hot migmatites against the overlying Koronos Unit caused a thermal (M_3) sillimanite-grade overprint and posttectonic garnet growth that truncated the S_3 top-to-the-shear fabrics and earlier (M_2) kyanite-grade assemblage (e.g., TLN13, TLN21, TLN22). The rocks then experienced a kink in the *P-T* path associated with cooling at <5 kbar pressure, causing resorption of garnet and cooling along a thermal gradient of ~40 °C km^{-1}.

PALINSPASTIC RESTORATION OF THE NAXOS CORE COMPLEX

Although balanced and restored cross sections cannot be applied to intensely deformed rocks under ductile conditions, we attempted

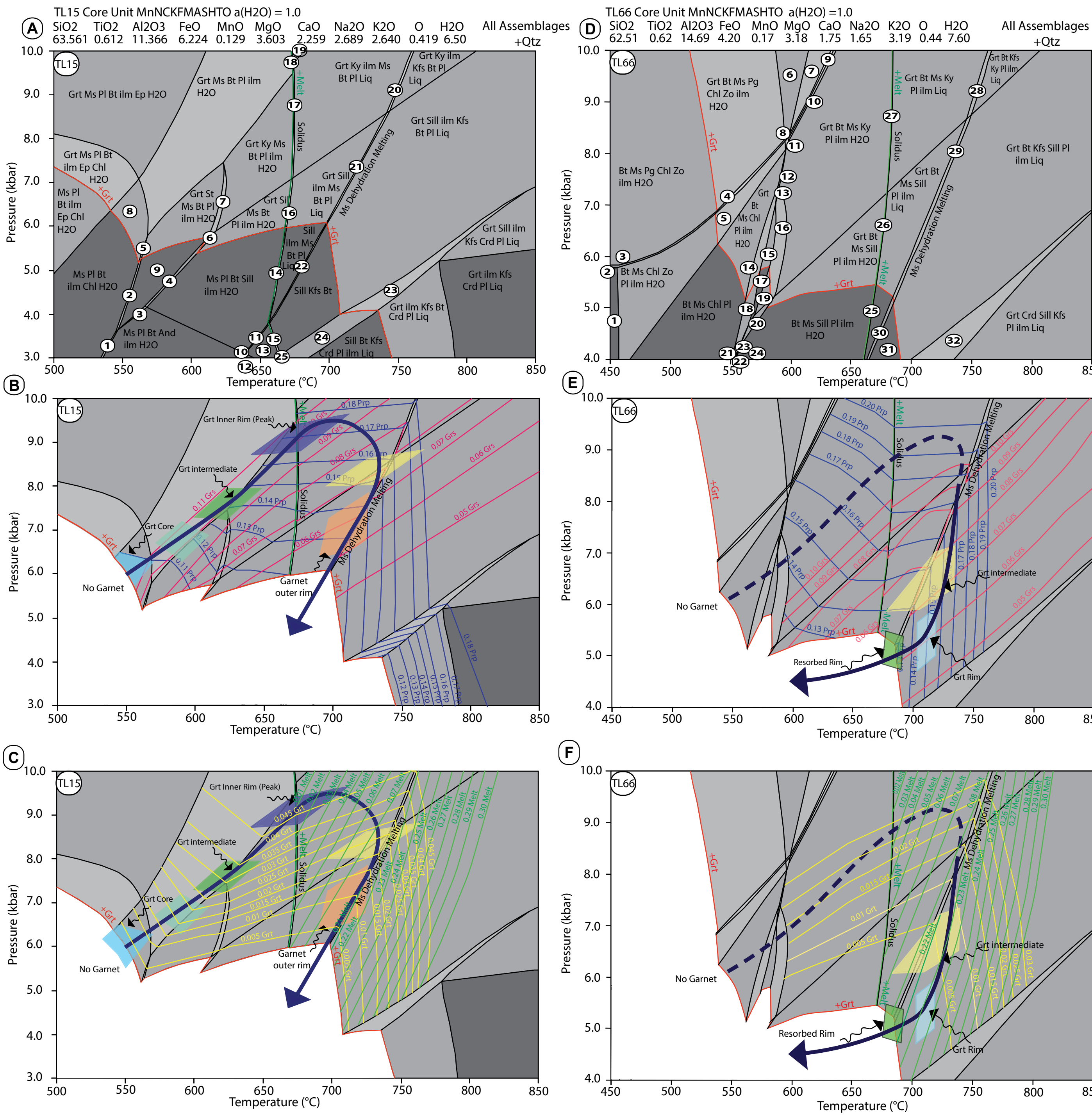

TL15 Phase Field Assemblages

1. Ms Bt Pl ilm Chl And Qtz H2O
2. Ms Bt Pl ilm Chl St Qtz H2O
3. Ms Bt Pl ilm St And Qtz H2O
4. Ms Bt Pl ilm St Sill Qtz H2O
5. Grt Ms Bt Pl ilm Chl St Qtz H2O
6. Grt Ms Bt Pl ilm St Sill Qtz H2O
7. Grt Ms Bt Pl ilm St Ky Qtz H2O
8. Grt Ms Bt Pl ilm Chl Qtz H2O
9. Ms Bt Pl ilm St Qtz H2O
10. Ms Bt Kfs Pl ilm Qtz And H2O
11. Ms Bt Kfs Pl ilm Qtz Sill H2O
12. Bt Kfs Pl ilm Qtz And H2O
13. Bt Kfs Pl ilm Qtz Sill H2O
14. Ms Bt Pl ilm Sill Qtz Liq H2O
15. Bt Kfs Pl ilm Qtz Sill Liq H2O
16. Grt Ms Bt Pl ilm Sill Qtz Liq H2O
17. Grt Ms Bt Pl ilm Ky Qtz Liq H2O
18. Grt Ms Bt Pl ilm Qtz Liq H2O
19. Grt Ms Bt Pl ilm Qtz Liq
20. Grt Ky Ms Bt Kfs Pl ilm Qtz Liq
21. Grt Sill Ms Bt Kfs Pl ilm Qtz Liq
22. Sill Ms Bt Kfs Pl ilm Qtz Liq
23. Grt Sill Bt Kfs Crd Pl ilm Qtz Liq
24. Sill Bt Kfs Crd Pl ilm Qtz Liq
25. Sill Bt Kfs Crd Pl ilm Qtz Liq H2O

TL66 Phase Field Assemblages

1. Ms Chl Zo Pl ilm Qtz H2O
2. Ms Chl Pa Zo Pl ilm Qtz H2O
3. Bt Ms Chl Pg Zo Pl ilm Qtz H2O
4. Grt Bt Ms Chl Pg Zo Pl ilm Qtz H2O
5. Grt Bt Ms Chl Zo Pl ilm Qtz H2O
6. Grt Bt Ms Zo Pg ilm Qtz H2O
7. Grt Bt Ms Zo Pg Pl ilm Qtz H2O
8. Grt Bt Ms Zo Pg Pl ilm Qtz H2O
9. Grt Bt Ms Ky Zo Pg Pl ilm Qtz H2O
10. Grt Bt Ms Ky Pg Pl ilm Qtz H2O
11. Grt Bt Ms Ky Zo Pl ilm Qtz H2O
12. Grt Bt Ms Ky Chl Pl ilm Qtz H2O
13. Grt Bt Ms Ky Chl St Pl ilm Qtz H2O
14. Grt Bt Ms Chl St Pl ilm Qtz H2O
15. Grt Bt Ms St Pl ilm Qtz H2O
16. Grt Bt Ms Ky St ilm Pl Qtz H2O
17. Bt Ms St Pl ilm Qtz H2O
18. Bt Ms St Chl Pl ilm Qtz H2O
19. Bt Ms St Ky ilm Pl Qtz H2O
20. Bt Ms Sill St Pl ilm Qtz H2O
21. Bt Ms Chl And Pl ilm Qtz H2O
22. Bt Ms Chl St And ilm Pl Qtz H2O
23. Bt Ms St Chl Sill ilm Pl Qtz H2O
24. Bt Ms And Pl ilm Qtz H2O
25. Bt Ms Sill ilm Pl Qtz Liq H2O
26. Grt Bt Ms Sill ilm Pl Qtz Liq H2O
27. Grt Bt Ms Ky ilm Pl Qtz Liq H2O
28. Grt Bt Ms Ky Kfs Pl ilm Qtz Liq
29. Grt Bt Ms Sill Kfs Pl ilm Qtz Liq
30. Bt Ms Kfs Sill Pl ilm Qtz Liq
31. Bt Kfs Sill Pl ilm Qtz Liq
32. Grt Bt Crd Sill Kfs Pl ilm Qtz Liq

Figure 19.

a palinspastic restoration of the metasedimentary and basement units to place minimum constraints on crustal shortening. A simple restoration of the Naxos MCC was performed to estimate minimum amounts of shortening during the leadup to peak M_3 conditions and postmetamorphic doming, by considering all structural, petrographic, pressure-temperature-deformation (*P-T-D*), and U-Th-Pb data presented herein. U-Th-Pb results will be presented in a future study. A simple two-dimensional area- and line-balance restoration along section A–A′ provided insight into the way in which the MCC formed, and how nappes of differing lithologies attained different *P-T* conditions at different times and were juxtaposed against each other. The restoration assumes that, in general, deformation propagated down-structural section with time, in agreement with structural, petrographic, and *P-T-D* data. The restoration process involved the following steps:

(1) The late-stage E-W doming and normal faults were restored prior to pre-Miocene extension and granodiorite intrusion using the Galanado normal fault as a pinning point (pinning point 5; Fig. 20, stage 1).

(2) Three units (Zas Unit, Koronos Unit, and Core Unit) were identified within the metamorphic footwall and treated separately; each unit is separated by a major extensional shear zone that cannot be restored due to lack of suitable pinning points (see text for more discussion).

(3) Zas Unit (Cycladic Blueschists) was assumed to behave in a brittle-ductile manner, dominantly by thrusting, and was restored first (Fig. 20, stage 2).

(4) Koronos Unit thrusts were restored to align the F_1 and F_2 folds. These folds were then restored using area and line-length balancing and assuming there are only three bands of marble structurally repeated. Basement-cover repetitions were assumed to represent thick-skinned thrusts and were restored to their original geometry.

(5) The Core Unit deformation was restored in two steps. The KSZ was restored by line-length balancing of the imbricate stack that utilized basement material as a relict thick-skinned thrust. Ductile deformation and isoclinal folding were restored using line-length and area balancing as above (Fig. 20, stage 2). This represents a minimum amount of shortening, because the thick-skinned thrusts structurally repeating the basement over shelf are laterally discontinuous, overprinted, and reworked by upright folding and ductile flow.

(6) Finally, a restoration of the continental margin was attempted in stage 3, based on structural mapping in this study. This suggests that Naxos records a thrusted and thickened continental margin sequence in a similar style to the Helvetic Nappes in the Alps and Greater Himalayan Series (Fig. 20, stage 3). The results show that the restored continental margin was intruded by numerous basaltic and doleritic sills, with intercalated tuffaceous, siliciclastic, and carbonate material.

An ~13-km-wide section today restores to a minimum of 60 km. Approximately 400% ENE-WSW shortening across the Naxos MCC is required to explain the folding and thickening during its prograde evolution. Although accurate section balancing is precluded in terrains with ductile deformation such as the Naxos MCC, an absolute minimum shortening of 47 km cannot be rectified. Although several assumptions were applied that may be oversimplistic and violated in ductile environments, this exercise illustrates that the folding of high-grade rocks forming the core complex could not have formed by purely extensional mechanisms. This magnitude of shortening within a continental margin sequence is commonly seen across many recent mountain ranges that experienced shortening and underthrusting of rocks to kyanite-grade conditions over time scales of tens of millions of years, such as the Himalaya (Corfield and Searle, 2000) and accretionary wedges such as those in Oman (Searle et al., 2004). Therefore, we believe that most of the structures (F_1 and F_2 folding) and prograde and peak (M_2) Barrovian conditions of the Naxos MCC occurred under a compressional tectonic regime, and not under crustal extension. Upright (F_3) folding within migmatites occurred at M_3 sillimanite-grade conditions and invokes a horizontal contractional stress regime. Whatever the cause for this constriction, it highlights a significant space problem requiring lateral displacement of material from the sides, and therefore it must have formed when the maximum principal stresses (σ_1) were orientated in a horizontal plane. Deformation as a result of this contraction must have become localized within the rheologically weaker migmatites upon experiencing muscovite dehydration melting, causing them to intensely fold, thicken, and dome the overlying units.

A significant component of E-W shortening is necessary to form the structures on Naxos, and it is suggested that some E-W shortening is occurring throughout the Aegean today (McClusky et al., 2000), accommodated on active conjugate ENE-WSW– and WNW-ESE–trending strike-slip faults like those that crosscut Naxos (see Fig. 2). This could be possibly related to a 20° counterclockwise rotation of Naxos about a vertical axis since the mid-Miocene (Kissel and Laj, 1988; Avigad et al., 1998; Malandri et al., 2016), and it could explain the late-stage gentle folding of the NPDS, the sedimentary units in the upper Cycladic Nappe, and the metamorphic sequence. Although the origin of Miocene E-W shortening remains unclear, there are several possible mechanisms that are discussed below.

Due to extreme attenuation, missing metamorphic stratigraphy, and many unknowns, such as the original dip of the NPDS, restoration of the extensional features and therefore the full amount of extension cannot be accurately determined. However, NNE-SSW crustal extension is the last phase of deformation, and it is pervasive, overprinting and truncating all shortening structures. It is frozen in the metamorphic stratigraphy and the migmatite dome. Assuming the doming occurred at ~5 kbar (17.5 km depth), and the NPDS maintained its original dip of ~10° to the north and was responsible for the entire exhumation of Naxos, the throw on this single fault would be >100 km. This fault must have been active in its present-day shallow geometry and could not have been rotated from steeper to shallower angles, as the migmatite dome and metamorphic footwall cannot have been rotated by over 40°. It seems likely, however, that the NPDS was not responsible for the entire exhumation on Naxos, but rather represents the brittle-ductile transition, mechanically uncoupling the upper- and midcrust, and it was exhumed in its present-day geometry by uplift on several younger crosscutting brittle normal faults. The simplistic relationships and restoration for the geometry of the Naxos-Paros detachment and earlier peak M_2 and M_1 geometries based on field relations and *P-T-D* data are presented in Figure 21.

DISCUSSION

Integration of Structural, Petrographic, and *P-T-D* Data

Crustal Thickening and Prograde and Peak Metamorphism

The field, petrological, and *P-T-D* data from this study imply a complicated tectonic evolution that cannot be explained by extension alone, with juxtaposition of several nappes that experienced differing metamorphic histories, as summarized by Figure 22. Previous models of Naxos, whereby all rocks experienced M_1 high-pressure conditions followed by isobaric heating and Barrovian metamorphism during crustal extension (e.g., Buick and Holland, 1989; Buick, 1991a, 1991b; Urai et al., 1990; Avigad, 1998; Vanderhaeghe, 2004; Kruckenberg et al., 2010), cannot explain the clockwise Barrovian *P-T-D*-time (*t*) paths, which involve prograde increasing pressure and temperature in the Koronos and Core Units.

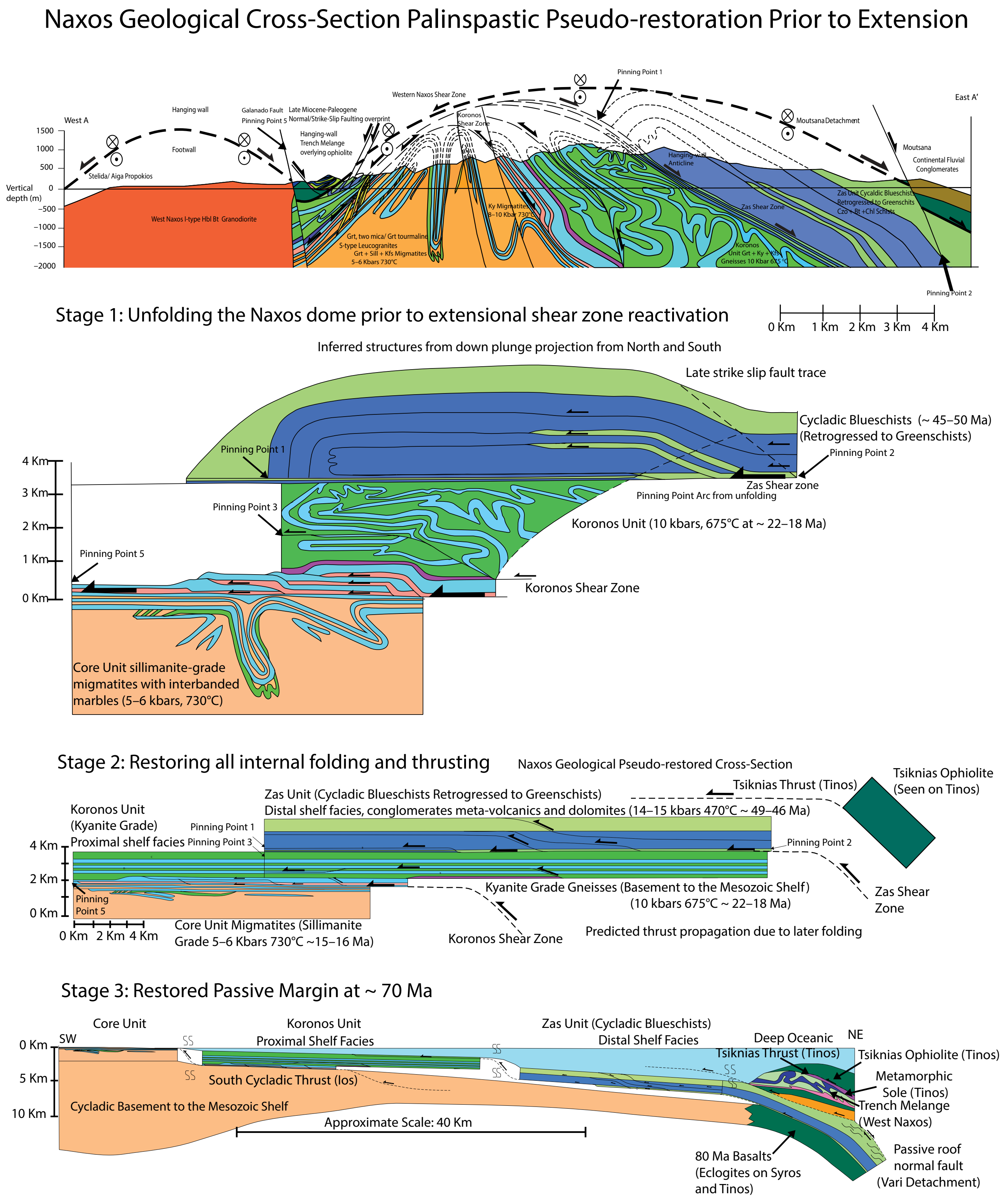

Figure 20. Palinspastic pseudorestoration of the Naxos metamorphic core complex, using the same color scheme as the maps and cross sections along line of section A–A′. Deformation was restored to that prior to late doming and I-type intrusion at 12.2 Ma, and then each unit was restored individually with deformation propagating down structural section with time, finally to the undeformed restored continental margin at ca. 70 Ma. See text for more discussion and details on each stage of the restoration. Mineral abbreviations follow Whitney and Evans (2010).

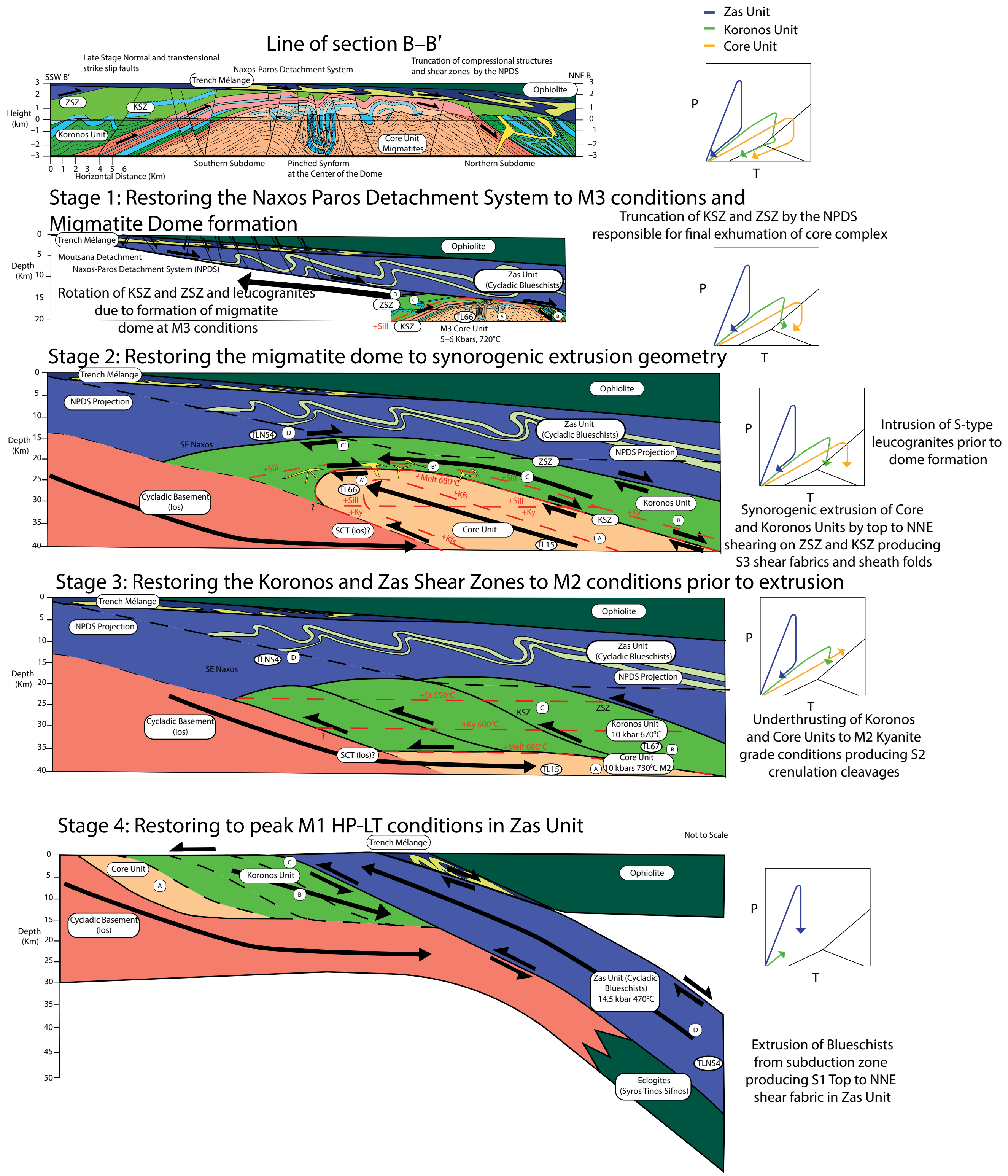

Figure 21. Schematic restoration of the Naxos metamorphic core complex along line of section B–B′, highlighting that the Naxos-Paros detachment system (NPDS) must truncate and postdate movement on the Zas shear zone (ZSZ) and Koronos shear zone (KSZ). Schematic predicted pressure-temperature-time (*P-T-t*) paths for each unit are displayed on the right. Stage 1—Restoration prior to extension, placing the core complex at ~18–20 km depth during migmatite formation. Stage 2—Restoration of the migmatites prior to dome formation. Stage 3—Restoration of the core complex prior to extrusion at peak M_2 kyanite-grade conditions representing ~35 km depth. Stage 4—Restoration prior to prograde burial of the Koronos and Core Units during peak M_1 conditions in the Zas Unit. See text for more discussion. Mineral abbreviations follow Whitney and Evans (2010). HP-LT—high-pressure–low-temperature; SCT—South Cycladic Thrust.

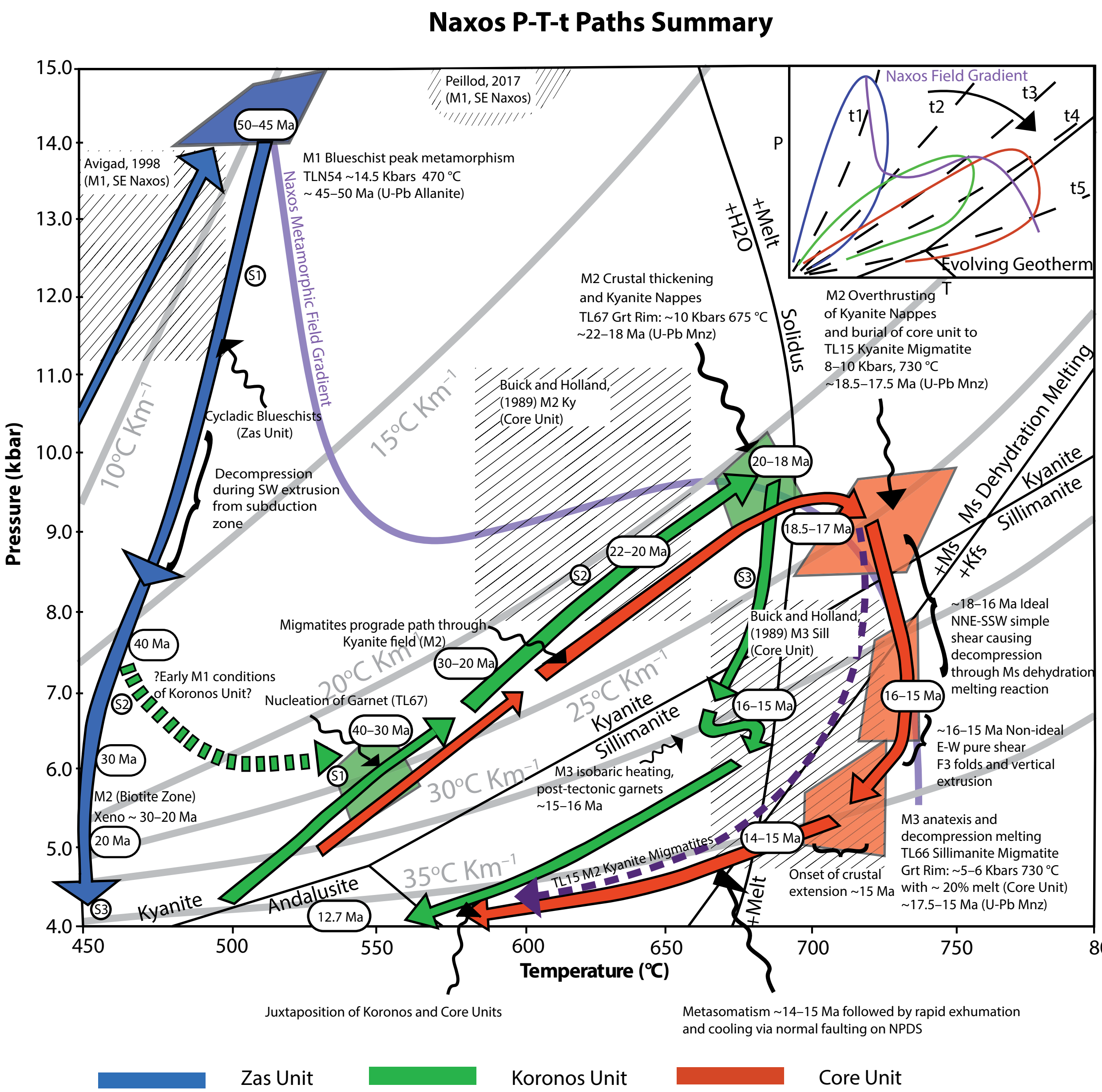

Figure 22. Summary pressure-temperature-time-deformation (*P-T-t-D*) paths for all units from the Naxos metamorphic core complex based on the results of this study. Shaded black hashed boxes represent *P-T* conditions estimated previously by Buick and Holland (1989), Avigad (1998), and Peillod et al. (2017; shown as Peillod 2017 in figure). Colored polygons represent estimated peak metamorphic conditions presented in this study, with labeled colored arrows that represent suggested *P-T* paths discussed in the text. U-Pb data will be presented in a future study. NPDS—Naxos-Paros detachment system. Mineral abbreviations follow Whitney and Evans (2010).

The rocks of southeast Naxos (Zas Unit or Cycladic Blueschists) underwent a completely different metamorphic evolution than the underlying higher-grade units. Contrary to previous suggestions that the whole island experienced (M_1) high-pressure conditions (Avigad, 1998; Martin et al., 2006), we find no evidence in the petrography or geochronology to suggest that either the Koronos or the Core Units experienced this event. Although it is poorly understood how meta-peridotites occur as enclaves within meta-gabbro (amphibolites) and are associated with both the Koronos and Zas shear zones (Katzir et al., 1999, 2002), several mechanisms have been proposed: (1) Katzir et al. (1999) suggested that the ultramafics were emplaced during Eocene subduction of the continental margin. (2) They could have also been emplaced by thrusting of lithospheric mantle and meta-gabbros into the Naxos shelf carbonate sequence. (3) They could have been doleritic or gabbroic sills that intruded the continental margin prior to deformation, and the ultramafic component represents cumulates that formed during fractional crystallization. (4) They could be slivers of serpentinite that were incorporated from a structurally higher ophiolitic thrust sheet, although this requires over several kilometers of structural movement. To explain the thermometry data of Katzir et al. (2002), minor compositional layering within the host amphibolites, and the absence of high-pressure relicts (see 17TL75 in the Data Repository material [footnote 1]), we suggest they represent doleritic-gabbroic sills that intruded the continental margin prior to deformation. This is because the host garnet-bearing meta-gabbros show no evidence of a high-pressure history, and this is the most likely rock composition to preserve evidence for blueschist- or eclogite-facies metamorphism (Heinrich, 1982). Furthermore, the mantle wedge in a subduction setting is cold, and this disagrees with two-pyroxene thermometry temperatures exceeding 1000 °C (Katzir et al., 2002); it is more likely to be associated with hot intrusion. If the Koronos and Core Units did experience M_1 conditions, they must have been reincorporated into another prograde burial Barrovian tectono-metamorphic cycle that obliterated all trace of this previous metamorphic event.

Eocene zircon ages of ca. 40 Ma have been reported from amphibolites from northern Naxos and within the Koronos Unit (Martin et al., 2006; Bolhar et al., 2017), and these could represent two possibilities: (1) The ages represent zircon growth during (M_1) high-pressure–low-temperature conditions but not in the presence of garnet (Martin et al., 2006), and the unit was extruded to the midcrust before being reburied and incorporated as part of a separate metamorphic cycle. In this scenario, prograde and peak M_2 conditions would occur ca. 25 Ma after experiencing high-pressure conditions, like the Lepontine metamorphism in the central Alps (e.g., Wiederkehr et al., 2008). (2) Alternatively, the ages do not represent M_1 conditions, which occurred on Naxos between 49 and 46 Ma and regionally at 54–45 Ma (Tomaschek et al., 2003; Lagos et al., 2007; Dragovic et al., 2012). In the absence of high-pressure relicts, the ca. 40 Ma zircon ages could be interpreted to represent the earliest M_2 Barrovian-type age due to overthrusting of the blueschists (Zas Unit). The latter of these two suggestions is our preferred choice and agrees with the petrological record on Naxos and new U-Pb data that will be presented in a future study.

To account for contrasting *P-T-D* paths recorded at different structural levels on Naxos, our model features subduction of the distal continental margin (Zas Unit) down a NE-dipping subduction zone to (M_1) high-pressure–low-temperature conditions that reached blueschist-facies conditions on Naxos, but also eclogite-facies conditions as seen on the islands of Syros, Tinos, and Sifnos. This was followed by SW expulsion of high-pressure rocks under a passive-roof normal fault (Vari detachment on Syros; Roche et al., 2016; Laurent et al., 2016) at the top of the subduction channel and a thrust at the base due to the positive buoyancy of continental margin material (England and Holland, 1979). Although this thrust is not convincingly exposed on Naxos due to extensional reworking, there is a strong record of thrust-related fabrics (S_{2a} and S_{2b}), and it is possible that the South Cycladic thrust on Ios (Huet et al., 2009; Mizera and Behrmann, 2015) could be this structure or a related structure. This would produce S_1 top-to-the-NE shear fabrics in the Zas Unit and the rest of the Cycladic Blueschists and would adequately explain S_2 crenulation cleavages and thrust fabrics under M_2 greenschist-facies conditions. Overthrusting of this high-pressure unit onto the more-proximal Cycladic continental margin, along with continued crustal shortening, would have led to the generation of a nappe pile (Dixon and Robertson, 1984). The proximal sedimentary cover of the continental margin (Koronos Unit) would have subsequently experienced burial, polyphase folding, and thick-skinned thrusting, as exemplified by structural repetition of basement material overlying metasedimentary protoliths during M_2 kyanite-grade conditions. This would have led to crustal thickening and (M_2) regional metamorphism during the Oligocene to Miocene (40–15 Ma). A crustal shortening mechanism would explain isoclinal F_1 folding during prograde (M_2) Barrovian metamorphism and development of the (S_{2a}) crenulation cleavages (S_{2b}) and top-to-the-SW thrust fabrics under amphibolite-facies conditions, preserved in domains unaffected by late crosscutting S_3 extensional fabrics. Burial of the continental margin to (M_2) kyanite-grade pressures of ~10 kbar (~35 km depth) was associated with the development of these shortening structures. Growth of garnet porphyroblasts occurred syn- to posttectonically with localized (S_{2b}) thrust fabrics along cleavage domains at the base of the Koronos Unit, indicating a synchronicity between peak (M_2) kyanite-grade conditions and thick-skinned thrusting.

Contrasting peak *P-T* conditions between the Koronos and Core Units indicate these packages equilibrated along an evolving geotherm at slightly different times (U-Pb data will be provided in a future study). The most likely explanation in accordance with field evidence is that thick-skinned thrusting was responsible for burying the Core Unit under the Koronos Unit. Repetition of basement rocks interleaved with metasedimentary schists and marbles along the base of the Koronos Unit and within the Core Unit is consistent with this idea. Further evidence for a southwestward-verging thrust also occurs on the island of Ios as the South Cycladic thrust, which places a thin package of amphibolite-grade metasedimentary cover over Cycladic basement (Huet et al., 2009; Mizera and Behrmann, 2015).

Following thick-skinned thrusting, conductive relaxation of the footwall geotherm would have heated and driven partial melting over a time span of several million years (England 1978; England and Thompson, 1984). Footwall rocks first underwent prograde hydrous melting in the kyanite field, producing kyanite- and garnet-bearing microstructural domains and leucosomes (Eq. 6). Upon experiencing melt weakening, the rocks then record decompression through the muscovite dehydration melting reaction to sillimanite-grade conditions. This decompression was associated with non-coaxial (S_3) top-to-the-NNE shearing, flattening, and the development of F_2 sheath folds on the Koronos and Zas shear zones. This reaction is the first major melt-producing reaction and would allow deformation to become localized along weakened zones of melt segregation and facilitate the development of upright folding. Kyanite-grade fabrics are folded with this foliation, placing tight constraints on the timing of upright (F_3) folding after (M_2) kyanite-grade conditions and following decompression to (M_3) sillimanite-grade conditions.

Partial Melting, Decompression, and Formation of the Migmatite Dome

Several models for isothermal decompression and migmatite dome formation have been suggested, but many fail to explain all structural, petrological, and *P-T-D* constraints. In a subsequent study, it will be shown that decompression of migmatites from ~10 to 5 kbar occurred in less than 2.5 m.y., a time scale much shorter than previously thought. From the structural and petrological features described in this paper, a relative chronology and framework for the sequence of deformation events leading to doming can be firmly established, and therefore the various dome forming mechanisms can be assessed.

Crosscutting relationships on the KSZ bounding the migmatites demonstrate that (S_3) top-to-the-NNE shearing predated doming and leucogranite intrusion. This is because the shear zones are folded around the dome with consistent top-to-the-NNE kinematics on all margins. This normal-sense shearing must have been associated with SW-directed exhumation of the footwall Core Unit relative to the overlying Koronos Unit. S-type leucogranite dikes and sills clearly postdate shearing, because they crosscut the (S_3) mylonite fabrics on the KSZ (refer to Figs. 7–8; see also Data Repository material [footnote 1]), and they show emanating geometries from the migmatite core (see Figs. 6O and 8H). The crosscutting dikes dip at ~45° toward the center of the dome and intrude perpendicular to the S_3 foliation, particularly on the eastern margin. Because these dikes and the shearing foliation are tilted around the dome, we infer that both the dikes and shear zones have experienced rotations of ~45° about a NNE-SSW horizontal axis from their original subhorizontal orientation. The leucogranites dikes probably intruded vertically when the KSZ and migmatites where subhorizontal and were passively rotated as the dome formed. Because leucogranites are the product of melt extraction, and this only occurs upon reaching the critical melt threshold (7%–10%; Rosenberg and Handy, 2005), this volume of melting only occurred upon decompression through the muscovite dehydration melting reaction (Eq. 4), at lower-pressure (M_3) sillimanite-grade conditions, also coeval with the timing of upright folding. Upright F_3 folds in the CHSZ have three fold axis populations that intersect around a vertical point, representing a type-2 Ramsey fold interference pattern. Vertical boudinage of folds and leucogranite dikes (see Figs. 8–10) suggests overall horizontal constriction while also at M_3 sillimanite-grade conditions. The intense upright E-W–trending and N-S–trending isoclinal folds in the center of the dome require that the maximum principal stresses σ_1 and σ_2 must have been almost equal and orientated E-W and N-S in the horizontal planes, whereas the minimum principal stress, σ_3, must have been orientated vertically. This horizontal contraction scenario can be easily explained by overall shortening of the crust, and although diapirism would predict similar features (Ramberg, 1980), the low overall melt fractions in migmatites (see Fig. 19) are inconsistent with diapirism being the dominant doming process. Similar features have been documented in Archean granite-greenstone terranes, such as the Pilbara North Pole Dome in Australia (e.g., Nijman et al., 2017). Diapirism or crustal turnover has been proposed as a mechanism to explain these tonalite-trondhjemite-granodiorite (TTG)–cored domes (e.g., Collins et al., 1998), which are associated with larger melt fractions than Naxos migmatites. The pattern of doming and basins with other observed shortening phenomena indicates the importance of regional compression during the formation of these domes, which may have caused a first Raleigh instability, leading to an egg-box pattern of sinking greenstones around the TTG domes (Nijman et al., 2017). N-S horizontal boudinage, and a range of brittle deformation features overprinting these folds, suggests the principal stress axes rotated to a NNE-SSW–orientated σ_3 and E-W–oriented σ_1 direction shortly after these folds formed.

Migmatite doming must have therefore occurred as a late feature at low-pressure (M_3) conditions (~5–6 kbar and 700–730 °C) after top-to-the-NNE shearing on the KSZ, and upon crossing the muscovite dehydration melting reaction. Although lower-crustal isostasy-driven flow during crustal extension has been suggested as a mechanism to produce such upright contractional features at the center of migmatite domes (Kruckenberg et al., 2011; Rey et al., 2011, 2017), the predicted sequence of deformation is inconsistent with our observations. Isostasy-driven flow predicts that decompression is caused by convergent flow of a partially molten lower crust under a horizontally extending upper crust. In this scenario, we would expect high overall melt fractions and doming to occur simultaneously with shearing and opposing and divergent shear senses on all margins of the dome due to a mechanical decoupling of the migmatites with the overlying rocks. Instead, we suggest the doming, upright folding, vertical boudinage, and constriction are late features that formed under compression, and they postdate decompression and top-to-the-NNE shearing from peak M_2 pressures. The migmatite dome folds the isograds, intruding S-type granite dikes and the entire overlying metamorphic sequence, including the top-to-the-NNE shear zones (KSZ and ZSZ), and it was therefore not mechanically decoupled from the overlying rocks at the time of its formation. Doming therefore represents a separate process to the decompression of rocks from kyanite- to sillimanite-grade conditions. To explain the high-temperature N-S boudinage overprinting the upright folds and vertical boudinage, we suggest that early stages of doming resulted from constrictional strain localization in the midcrust associated with the rheological weakening that occurred upon crossing the muscovite dehydration melting reaction, whereas the latter stages of doming coincided with a change in boundary conditions, most notably, a decrease in the N-S principal stress, presumably associated the transition from overall compressional to extensional tectonics (see Fig. 23).

Origin of Top-to-the-NNE Fabrics: Synorogenic Extrusion vs. Crustal Extension

Isothermal decompression of migmatites and gneisses from 10 to 5 kbar (~35–17.5 km depth) was rapid and associated with S_3 top-to-the-NNE shearing on the normal-sense Koronos and Zas shear zones. If this normal-sense shearing occurred synchronously with SW-directed thrusting within or under the migmatites, it would result in synorogenic ductile extrusion in an overall compressional setting (Law et al., 2006; Searle et al., 2006, 2010; Searle, 2010). Ductile extrusion can explain the decompression *P-T* path and extensional fabrics recoded in several other Barrovian metamorphic terranes in compression, including the Greater Himalayan Series, the Lepontine dome, and the Tauern Window in the Alps. There is an abundance of evidence for SSW-verging thick-skinned thrusting and compression across Naxos, and it seems likely that more thick-skinned thrusts are preserved at depth under the migmatites.

We propose that normal-sense shearing on the Koronos and Zas shear zones occurred due to extrusion in an overall crustal thickening scenario based on five key reasons: (1) If the crust was extending, we would not expect horizontal constrictional strains associated with doming. NNE-SSW crustal extension clearly produced NNE-SSW pure shear boudinage under M_3 conditions, which postdated upright F_3 folding in the migmatite dome. Because F_3 folding predated NNE-SSW extension but postdated movement on the KSZ, extrusion and top-to-the-NNE shearing on the KSZ and ZSZ must also have predated extension. (2) The KSZ and ZSZ record only top-to-the-NNE kinematics on all margins of the dome and were therefore active prior to doming. They are not multidivergent shear zones as predicted by extensional dome models (Kruckenberg et al., 2010, 2011; Rey et al., 2011, 2017). (3) The KSZ and ZSZ are completely discordant to the NPDS at a higher structural level, which truncates them (see Figs. 3 and 4), and the S_3 foliation associated with the Zas and Koronos shear zones is refolded by F_3 folds, which in turn are cut by the NPDS. Therefore, these shear zones formed earlier than and are separate structures from the NPDS, which exhibits both brittle and ductile deformation features. (4) If movement on the KSZ represents the deep lower-crustal signature of a detachment fault associated with crustal extension, then we would expect rapid cooling and migration of the brittle-ductile transition (England and Jackson, 1987). There is no evidence to suggest this occurred. Instead, isothermal decompression of migmatites to ~5 kbar led to cooling by <30 °C upon their exhumation to the midcrust. This isothermal decompression *P-T* path would be predicted if the KSZ and ZSZ represent stretching faults or ductile shear zones that progressed up structural section with time (Means, 1989). (5) Hydrous melting is the major anatectic process for the Naxos migmatites that was responsible for initial melting and weakening at M_2 kyanite-grade conditions. This hydration reaction acts as a large sink for water. To balance the net water budget of the deep crust, calculations require a large external supply of water. A potential water source that could drive the partial melting process could be the result of prograde dehydration reactions from underthrusted crust. Underthrusted rocks would have been experiencing prograde metamorphism and dehydration reactions at the time of migmatization in the overlying units. This could alleviate this conundrum because liberated water could migrate into the overlying migmatites and act as a source to drive anatexis. In contrast, during crustal extension, underthrusting of hydrated rocks would not occur, and we would expect dry granulite-facies rocks to underlie Naxos migmatites, which would be strong and less likely to flow or act as a source of water to drive anatexis.

If indeed the Koronos and Zas shear zones represent passive-roof stretching normal faults in an overall compressive and E-W horizontal constrictional regime, these faults would form at the top of the SW-extruding wedge, as material was returned via ductile flow toward the foreland, and by possible erosion due to melt weakening and the buoyancy and viscosity contrasts of migmatites. Together, these shear zones preserve a sequence of right-way-up metamorphic isograds, similar to the South Tibetan Detachment System (STDS) in the Himalaya, by a process of general shear (simple shear plus pure shear flattening) that telescoped the isograds (Jessup et al., 2006; Cottle et al., 2007; Law et al., 2006; Searle et al., 2006, 2010). Top-to-NNE shearing (S_3; Fig. 23, stage 1) first developed along the rheological boundary marking the solidus. Deformation temperatures in the KSZ exceeded 650 °C, and it was therefore responsible for the earliest and deepest stages of exhumation. With subsequent ductile flow, sheath folds developed under general shear due to high non-coaxial shear strain followed by E-W constriction (Fig. 23, stage 2).

Emplacement of hot migmatites at mid-crustal levels would have provided the thermal perturbation in the hanging wall of the KSZ to nucleate posttectonic garnets that crosscut S_2 kyanite-grade and S_3 top-to-the-NNE shearing fabrics and M_3 sillimanite-biotite intergrowths with strong annealing textures (Fig. 23, stage 2). This thermal pulse would also explain the intrusion of S-type leucogranites into the Koronos Unit that crosscut the S_3 blastomylonite fabric. All structures were then gently domed about a N-S axis that resulted in the frozen bull's-eye isograd pattern.

Following extrusion of migmatites to shallower crustal levels and F_3 upright folding, initiation of NNE-SSW regional extension produced retrograde greenschist-facies, top-to-the-NNE (S_3) mylonite fabrics associated with the NPDS, which truncated, reactivated, and utilized subparallel (S_{2a}) crenulation cleavages and top-to-the-SW (S_{2b}) fabrics. NNE-SSW boudinage of amphibolites in the CHSZ indicate a rapid switch from crustal thickening to NNE-SSW regional extension during the closure of the M_3 event.

Figure 23 (*on following page*). Extrusion model to explain and visualize the sequence of deformation events that created S_3 top-to-the-NNE shear fabrics on the Koronos shear zone (KSZ) and Zas shear zone (ZSZ) and the decompression of high-grade rocks on Naxos from 10 to 5 kbar followed by migmatite doming. U-Pb age data will be presented in a future study. Samples TL15, TL66, TL67, and TLN54 are approximately located, and their spatial evolution is illustrated as the model progresses. Stage 1—Pre–18 Ma: Prograde burial and metamorphism of the Koronos and Core Units forming F_1 isoclinal folds. Stage 2—Peak M_2 kyanite-grade metamorphism and partial melting of the Core Unit. Stage 3—Synorogenic extrusion of the Koronos and Core Units under passive-roof normal faults. Stage 4—Rotation of principal stress axes causing constriction at M_3 sillimanite-grade conditions. Stage 5—Onset of extensional tectonics and initiation of Naxos-Paros detachment system, which truncates and is discordant to all earlier structures. Mineral abbreviations follow Whitney and Evans (2010).

Exhumation of the Core Complex and Regional Extension

Regional extension subsequent to 15 Ma (Fig. 23, stage 3; a future paper will present the U-Th-Pb ages) was accommodated by normal faulting and horizontal NNE-SSW–directed pure shear ductile boudinage. In the upper crust, normal faults sole into and crosscut a low-angle detachment horizon (NPDS). This structure, which is discordant to, and truncates, the folding, migmatite dome, and metamorphic stratigraphy within the core complex, caused extreme telescoping of previously frozen-in isograds beneath it, and rapid footwall cooling at rates of 60–90 °C m.y.$^{-1}$ along a peak thermal gradient of 40 °C km^{-1}. The onset of extension is recorded by the kink in the *P-T* path while the migmatites were at the close of the M_3 event at ~5 kbar and 690 °C (Fig. 22). The Naxos I-type granodiorite intruded into the metamorphic sequence at ca. 12.2 Ma, and it is cut by the NPDS, with brittle-ductile deformation features including pseudotachylytes, suggesting the arrival of the core complex at the brittle-ductile transition at this time. In contrast, in the ductile crust, extensional strain during the latter stages of the sillimanite-grade event was accommodated by mainly NNE-SSW–directed pure shear with extensional strains of up to ~50%, resulting in horizontal boudinage and stretching that overprinted earlier compressional features (e.g., Figs. 9 and 10) and that formed the elliptical dome structure.

Significance of E-W Shortening

This study and several others highlight a significant component of E-W shortening on Naxos (e.g., Virgo et al., 2018). This shortening occurred during migmatite dome formation and F_3 folding and occurred prior to and synchronous with regional NNE-SSW extension. All structures, including the NPDS, aplite sills within the 12.2 Ma granodiorite, and even Pliocene–Pleistocene sediments, are folded or tilted around the island, which cannot be explained by isostatic footwall rebound alone. It is unclear what the origin of this shortening was during the Miocene, as it would have predated movement on the North Anatolian fault, which commenced at ca. 11 Ma (e.g., Menant et al., 2013). Convergent E-W lower-crustal flow during NNE-SSW extension (Kruckenberg et al., 2011) could possibly explain E-W shortening in the middle of the migmatite dome, but this should have been simultaneous with NNE-SSW extensional boudinage and would exclusively affect migmatites, in disagreement with our observations of F_3 folding also affecting the entire carapace. Furthermore, many islands in the Cyclades document a significant component of E-W shortening (e.g., Virgo et al., 2018, and references therein), indicating it was a regional compressive stress and not related to ductile convergent flow of migmatites under crustal extension (Kruckenberg et al., 2011). It is possible that Miocene E-W shortening was related to the westward escape of Anatolia into the Cyclades (e.g., Phillipon et al., 2014). This would have been accommodated via dextral strike-slip reactivation of the eastward Vardar suture zone to the north of the Cyclades, and possibly related to strike-slip movement on the Mid-Cycladic Lineament (e.g., Malandri et al., 2016), prior to rollback on the Hellenic subduction zone. This scenario could produce horizontal constriction-type conditions due to shortening in all directions, like those recorded in the Naxos migmatite dome. This would have been followed by NNE-SSW extension following a change in boundary stresses, either due to the onset of slab rollback on the Hellenic subduction zone or removal of lithospheric mantle during the mid-Miocene. Doming of Pleistocene sediments on the margins of Naxos is probably related to a component of recent E-W transpression, which possibly resulted in a 20° counterclockwise rotation about a vertical axis (Kissel and Laj, 1988) and the series of conjugate NNE-SSW–trending and NNW-SSE–trending strike-slip faults that crosscut the island.

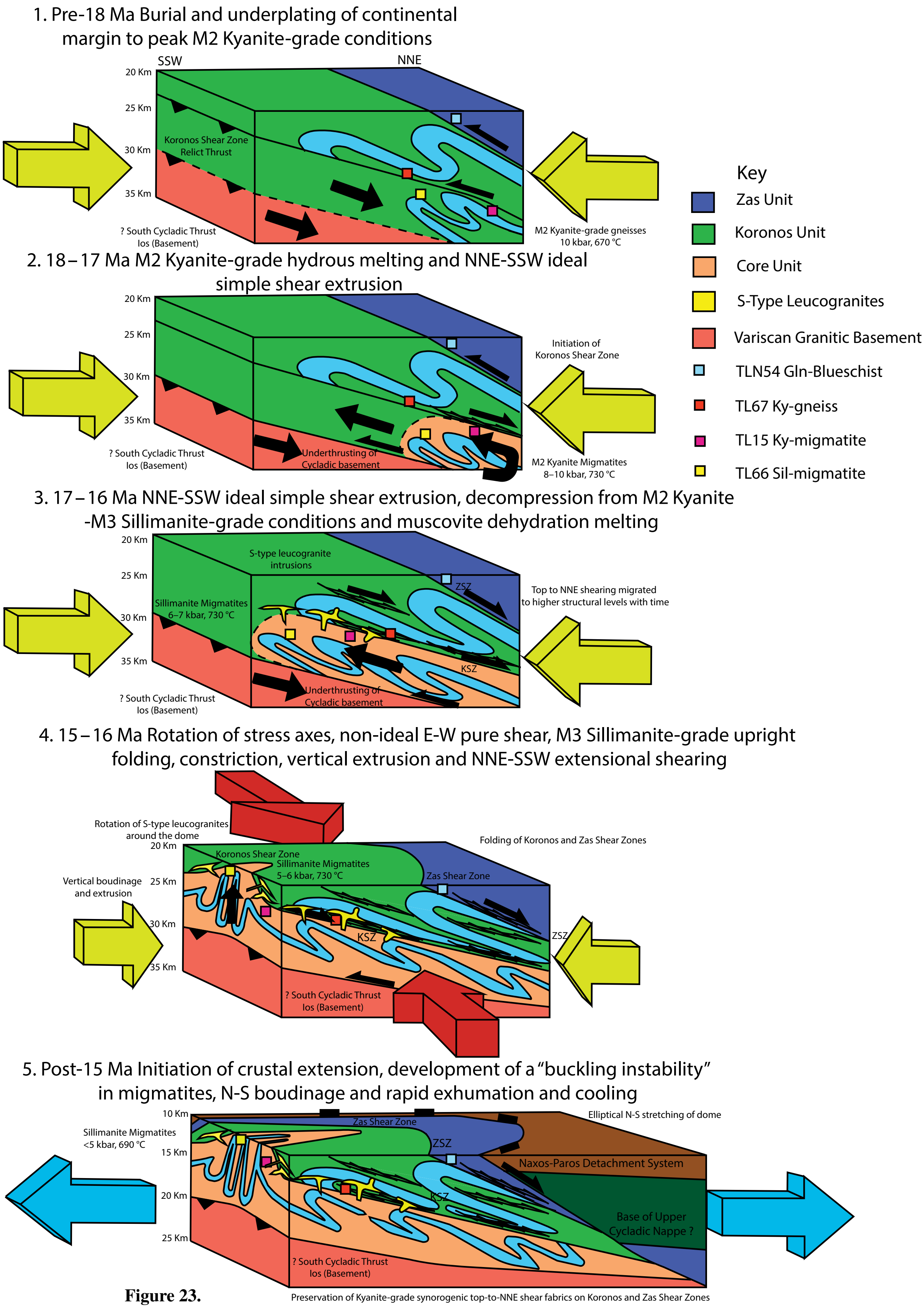
1. Pre-18 Ma Burial and underplating of continental margin to peak M2 Kyanite-grade conditions
SSW
NNE
20 Km
25 Km
30 Km
35 Km
Koronos Shear Zone Relict Thrust
? South Cycladic Thrust Ios (Basement)
M2 Kyanite-grade gneisses 10 kbar, 670 °C
2. 18 – 17 Ma M2 Kyanite-grade hydrous melting and NNE-SSW ideal simple shear extrusion
Initiation of Koronos Shear Zone
Underthrusting of Cycladic basement
M2 Kyanite Migmatites 8–10 kbar, 730 °C
3. 17 – 16 Ma NNE-SSW ideal simple shear extrusion, decompression from M2 Kyanite -M3 Sillimanite-grade conditions and muscovite dehydration melting
S-type leucogranite intrusions
Sillimanite Migmatites 6–7 kbar, 730 °C
ZSZ
KSZ
Top to NNE shearing migrated to higher structural levels with time
4. 15 – 16 Ma Rotation of stress axes, non-ideal E-W pure shear, M3 Sillimanite-grade upright folding, constriction, vertical extrusion and NNE-SSW extensional shearing
Rotation of S-type leucogranites around the dome
Folding of Koronos and Zas Shear Zones
Koronos Shear Zone
Sillimanite Migmatites 5–6 kbar, 730 °C
Zas Shear Zone
Vertical boudinage and extrusion
5. Post-15 Ma Initiation of crustal extension, development of a "buckling instability" in migmatites, N-S boudinage and rapid exhumation and cooling
10 Km
15 Km
Sillimanite Migmatites <5 kbar, 690 °C
Elliptical N-S stretching of dome
Naxos-Paros Detachment System
Base of Upper Cycladic Nappe ?
Preservation of Kyanite-grade synorogenic top-to-NNE shear fabrics on Koronos and Zas Shear Zones
Key
Zas Unit
Koronos Unit
Core Unit
S-Type Leucogranites
Variscan Granitic Basement
TLN54 Gln-Blueschist
TL67 Ky-gneiss
TL15 Ky-migmatite
TL66 Sil-migmatite

Figure 23.

Possible Comparisons to Other Mountain Belts

Naxos records the entire evolution of an orogeny, from ophiolite obduction to postorogenic collapse, and it displays similarities to many well-studied geological areas, including the following:

(1) Oman/United Arab Emirates: The relatively unmetamorphosed hanging wall of the NPDS displays an ophiolitic mélange similar to the Haybi oceanic unit, directly underlying the sole of the Oman/United Arab Emirates ophiolite (Searle and Cox, 2002). This unit is interpreted to represent off-axis alkali seamounts with carbonate caps that formed on the lower plate and were scraped off into a mélange during the subduction/obduction process. Oman also records blueschist- and eclogite-facies rocks that are bounded by normal-sense extensional shear zones within the continental margin sequence under the ophiolite. These formed ~15 m.y. after the initiation of obduction as the leading edge of the Arabian continental margin attempted to subduct. A comparable ophiolite obduction scenario could also have taken place in the Cyclades prior to high-pressure metamorphism of the Cycladic Blueschists, which also represent the leading edge of the Cycladic continental margin.

(2) The Tauern Window, Austrian Alps: The metamorphic footwall of the Naxos MCC records Barrovian metamorphism due to the stacking of various tectonic slices. Many comparisons can be drawn to the Tauern Window in the Austrian Alps, one of the most intensely studied overthrust terranes on the planet (e.g., Schmid et al., 2013; Smye et al., 2011, and references therein). It is composed of an amphibolite-facies metamorphic core that underlies discrete slices of eclogite- and blueschist-facies thrust sheets. Barrovian metamorphism was a result of overthrusting Austroalpine nappes derived from the Adriatic continental margin (upper plate), in some respects like the Upper Cycladic Nappe (Jolivet et al., 2013) and Cycladic Blueschists.

(3) The Greater Himalayan Series (GHS) in the Himalaya: The metamorphic core of the Himalaya records an almost identical *P-T-D* path to that observed on Naxos, with kyanite-grade conditions followed by isothermal decompression through the muscovite dehydration melting reaction to lower-pressure sillimanite-grade conditions and S-type leucogranite formation. Decompression occurred during SW-directed extrusion of the GHS in an overall compressional setting, bounded by the Main Central thrust at the base and the South Tibetan Detachment System at the top, which were active at the same time. The extensional top-to-the-NE shear fabrics on the STDS formed due to exhumation of footwall material beneath a fixed hanging wall in an overall compressional setting, and they preserve a sequence of right-way-up metamorphic isograds that are strikingly similar to the Koronos and Zas shear zones on Naxos. Naxos has gone one stage further than the Himalaya and represents a collapsed orogen that beautifully documents the transition from an overall compressional to extensional environment that coincided with the latter stages of migmatite dome formation.

(4) Betic-Rif, Spain: This structure records the transition from overall compressional to extensional tectonics. Eocene to Oligocene south-directed subduction was associated with high-pressure metamorphism of the Iberian continental margin and was followed by significant crustal thinning and coeval heating during the early stages of arc formation (e.g., Platt et al., 2013). The mechanisms that caused extension within the hinterland of this orogen are debated, but removal of lithospheric mantle seems to be the most likely scenario and would result in upwelling of the asthenosphere, causing heating, a rise in topography, crustal extension, and rapid westward rollback on the West Mediterranean subduction zone (Platt et al., 2013, and references therein). Comparable processes could have caused extension within the Aegean during the late Miocene. An important difference between Naxos and the Betics is that there is substantial kyanite-grade metamorphism and no subcontinental lithospheric mantle exhumed in the Cyclades, as the Moho lies at ~25 km depth and deepens to the north (Cossette et al., 2016).

CONCLUSIONS

The tectonothermal evolution of the Naxos metamorphic core complex is more complicated than can be explained purely by crustal extension. The data presented in this study demonstrate that Naxos records a prolonged history of compression, resulting in crustal thickening and regional metamorphism, followed by extension. Eight key points can be made:

(1) The footwall of the Naxos MCC represents three tectono-metamorphic units that each record contrasting *P-T-D-t* paths, and each represents a series of nappes that were stacked due to prolonged crustal thickening. During this process, rocks were buried and metamorphosed diachronously as the geothermal gradient conductively increased over time, and eventually resulted in Barrovian metamorphism and partial melting. The sequence records M_1 blueschist-facies conditions at the top to M_2–M_3 upper-amphibolite-facies migmatites at the base.

(2) These nappes were juxtaposed against one another by top-to-the-NNE normal-sense ductile extensional shear zones that coincided with peak M_2–M_3 Barrovian conditions at the deepest levels. This resulted in telescoping of previously frozen-in isograds during extrusion of footwall rocks, similar to the normal-sense shear zone of the STDS bounding the top of the Greater Himalayan Series. Deformation migrated from deep to shallow structural levels with time and was associated with general shear. These shear zones predated doming and are discordant to, and predated, normal faulting related to crustal extension. In contrast, the low-angle normal faults truncate all structures and metamorphic stratigraphy in their footwall.

(3) The hanging wall of the NPDS dominantly consists of trench mélange formed along the base of the obducting ophiolite. This may record further evidence for a relict ophiolite obduction event, as seen on Tinos (Lamont, 2018), which preceded M_1 high-pressure metamorphism in the Cyclades. Ophiolitic rocks are exposed at the highest structural level across the Cyclades. Miocene–Pliocene fluvial sediments and conglomerates were deposited unconformably on top of this, suggesting that topography was much higher during the Miocene.

(4) At the deepest levels, M_2 kyanite-grade hydrous melting (Eq. 6) was the dominant melting process and was followed by isothermal decompression from ~10 kbar and 680–750 °C to 5–6 kbar and 700–730 °C. With small degrees of partial melting, the migmatites weakened and decompressed under a passive-roof normal fault (KSZ). The hottest and most deeply buried rocks decompressed through the muscovite dehydration melting reaction (Eq. 4), locally producing up to 20%–25% melt. This advective process may have acted as substantial source of heat applicable to many Barrovian metamorphic terranes.

(5) The migmatite dome is a late feature, and it was formed in a constrictive stress regime at lower-pressure M_3 sillimanite-grade conditions. This postdated top-to-the-NNE shearing on the Koronos and Zas shear zones and folded the entire metamorphic sequence. Structural analysis of polyphase deformation within the center of the dome indicates a major change in stress regime from NNE-SSW compression to dominantly E-W contraction and later NNE-SSW extension, coinciding with doming.

(6) Naxos records the transition from compression to extension in the Cyclades. The formation of the sillimanite-grade migmatites marks the climax of high-grade metamorphism in the Cyclades, and no evidence for crustal thickening postdates this event. Within the dome, N-S pure shear horizontal extensional boudinage occurred during the end of the M_3 sillimanite-grade event and overprints earlier

upright F_3 isoclinal folds and vertical boudinage. This corresponds to the final stage of migmatite dome formation and marks the transition from regional compression to extension in the Cyclades.

(7) Regional extension and crustal thinning were accommodated by brittle-ductile normal faulting that crosscut and is discordant to all footwall structures. It attenuated and telescoped the frozen-in metamorphic isograds to produce metamorphic field gradients of up to 700 °C km^{-1}, particularly in west Naxos. In the ductile crust, horizontal N-S pure shear boudinage accommodated extensional strains of up to 50%. These structures postdate all earlier collisional features, and brittle-ductile normal faulting was responsible for the final stage of exhumation from 5 kbar (~17.5 km depth) to the surface along an apparent geothermal gradient of 40 °C km^{-1}.

(8) Three types of extensional fabrics are recorded on Naxos: (i) SW extrusion from the subduction zone, as recorded in the Zas Unit with top-to-the-NE fabrics, (ii) synorogenic SSW extrusion of migmatites and high-grade gneisses under a passive-roof fault (Koronos and Zas shear zones), with top-to-the-NNE kinematic indicators, and (iii) top-to-NNE extensional fabrics due to late brittle-ductile crosscutting normal faults related to crustal extension and cooling (NPDS). This movement was superimposed on earlier fabrics along the western side of the core complex. In particular, extensional fabrics on the Koronos and Zas shear zones within the metamorphic footwall were responsible for synorogenic extrusion of kyanite- to sillimanite-grade gneisses and migmatites that predate extension. These are truncated and crosscut by later S-type granite dikes and lower-grade fabrics and structures related to crustal extension.

Because the timing constraints and rates of deformation, metamorphism, and partial melting are crucial for resolving the complete *P-T-D-t* history of Naxos to a high resolution, we will provide new U-Th-Pb age data in a future paper. We also present a fully integrated tectonic model for the development and exhumation of the Naxos MCC and show that Naxos documents the entire evolution of what we term the "Aegean orogeny." This mountain belt records a full orogenic cycle from ophiolite obduction, to high-pressure metamorphism, through subduction-related exhumation, crustal thickening, and regional metamorphism to postorogenic extension. We demonstrate that the transition from compression to extension on Naxos coincided with the latter stages of migmatite formation at ca. 15 Ma, corresponding with the timing of a major slowdown in the convergence rate between Nubia and Eurasia (DeMets et al., 2015). We build on this structural and metamorphic framework and show that crustal extension was associated with rapid cooling and brittle-ductile normal faulting and was responsible for the final stages of core complex exhumation, which postdated peak metamorphism, partial melting, and synorogenic extrusion.

ACKNOWLEDGMENTS

This work forms part of T.N. Lamont's doctoral project, which was funded by the Natural Environment Research Council (NERC; grant NE/L0021612/1). Analytical work at the NERC Isotope Geosciences Laboratory was funded by NERC Isotope Geosciences Facilities Steering Committee grant IP-1597-1115. We thank Philip England, Anthony Watts, Dave Wallis, Lars Hansen, and Tyler Ambrose for thought-provoking and critical discussion. We extend thanks to Callum Higgins, William Nash, and Anna Bidgood for assistance in the field, Adrian Wood for assistance with mineral separation, Owen Green and Jonathan Wells for thin section preparation, and Gren Turner, Jeremy Rushton, and Jon Wade for analytical assistance. Chris Ballhaus and Christoph Von Hagkne are thanked for thorough reviews, which greatly improved the quality of the manuscript, and Nick Timms, Chris Kirkland, and Aaron Cavosie are thanked for handling the manuscript and providing further comments. We finally thank University College, Oxford for travel bursaries covering fieldwork expenses and the University of Oxford and NERC for generously covering publication and open access costs.

APPENDIX: GLOSSARY

MCC—metamorphic core complex.

Moutsana detachment—The brittle low-angle normal fault that was partly responsible for exhuming the island.

NCDS—North Cycladic Detachment System, a brittle-ductile low-angle normal fault and series of shear zones that display top-to-the-NE kinematics exposed on the north coast of Mykonos, Tinos, and Andros, juxtaposing I-type granites and blueschists in the footwall from relatively less metamorphosed ophiolitic rocks and sediments in the hanging wall.

NPDS—Naxos-Paros Detachment System, the brittle-ductile low-angle normal-sense extensional shear zone that cuts all previous metamorphic stratigraphy and produces telescoping of isograds on the western side of the island.

Carapace—the metasedimentary units that overlie the migmatite dome, including the Zas Unit and Koronos Unit.

CHSZ—Core high-strain zone, a zone of upright folded marbles and amphibolites that are affected by vertical and horizontal boudinage at the center of the migmatite dome, best exposed in the Boulibas and Kinadaros quarries.

Upper Cycladic Nappe—The relatively unmetamorphosed, ophiolitic and sedimentary hanging wall of the Naxos metamorphic core complex and the hanging wall of the North Cycladic detachment system on Mykonos, Tinos, and Andros.

GHS—Greater Himalayan Series.

STDS—South Tibetan Detachment System.

TTG—Tonalite-trondhjemite-granodiorite.

Zas Unit—A blueschist-facies unit that can be regionally correlated with the Cycladic Blueschist Unit, representing the distal Cycladic (Adriatic) continental margin.

Koronos Unit—A kyanite-grade amphibolite-facies unit that represents the more-proximal continental margin, forming the deeper carapace to the metamorphic core complex.

Core Unit—The kyanite- to sillimanite-grade core of the island, with migmatites, orthogneisses, and structurally repeated and uprightly folded and boudinaged marbles and amphibolites that form a doubly plunging migmatite dome.

Main ultramafic horizon—A semicontinuous band of amphibolites directly above the Koronos shear zone that wraps around the Core Unit, locally containing enclaves of ultramafic lithologies.

ZSZ—Zas shear zone, the top-to-the-NE greenschist-facies shear zone separating blueschist-facies rocks of the Zas Unit (on top) from amphibolite-facies rocks of the Koronos Unit (below).

KSZ—Koronos shear zone, the top-to-the-NE, upper-amphibolite-facies shear zone bounding the migmatite dome (Core Unit), which is folded and cut by S-type leucogranites.

M_1—High-pressure–low-temperature blueschist-facies metamorphism that locally reached eclogite-facies conditions on Syros, Tinos, and Sifnos.

M_2—Regional metamorphism that reached greenschist-facies conditions in the Cycladic Blueschists (Zas Unit) and kyanite-grade conditions in the Koronos and Core Units.

M_3—Regional metamorphism that is associated with sillimanite-grade conditions, partial melting, and S-type leucogranite intrusion at the deepest levels of Naxos in the Core Unit.

P-T-D-(*t*) paths—Pressure, temperature, deformation, and time paths.

F_1—First generation of folds, which show isoclinal to recumbent geometries and developed during burial and SW-directed thrusting.

F_2—Second generation of folds to form, which display sheath and isoclinal geometries that refold the F_1 folds, and that developed during top-to-the-NNE shearing, during exhumation.

F_3—Last generation of folds that formed under lower-pressure conditions. These are upright folds that trend along NNE-SSW axes across all units and are boudinaged both vertically and horizontally in the Core High-Strain Zone.

REFERENCES CITED

Alsop, G.I., and Holdsworth, R.E., 2006, Sheath folds as discriminators of bulk strain type: Journal of Structural Geology, v. 28, p. 1588–1606, https://doi.org/10.1016/j.jsg.2006.05.005.

Andriessen, P.A.M., Boelrijk, N.A.I.M., Hebeda, E.H., Priem, H.N.A., Verdurmen, E.A.T., and Verschure, R.H., 1979, Dating the events of metamorphism and granitic magmatism in the Alpine orogen of Naxos (Cyclades, Greece): Contributions to Mineralogy and Petrology, v. 69, p. 215–225, https://doi.org/10.1007/BF00372323.

Armstrong, R.L., 1982, Cordilleran metamorphic core complexes from Arizona to southern Canada: Annual Review of Earth and Planetary Sciences, v. 10, p. 129–154, https://doi.org/10.1146/annurev.ea.10.050182.001021.

Ashworth, J.R., 1975, The sillimanite zones of the Huntly Portsoy area in the north-east Dalradian, Scotland: Geological Magazine, v. 112, p. 113–136, https://doi.org/10.1017/S0016756800045817.

Ashworth, J.R., 1979, Textural and mineralogical evolution of migmatites: Geological Society of London, Special Publications, v. 8, no. 1, p. 357–361, https://doi.org/10.1144/GSL.SP.1979.008.01.40.

Avigad, D., 1998, High-pressure metamorphism and cooling on SE Naxos (Cyclades, Greece): European Journal of Mineralogy, v. 10, p. 1309–1320, https://doi.org/10.1127/ejm/10/6/1309.

Avigad, D., Baer, G., and Heimann, A., 1998, Block rotations and continental extension in the central Aegean Sea: Palaeomagnetic and structural evidence from Tinos and Mykonos: Earth and Planetary Science Letters, v. 157, p. 23–40, https://doi.org/10.1016/S0012-821X(98)00024-7.

Axen, G.J., 2007, Research focus: Significance of large-displacement, low-angle normal faults: Geology, v. 35, p. 287–288, https://doi.org/10.1130/0091-7613(2007)35[287:RFSOLL]2.0.CO;2.

Baker, J., and Matthews, A., 1994, Textural and isotopic development of marble assemblages during the Barrovian-style M_2 metamorphic event, Naxos, Greece: Contributions to Mineralogy and Petrology, v. 116, p. 130–144, https://doi.org/10.1007/BF00310695.

Baker, J., Bickle, M.J., Buick, I.S., Holland, T.J.B., and Matthews, A., 1989, Isotopic and petrological evidence for the infiltration of water-rich fluids during the Miocene M_2 metamorphism on Naxos, Greece: Geochimica et Cosmochimica Acta, v. 53, p. 2037–2050, https://doi.org/10.1016/0016-7037(89)90323-2.

Bhattacharya, L., Mohanty, L., Maji, A., Sen, S.K., and Raith, M., 1992, Non-ideal mixing in the phlogopite-annite binary: Constraints from experimental data on Mg-Fe partitioning and a reformulation of the biotite-garnet geothermometer: Contributions to Mineralogy and Petrology, v. 111, p. 87–93, https://doi.org/10.1007/BF00296580.

Bickle, M.J., and Baker, J., 1990, Advective-diffusive transport of isotopic fronts: An example from Naxos, Greece: Earth and Planetary Science Letters, v. 97, p. 78–93, https://doi.org/10.1016/0012-821X(90)90100-C.

Bickle, M.J., Hawkesworth, C., England, P.C., and Athey, D., 1975, A preliminary thermal model for regional metamorphism in the eastern Alps: Earth and Planetary Science Letters, v. 26, p. 13–28, https://doi.org/10.1016/0012-821X(75)90173-9.

Bolhar, R., Ring, U., and Ireland, T.R., 2017, Zircon in amphibolites from Naxos, Aegean Sea, Greece: origin, significance and tectonic setting: Journal of Metamorphic Geology, v. 35, p. 413–434, https://doi.org/10.1111/jmg.12238.

Bröcker, M., and Franz, L., 1998, Rb-Sr isotope studies on Tinos island (Cyclades, Greece): Additional time constraints for metamorphism, extent of infiltration-controlled overprinting and deformational activity: Geological Magazine, v. 135, p. 369–382, https://doi.org/10.1017/S0016756898008681.

Brown, M., 2002, Retrograde processes in migmatites and granulites revisited: Journal of Metamorphic Geology, v. 20, p. 25–40, https://doi.org/10.1046/j.0263-4929.2001.00362.x.

Buick, I.S., 1991a, Mylonite fabric development on Naxos, Greece: Journal of Structural Geology, v. 13, p. 643–655, https://doi.org/10.1016/0191-8141(91)90027-G.

Buick, I.S., 1991b, The late Alpine evolution of an extensional shear zone, Naxos, Greece: Journal of the Geological Society [London], v. 148, p. 93–103, https://doi.org/10.1144/gsjgs.148.1.0093.

Buick, I.S., and Holland, T.J.B., 1989, The *P-T-t* path associated with crustal extension, *in* Daly, J.S., Cliff, R.A., and Yardley, W.D., eds., Evolution of Metamorphic Belts: Geological Society of London Special Publication 43, p. 365–369.

Buick, I.S., and Holland, T.J.B., 1991, The nature and distribution of fluids during amphibolite-facies metamorphism, Naxos (Greece): Journal of Metamorphic Geology, v. 9, p. 301–314, https://doi.org/10.1111/j.1525-1314.1991.tb00525.x.

Burg, J.P., Guiraud, M., Chen, G.M., and Li, G.C., 1984, Himalayan metamorphism and deformations in the North Himalayan belt (southern Tibet, China): Earth and Planetary Science Letters, v. 69, p. 391–400, https://doi.org/10.1016/0012-821X(84)90197-3.

Caddick, M.J., Konopásek, J., and Thompson, A.B., 2010, Preservation of garnet growth zoning and the duration of prograde metamorphism: Journal of Petrology, v. 51, p. 2327–2347, https://doi.org/10.1093/petrology/egq059.

Cao, S., Neubauer, F., Bernroider, M., and Liu, J., 2013, The lateral boundary of a metamorphic core complex: The Moutsounas shear zone on Naxos, Cyclades, Greece: Journal of Structural Geology, v. 54, p. 103–128, https://doi.org/10.1016/j.jsg.2013.07.002.

Cao, S., Neubauer, F., Bernroider, M., Genser, J., Liu, J., and Friedl, G., 2017, Low-grade retrogression of a high-temperature metamorphic core complex: Naxos, Cyclades, Greece: Geological Society of America Bulletin, v. 129, p. 93–117, https://doi.org/10.1130/B31502.1.

Carmichael, D.M., 1969, On the Mechanism of Prograde Metamorphic Reactions in Quartz-Bearing Pelitic Rocks: Contributions to Mineralogy and Petrology, v. 20, p. 244–267, https://doi.org/10.1007/BF00377479.

Cobbold, P.R., and Quinquis, H., 1980, Development of sheath folds in shear regimes: Journal of Structural Geology, v. 2, p. 119–126, https://doi.org/10.1016/0191-8141(80)90041-3.

Coggon, R., and Holland, T.J.B., 2002, Mixing properties of phengitic micas and revised garnet-phengite thermobarometers: Journal of Metamorphic Geology, v. 20, p. 683–696, https://doi.org/10.1046/j.1525-1314.2002.00395.x.

Collins, W.J., Van Kranendonk, M.J., and Teyssier, C., 1998, Partial convective overturn of Archaean crust in the east Pilbara Craton, Western Australia: Driving mechanisms and tectonic implications: Journal of Structural Geology, v. 20, p. 1405–1424.

Coney, P.J., 1980, Cordilleran metamorphic core complexes: An overview, *in* Crittenden, M.D., Jr., Coney, P.J., and Davis, G.H., eds., Cordilleran Metamorphic Core Complexes: Geological Society of America Memoir 153, p. 7–34, https://doi.org/10.1130/MEM153-p7.

Conrad, W.K., Nicholls, L.A., and Wall, V.J., 1988, Water-saturated and -undersaturated melting of metaluminous and peraluminous crustal compositions at 10 kb: Evidence for the origin of silicic magmas in the Taupo volcanic zone, New Zealand, and other occurrences: Journal of Petrology, v. 29, p. 765–803, https://doi.org/10.1093/petrology/29.4.765.

Corfield, R.I., and Searle, M.P., 2000, Crustal shortening estimates across the north Indian continental margin, Ladakh, NW India, *in* Asif Khan, M., Treloar, P.J., Searle, M.P., and Qasim Jan, M., eds., Tectonics of the Nanga Parbat Syntaxis and the Western Himalaya: Geological Society of London Special Publication 170, p. 395–410, https://doi.org/10.1144/GSL.SP.2000.170.01.21.

Cossette, É., Audet, P., Schneider, D., and Grasemann, B., 2016, Structure and anisotropy of the crust in the Cyclades, Greece, using receiver functions constrained by in situ rock textural data: Journal of Geophysical Research–Solid Earth, v. 121, p. 2661–2678, https://doi.org/10.1002/2015JB012460.

Cottle, J.M., Jessup, M.J., Newell, D.J., Searle, M.P., Law, R.D., and Horstwood, M.S.A., 2007, Structural insights into the early stages of exhumation along an orogen-scale detachment: The South Tibetan detachment system, Dzakaa Chu section, Eastern Himalaya: Journal of Structural Geology, v. 29, p. 1781–1797, https://doi.org/10.1016/j.jsg.2007.08.007.

Cruciani, G., Franceschelli, M., Elter, F.M., Puxeddu, M., and Utzeri, D., 2008, Petrogenesis of Al-silicate-bearing trondhjemitic migmatites from NE Sardinia, Italy: Lithos, v. 102, p. 554–574, https://doi.org/10.1016/j.lithos.2007.07.023.

Deer, W.A., Howie, R.A., and Zussman, J., 1992, An Introduction to the Rock Forming Minerals (2nd ed.): Harlow, Essex, UK Longman Scientific & Technical, 528 p.

DeMets, C., Iaffaldano, G., and Merkouriev, S., 2015, High-resolution Neogene and Quaternary estimates of Nubia–Eurasia–North America plate motion: Geophysical Journal International, v. 203, p. 416–427, https://doi.org/10.1093/gji/ggv277.

Dixon, J.E., and Robertson, A.H.F., eds., 1984, The Geological Evolution of the Eastern Mediterranean: Geological Society Special Publication, v. 17, p. 824.

Dragovic, B., Samanta, L.M., Baxter, E.F., and Selverstone, J., 2012, Using garnet to constrain the duration and rate of water-releasing metamorphic reactions during subduction: An example from Sifnos, Greece: Chemical Geology, v. 314, p. 9–22, https://doi.org/10.1016/j.chemgeo.2012.04.016.

Duchêne, S., Aïssa, R., and Vanderhaeghe, O., 2006, Pressure-temperature-time evolution of metamorphic rocks from Naxos (Cyclades, Greece): Constraints from thermobarometry and Rb/Sr dating: Geodinamica Acta, v. 19, p. 301–321, https://doi.org/10.3166/ga.19.301-321.

Durr, S., Altherr, R., Keller, J., Okrusch, M., and Seidel, E., 1978, The median Aegean crystalline belt: stratigraphy, structure, metamorphism, magmatism, *in* Cloos, H., Roeder, D., and Schmidt, K., eds., Alps, Apennines, Hellenides: Schweizerbart, Stuttgart, p. 455–476.

England, P.C., 1978, Some thermal considerations of the Alpine metamorphism, past, present and future: Tectonophysics, v. 46, p. 21–40, https://doi.org/10.1016/0040-1951(78)90103-8.

England, P.C., and Holland, T.J.B., 1979, Archimedes and the Tauern eclogites: The role of buoyancy in the preservation of exotic eclogite blocks: Earth and Planetary Science Letters, v. 44, p. 287–294, https://doi.org/10.1016/0012-821X(79)90177-8.

England, P.C., and Jackson, J., 1987, Migration of the seismic-aseismic transition during uniform and nonuniform extension of the continental lithosphere: Geology, v. 15, p. 291–294, https://doi.org/10.1130/0091-7613(1987)15<291:MOTSTD>2.0.CO;2.

England, P.C., and Richardson, S.W., 1977, The influence of erosion upon the mineral facies of rocks from different metamorphic environments: Journal of the Geological Society [London], v. 134, p. 201–213, https://doi.org/10.1144/gsjgs.134.2.0201.

England, P.C., and Thompson, A.B., 1984, Pressure–temperature–time paths of regional metamorphism I. Heat transfer during the evolution of regions of thickened continental crust: Journal of Petrology, v. 25, p. 894–928, https://doi.org/10.1093/petrology/25.4.894.

Evans, B.W., and Guidotti, C.V., 1966, The sillimanite-potash feldspar isograd in western Maine, U.S.A.: Contributions to Mineralogy and Petrology, v. 12, p. 25–62, https://doi.org/10.1007/BF02651127.

Ez, V., 2000, When shearing is a cause of folding: Earth-Science Reviews, v. 51, p. 155–172, https://doi.org/10.1016/S0012-8252(00)00020-9.

Feenstra, A., 1985, Metamorphism of bauxites on Naxos [PhD Thesis], Utrecht, Netherlands, Rijks Universiteit.

Fletcher, R.C., and Hallet, B., 1983, Unstable extension of the lithosphere: A mechanical model for Basin-and-Range structure: Journal of Geophysical Research, v. 88, p. 7457–7466, https://doi.org/10.1029/JB088iB09p07457.

García-Casco, A., Torres-Roldán, R.L., Millán, G., Monié, P., and Haissen, F., 2001, High-grade metamorphism and hydrous melting of metapelites in the Pinos terrane (W Cuba): Evidence for crustal thickening and extension in the northern Caribbean collisional belt: Journal of Metamorphic Geology, v. 19, p. 699–715, https://doi.org/10.1046/j.0263-4929.2001.00343.x.

García-Casco, A., Haissen, F., Castro, A., El-Hmidi, H., Torres-Roldán, R.L., and Millán, G., 2003, Synthesis of staurolite in melting experiments of a natural metapelite: Consequences for the phase relations in low-temperature pelitic migmatites: Journal of Petrology, v. 44, p. 1727–1757, https://doi.org/10.1093/petrology/egg056.

Gautier, P., and Brun, J.P., 1994a, Crustal-scale geometry and kinematics of late-orogenic extension in the central Aegean (Cyclades and Evvia island): Tectonophysics, v. 238, p. 399–424, https://doi.org/10.1016/0040-1951(94)90066-3.

Gautier, P., and Brun, J.P., 1994b, Ductile crust exhumation and extensional detachments in the central Aegean (Cyclades and Evvia islands): Geodinamica Acta, v. 7, p. 57–85, https://doi.org/10.1080/09853111.1994.11105259.

Grasemann, B., Schneider, D.A., Stockli, D.F., and Iglseder, C., 2012, Miocene bivergent crustal extension in the Aegean: Evidence from the western Cyclades (Greece): Lithosphere, v. 4, p. 23–39, https://doi.org/10.1130/L164.1.

Green, E.C.R., White, R.W., Diener, J.F.A., Powell, R., Holland, T.J.B., and Palin, R.M., 2016, Activity-composition relations for the calculation of partial melting equilibria in metabasic rocks: Journal of Metamorphic Geology, v. 34, p. 845–869, https://doi.org/10.1111/jmg.12211.

Guidotti, C.V., 1984, Micas in metamorphic rocks, *in* Bailey, S.W., ed., Micas: Mineralogical Society of America Reviews in Mineralogy 13, p. 357–468, https://doi.org/10.1515/9781501508820-014.

Guilmette, C., Indares, A., and Hébert, R., 2011, High-pressure anatectic paragneisses from the Namche Barwa, Eastern Himalayan syntaxis: Textural evidence for partial melting, phase equilibria modeling and tectonic implications: Lithos, v. 124, p. 66–81, https://doi.org/10.1016/j.lithos.2010.09.003.

Hacker, B.R., Gerya, T.V., and Gilotti, J.A., 2013, Formation and exhumation of ultrahigh-pressure terranes: Elements, v. 9, p. 289–293, https://doi.org/10.2113/gselements.9.4.289.

Halpin, J.A., Clarke, G.L., White, R.W., and Kelsey, D.E., 2007, Contrasting P–T–t paths for Neoproterozoic metamorphism in macrobertson and Kemp Lands, east Antarctica: Journal of Metamorphic Geology, v. 25, p. 683–701, https://doi.org/10.1111/j.1525-1314.2007.00723.x.

Heinrich, C. A., 1982, Kyanite-eclogite to amphibolite fades evolution of hydrous mafic and pelitic rocks, Adula nappe, Central Alps: Contributions to Mineralogy and Petrology, v. 81, no. 1, p. 30–38.

Henry, D.J., Guidotti, C.V., and Thomson, J.A., 2005, The Ti-saturation surface for low-to-medium pressure metapelitic biotite: Implications for geothermometry and Ti-substitution mechanisms: The American Mineralogist, v. 90, p. 316–328, https://doi.org/10.2138/am.2005.1498.

Hinsken, T., Bröcker, M., Strauss, H., and Bulle, F., 2017, Geochemical, isotopic and geochronological characterization of listvenite from the Upper Unit on Tinos, Cyclades, Greece: Lithos, v. 282-282, p. 281–297, https://doi.org/10.1016/j.lithos.2017.02.019.

Hodges, K.V., Walker, J.D., and Wernicke, B.P., 1987, Footwall structural evolution of the Tucki Mountain detachment system, Death Valley region, southeastern California: Geological Society of London, Special Publications, v. 28, no. 1, p. 393–408, https://doi.org/10.1144/GSL.SP.1987.028.01.24.

Holdaway, M.J., 2000, Application of new experimental and garnet Margules data to the garnet-biotite geothermometer: The American Mineralogist, v. 85, p. 881–892, https://doi.org/10.2138/am-2000-0701.

Holland, T.J.B., 2009, AX: A program to calculate activities of mineral end-members from chemical analyses: http://www.esc.cam.ac.uk/research/research-groups/holland/ax (accessed July 2016).

Holland, T.J.B., and Blundy, J., 1994, Non-ideal interactions in calcic amphiboles and their bearing on amphibole-plagioclase thermometry: Contributions to Mineralogy and Petrology, v. 116, p. 433–447, https://doi.org/10.1007/BF00310910.

Holland, T.J.B., and Powell, R., 1998, An internally-consistent thermodynamic dataset for phases of petrological interest: Journal of Metamorphic Geology, v. 16, p. 309–343, https://doi.org/10.1111/j.1525-1314.1998.00140.x.

Holland, T.J.B., and Powell, R., 2003, Activity-composition relations for phases in petrological calculations: An asymmetric multicomponent formulation: Contributions to Mineralogy and Petrology, v. 145, p. 492–501, https://doi.org/10.1007/s00410-003-0464-z.

Holland, T.J.B., and Powell, R., 2011, An improved and extended internally consistent thermodynamic dataset for phases of petrological interest, involving a new equation of state for solids: Journal of Metamorphic Geology, v. 29, p. 333–383, https://doi.org/10.1111/j.1525-1314.2010.00923.x.

Holland, T.J.B., Baker, J.M., and Powell, R., 1998, Mixing properties and activity-composition relationships of chlorites in the system MgO-FeO-Al_2O_3-SiO_2-H_2O: European Journal of Mineralogy, v. 10, p. 395–406, https://doi.org/10.1127/ejm/10/3/0395.

Hollister, L.S., 1966, Garnet zoning: an interpretation based on the Rayleigh fractionation model: Science, v. 154, p. 1647–1651.

Holness, M., 2008, Decoding migmatite microstructures, *in* Sawyer, E.W., and Brown, M., eds., Working with Migmatites: Mineralogical Association of Canada Short Course 38, p. 57–76.

Huet, B., Labrousse, L., and Jolivet, L., 2009, Thrust or detachment? Exhumation processes in the Aegean: Insight from a field study on Ios (Cyclades, Greece): Tectonics, v. 28, TC3007, https://doi.org/10.1029/2008TC002397.

Indares, A., White, R.W., and Powell, R., 2008, Phase equilibria modelling of kyanite-bearing anatectic paragneiss from the central Grenville Province: Journal of Metamorphic Geology, v. 26, p. 815–836, https://doi.org/10.1111/j.1525-1314.2008.00788.x.

Jansen, J.B.H., 1973, Geological Map of Greece, Island of Naxos: Athens, Greece, Institute for Geology and Mineral Resources.

Jansen, J.B.H., and Schuiling, R.D., 1976, Metamorphism on Naxos: Petrology and geothermal gradients: American Journal of Science, v. 276, p. 1225–1253, https://doi.org/10.2475/ajs.276.10.1225.

Jessup, M.J., Law, R.D., Searle, M.P., and Hubbard, M.S., 2006, Structural evolution and vorticity of flow during extrusion and exhumation of the Greater Himalayan Slab, Mount Everest Massif, Tibet/Nepal: implications for orogen-scale flow partitioning: Geological Society, London, Special Publications, v. 268, p.379–413, https://doi.org/10.1144/GSL.SP.2006.268.01.18.

John, B.E., and Howard, K.A., 1995, Rapid extension recorded by cooling age pattern and brittle deformation, Naxos, Greece: Journal of Geophysical Research, v. 100, p. 9969–9979, https://doi.org/10.1029/95JB00665.

Jolivet, L., 2001, A comparison of geodetic and finite strain pattern in the Aegean, geodynamic implications: Earth and Planetary Science Letters, v. 187, no. 1-2, p. 95–104.

Jolivet, L., and Brun, J.P., 2010, Cenozoic geodynamic evolution of the Aegean region: International Journal of Earth Sciences, v. 99, p. 109–138, https://doi.org/10.1007/s00531-008-0366-4.

Jolivet, L., Faccenna, C., Goffé, B., Burov, E., and Agard, P., 2003, Subduction tectonics and exhumation of high-pressure metamorphic rocks in the Mediterranean orogens: American Journal of Science, v. 303, p. 353–409, https://doi.org/10.2475/ajs.303.5.353.

Jolivet, L., Famin, V., Mehl, C., Parra, T., Aubourg, C., Hébert, R., and Philippot, P., 2004, Strain localization during crustal-scale boudinage to form extensional metamorphic domes in the Aegean Sea, *in* Whitney, D.L., Teyssier, C., and Siddoway, C.S., eds., Gneiss Domes in Orogeny: Geological Society of America Special Paper 380, p. 185–210.

Jolivet, L., Lecomte, E., Huet, B., Denèle, Y., Lacombe, O., Labrousse, L., Le Pourhiet, L., and Mehl, C., 2010, The North Cycladic detachment system: Earth and Planetary Science Letters, v. 289, p. 87–104, https://doi.org/10.1016/j.epsl.2009.10.032.

Jolivet, L., Faccenna, C., Huet, B., Labrousse, L., Le Pourhiet, L., Lacombe, O., Lecomte, E., Burov, E., Denèle, Y., and Brun, J. P., 2013, Aegean tectonics: Strain localisation, slab tearing and trench retreat: Tectonophysics, v. 597–598, p. 1–33, https://doi.org/10.1016/j.tecto.2012.06.011.

Jolivet, L., Menant, A., Sternai, P., Rabillard, A., Arbaret, A., Augier, R., Laurent, V., Beaudoin, A., Grasemann, B., and Huet, B., 2015, The geological signature of a slab tear below the Aegean: Tectonophysics, v. 659, p. 166–182, https://doi.org/10.1016/j.tecto.2015.08.004.

Katzir, Y., Matthews, A., Garfunkel, Z., Schliestedt, M., and Avigad, D., 1996, The tectono-metamorphic evolution of a dismembered ophiolite (Tinos, Cyclades, Greece): Geological Magazine, v. 133, p. 237–254, https://doi.org/10.1017/S0016756800008992.

Katzir, Y., Avigad, D., Matthews, A., Garfunkel, Z., and Evans, B. W., 1999, Origin and metamorphism of ultrabasic rocks associated with a subducted continental margin, Naxos (Cyclades, Greece): Journal of Metamorphic Geology, v. 17, p. 301–318.

Katzir, Y., John, E., Valley, W., Matthews, A., and Spicuzza, M.J., 2002, Tracking fluid flow during deep crustal anatexis: Metasomatism of peridotites (Naxos, Greece): Contributions to Mineralogy and Petrology, v. 142, p. 700–713, https://doi.org/10.1007/s00410-001-0319-4.

Katzir, Y., Garfunkel, Z., Avigad, D., and Matthews, A., 2007, The geodynamic evolution of the Alpine orogen in the Cyclades (Aegean Sea, Greece): Insights from diverse origins and modes of emplacement of ultramafic rocks, *in* Taymaz, T., Yilmaz, Y., and Dilek, Y., eds., The Geodynamics of the Aegean and Anatolia: Geological Society of London Special Publication 291, p. 17–40.

Keay, S., Lister, G., and Buick, I., 2001, The timing of partial melting, Barrovian metamorphism and granite intrusion in the Naxos metamorphic core complex, Cyclades, Aegean Sea, Greece: Tectonophysics, v. 342, p. 275–312, https://doi.org/10.1016/S0040-1951(01)00168-8.

Kissel, C., and Laj, C., 1988, The Tertiary geodynamical evolution of the Aegean arc: A paleomagnetic reconstruction: Tectonophysics, v. 146, p. 183–201, https://doi.org/10.1016/0040-1951(88)90090-X.

Kohn, M.J., and Spear, F.S., 2000, Retrograde net transfer reaction insurance for pressure-temperature estimates: Geology, v. 28, p. 1127–1130, https://doi.org/10.1130/0091-7613(2000)28<1127:RNTRIF>2.0.CO;2.

Koukouvelas, I.K., and Kokkalas, S., 2003, Emplacement of the Miocene west Naxos pluton (Aegean Sea, Greece): A structural study: Geological Magazine, v. 140, p. 45–61, https://doi.org/10.1017/S0016756802007094.

Kruckenberg, S.C., Ferré, E.C., Teyssier, C., Vanderhaeghe, O., Whitney, D.L., Seaton, N.C.A., and Skord, J.A., 2010, Viscoplastic flow in migmatites deduced from fabric anisotropy: An example from the Naxos dome, Greece: Journal of Geophysical Research–Solid Earth, v. 115, B09401, https://doi.org/10.1029/2009JB007012.

Kruckenberg, S.C., Vanderhaeghe, O., Ferré, E.C., Teyssier, C., and Whitney, D.L., 2011, Flow of partially molten crust and the internal dynamics of a migmatite dome, Naxos, Greece: Tectonics, v. 30, TC3001, https://doi.org/10.1029/2010TC002751.

Kreulen, R., 1980, CO_2 rich fluids during regional metamorphism on Naxos (Greece); carbon isotopes and fluid inclusions: American Journal of Science, v. 280, no. 8, p. 745–771, https://doi.org/10.2475/ajs.280.8.745.

Lagos, M., Scherer, E. E., Tomaschek, F., Münker, C., Keiter, M., Berndt, J., and Ballhaus, C., 2007, High precision Lu–Hf geochronology of Eocene eclogite-facies rocks from Syros, Cyclades, Greece: Chemical Geology, v. 243, p. 16–35, https://doi.org/10.1016/j.chemgeo.2007.04.008.

Lamont, T.N., 2018, Unravelling the structural, metamorphic, and strain history of the “Aegean Orogeny,” Southern Greece, with a combined structural, petrological and geochronological approach [D.Phil thesis]: University of Oxford.

Laurent, V., Jolivet, L., Roche, R., Augier, R., Scaillet, R., and Cardello, G. L., 2016, Strain localization in a fossilized subduction channel: Insights from the Cycladic Blueschist Unit (Syros, Greece): Tectonophysics, v. 672–673, p. 150–169, https://doi.org/10.1016/j.tecto.2016.01.036.

Law, R.D., Searle, M.P., and Godin, L., 2006, Channel flow, ductile extrusion and exhumation in continental collision zones, *in* Law, R.D., Searle, M.P., and Godin, L., eds., Channel Flow, Ductile Extrusion, Exhumation in Continental Collision Zones: Geological Society of London Special Publication 268, https://doi.org/10.1144/GSL.SP.2006.268.01.28.

Le Pichon, X., and Angelier, J., 1979, The Hellenic arc and trench system: A key to the neotectonic evolution of the Eastern Mediterranean area: Tectonophysics, v. 60, p. 1–42, https://doi.org/10.1016/0040-1951(79)90131-8.

Le Pichon, X., and Angelier, J., 1981, The Aegean Sea: Philosophical Transactions of the Royal Society of London, v. 300, p. 357–372, https://doi.org/10.1098/rsta.1981.0069.

Le Pichon, X., Lallemant, S.J., Chamot-Rooke, N., Lemeur, D., and Pascal, G., 2002, The Mediterranean Ridge backstop and the Hellenic nappes: Marine Geology, v. 186, no. 1-2, p. 111–125, https://doi.org/10.1016/S0025-3227(02)00175-5.

Lee, J., Hacker, B., and Wang, Y., 2004, Evolution of North Himalayan gneiss domes: Structural and metamorphic studies in Mabja Dome, southern Tibet: Journal of Structural Geology, v. 26, p. 2297–2316, https://doi.org/10.1016/j.jsg.2004.02.013.

Lee, J., McClelland, W., Wang, Y., Blythe, A., and McWilliams, M., 2006, Oligocene–Miocene middle crustal flow in southern Tibet: Geochronology of Mabja Dome, *in* Law, R.D., Searle, M.P., and Godin, L., eds., Channel Flow, Ductile Extrusion and Exhumation in Continental Collision Zones: Geological Society of London Special Publication 268, p. 445–469, https://doi.org/10.1144/GSL.SP.2006.268.01.21.

Lister, G.S., Banga, G., and Feenstra, A., 1984, Metamorphic core complexes of cordilleran type in the Cyclades, Aegean Sea, Greece: Geology, v. 12, p. 221–225, https://doi.org/10.1130/0091-7613(1984)12<221:MCCOCT>2.0.CO;2.

Mahar, E.M., Baker, J.M., Powell, R., Holland, T.J.B., and Howell, N., 1997, The effect of Mn on mineral stability in metapelites: Journal of Metamorphic Geology, v. 15, p. 223–238, https://doi.org/10.1111/j.1525-1314.1997.00011.x.

Malandri, C., Soukis, K., Maffione, M., Özkaptan, M., Vassilakis, E., Lozios, S., and van Hinsbergen, D.J., 2016, Vertical-axis rotations accommodated along the Mid-Cycladic lineament on Paros Island in the extensional heart of the Aegean orocline (Greece): Lithosphere, v. 9, p. 78–99, https://doi.org/10.1130/L575.1.

Martin, L., Duchêne, S., Deloule, E., and Vanderhaeghe, O., 2006, The isotopic composition of zircon and garnet: A record of the metamorphic history of Naxos, Greece: Lithos, v. 87, p. 174–192, https://doi.org/10.1016/j.lithos.2005.06.016.

McClusky, S., Balassanian, S., Barka, A., Demir, C., Ergintav, S., Georgiev, I., Gurkan, O., Hamburger, M., Hurst, K., Kahle, H., and Kastens, K., 2000, Global positioning system constraints on plate kinematics and dynamics in the Eastern Mediterranean and Caucasus: Journal of Geophysical Research–Solid Earth, v. 105, no. B3, p. 5695–5719, https://doi.org/10.1029/1999JB900351.

Means, W.D., 1989, Stretching faults: Geology, v. 17, p. 893–896, https://doi.org/10.1130/0091-7613(1989)017<0893:SF>2.3.CO;2.

Menant, A., Jolivet, L., Augier, R., and Skarpelis, N., 2013, The North Cycladic Detachment System and associated mineralization, Mykonos, Greece: Insights on the evolution of the Aegean domain: Tectonics, v. 32, p. 433–452, https://doi.org/10.1002/tect.20037.

Miller, C.F., Stoddard, E.F., Bradfish, L.J., and Dollase, W.A., 1981, Composition of plutonic muscovite; genetic implications: Canadian Mineralogist, v. 19, p. 25–34.

Mizera, M., and Behrmann, J.H., 2015, Strain and flow in the metamorphic core complex of Ios Island (Cyclades, Greece): International Journal of Earth Sciences [Geologische Rundschau], v. 105, no. 7 p. 2097–2110, https://doi.org/10.1007/s00531-015-1259-y.

Newton, R.C., 1989, Metamorphic fluids in the deep crust: Annual Review of Earth and Planetary Sciences, v. 17, p. 385–410, https://doi.org/10.1146/annurev.ea.17.050189.002125.

Nijman, W., Kloppenburg, A., and de Vries, S.T., 2017, Archaean basin margin geology and crustal evolution: An East Pilbara traverse: Journal of the Geological Society [London], v. 174, p. 1090–1112, https://doi.org/10.1144/jgs2016-127.

Palin, R.M., Searle, M.P., Waters, D.J., Parrish, R.R., Roberts, N.M.W., Horstwood, M.S.A., Yeh, M.-W., Chung, S.L., and Anh, T.T., 2013, A geochronological and petrological study of anatectic paragneiss and associated granite dykes from the Day Nui Con Voi metamorphic core complex, North Vietnam: Constraints on the timing of metamorphism within the Red River shear zone: Journal of Metamorphic Geology, v. 31, p. 359–387, https://doi.org/10.1111/jmg.12025.

Palin, R.M., Weller, O.M., Waters, D.J., and Dyck, B., 2016, Quantifying geological uncertainty in metamorphic phase equilibria modelling; a Monte Carlo assessment and implications for tectonic interpretations: Geoscience Frontiers, v. 7, p. 591–607, https://doi.org/10.1016/j.gsf.2015.08.005.

Parra, T., Vidal, O., Jolivet, L., 2002, Relation between the intensity of deformation and retrogression in blueschist metapelites of Tinos Island (Greece) evidenced by chlorite–mica local equilibria: Lithos, v. 63, p. 41–66, https://doi.org/10.1016/S0024-4937(02)00115-9.

Patiño Douce, A.E., and Harris, N., 1998, Experimental constraints on Himalayan anatexis: Journal of Petrology, v. 39, p. 689–710, https://doi.org/10.1093/petroj/39.4.689.

Pattison, D.R.M., and Begin, N.J., 1994, Hierarchy of closure temperatures in granulites and the importance of an intergranular exchange medium (melt?) in controlling maximum Fe-Mg exchange temperatures: Mineralogical Magazine, v. 58A, p. 694–695, https://doi.org/10.1180/minmag.1994.58A.2.99.

Pattison, D.R.M., and Tracy, R.J., 1991, Phase equilibria and thermobarometry of metapelites: Mineralogy Society of America Reviews in Mineralogy, v. 26, p. 105–206.

Pattison, D.R.M., Chacko, T., Farquhar, J., and Mcfarlane, C.R.M., 2003, Temperatures of granulite-facies metamorphism: Constraints from experimental phase equilibria and thermobarometry corrected for retrograde exchange: Journal of Petrology, v. 44, p. 867–900, https://doi.org/10.1093/petrology/44.5.867.

Peillod, A., Ring, U., Glodny, J., and Skelton, A., 2017, An Eocene/Oligocene blueschist/greenschist-facies *P-T* loop from the Cycladic Blueschist Unit on Naxos Island, Greece: Deformation-related reequilibration vs thermal relaxation: Journal of Metamorphic Geology, v. 35, p. 805–830, https://doi.org/10.1111/jmg.12256.

Peterson, J.W., and Newton, R.C., 1989, Reversed experiments on biotite-quartz-feldspar melting in the system KMASH: Implications for crustal anatexis: The Journal of Geology, v. 97, p. 465–485, https://doi.org/10.1086/629323.

Pëto, P., 1976, An Experimental Investigation of Melting Reactions Involving Muscovite and Paragonite in the Silica-Saturated Portion of the System K_2O–Na_2O–Al_2O_3–SiO_2–H_2O to 15 kbar Total Pressure: UK Natural Environment Research Council.

Philippon, M., Brun, J.P., Gueydan, F., and Sokoutis, D., 2014, The interaction between Aegean back-arc extension and Anatolia escape since Middle Miocene: Tectonophysics, v. 631, p. 176–188, https://doi.org/10.1016/j.tecto.2014.04.039.

Platt, J.P., 1986, Dynamics of orogenic wedges and the uplift of high-pressure metamorphic rocks: Geological Society of America Bulletin, v. 97, p. 1037–1053, https://doi.org/10.1130/0016-7606(1986)97<1037:DOOWAT>2.0.CO;2.

Platt, J.P., Behr, W.M., Johanesen, K., and Williams, J.R., 2013, The Betic-Rif arc and its orogenic hinterland: A review: Annual Review of Earth and Planetary Sciences, v. 41, p. 313–357, https://doi.org/10.1146/annurev-earth-050212-123951.

Platt, J.P., Behr, W., and Cooper, F.J., 2014, Metamorphic core complexes: Windows into the mechanics and rheology of the crust: Journal of the Geological Society [London], v. 172, p. 9–27, https://doi.org/10.1144/jgs2014-036.

Powell, R., and Holland, T.J.B., 1988, An internally consistent thermodynamic dataset with uncertainties and correlations: 3. Application to geobarometry, worked examples and a computer program: Journal of Metamorphic Geology, v. 6, p. 173–204, https://doi.org/10.1111/j.1525-1314.1988.tb00415.x.

Powell, R., and Holland, T. J., 2008, On hermobarometry: Journal of Metamorphic Geology, v. 26, p. 155–179, https://doi.org/10.1111/j.1525-1314.2007.00756.x.

Powell, R., Holland, T.J.B., and Worley, B., 1998, Calculating phase diagrams involving solid solutions via non-linear equations, with examples using THERMOCALC: Journal of Metamorphic Geology, v. 16, p. 577–588, https://doi.org/10.1111/j.1525-1314.1998.00157.x.

Ramberg, H., 1980, Diapirism and gravity collapse in the Scandinavian Caledonides: Journal of the Geological Society London], v. 137, p. 261–260, https://doi.org/10.1144/gsjgs.137.3.0261.

Ramsay, J.G., and Huber, M.I., 1987, The Techniques of Modern Structural Geology, v. 2: Folds and Fractures: London, Pergamon Press, 392 p.

Rey, P.F., Teyssier, C., Kruckenberg, S.C., and Whitney, D.L., 2011, Viscous collision in channel explains double domes in metamorphic core complexes: Geology, v. 39, p. 387–390, https://doi.org/10.1130/G31587.1.

Rey, P.F., Mondy, L., Duclaux, G., Teyssier, C., Whitney, D.L., Bocher, M., and Prigent, C., 2017, The origin of contractional structures in extensional gneiss domes: Geology, v. 45, p. 263–266, https://doi.org/10.1130/G38595.1.

Ring, U., and Layer, P.W., 2003, High-pressure metamorphism in the Aegean, Eastern Mediterranean: Underplating and exhumation from the Late Cretaceous until the Miocene to Recent above the retreating Hellenic subduction zone: Tectonics, v. 22, 1022, https://doi.org/10.1029/2001TC001350.

Ring, U., Thomson, S.N., and Bröcker, M., 2003, Fast extension but little exhumation: The Vari detachment in the Cyclades, Greece: Geological Magazine, v. 140, p. 245–252, https://doi.org/10.1017/S0016756803007799.

Ring, U., Glodny, J., Will, T., and Thomson, S., 2007a, An Oligocene extrusion wedge of blueschists-facies nappes on Evia, Aegean Sea, Greece: Implications for the early exhumation of high-pressure rocks: Journal of the Geological Society [London], v. 164, p. 637–652, https://doi.org/10.1144/0016-76492006-041.

Ring, U., Will, T., Glodny, J., Kumerics, C., Gessner, K., Thomson, S., Güngör, T., Monie, P., Okrusch, M., and Drüppel, K., 2007b, Early exhumation of high-pressure rocks in extrusion wedges: Cycladic Blueschist Unit in the eastern Aegean, Greece, and Turkey: Tectonics, v. 26, TC2001, https://doi.org/10.1029/2005TC001872.

Ring, U., Glodny, J., Will, T., and Thomson, S., 2010, The Hellenic subduction system: High-pressure metamorphism, exhumation, normal faulting, and large-scale extension: Annual Review of Earth and Planetary Sciences, v. 38, p. 45–76, https://doi.org/10.1146/annurev.earth.050708.170910.

Roche, V., Laurent, V., Cardello, G.L., Jolivet, L., and Scaillet, S., 2016, Anatomy of the Cycladic Blueschist Unit on Sifnos Island (Cyclades, Greece): Journal of Geodynamics, v. 97, p. 62–87, https://doi.org/10.1016/j.jog.2016.03.008.

Rosenberg, C.L., and Handy, M.R., 2005, Experimental deformation of partially melted granite revisited: implications for the continental crust: Journal of Metamorphic Geology, v. 23, p. 19–28, https://doi.org/10.1111/j.1525-1314.2005.00555.x.

Sawyer, E.W., 1996, Melt segregation and magma flow in migmatites: Implications for the generation of granite magmas, *in* Brown, M., Candela, P.A., Peck, D.L., Stephens, W.E., Walker, R.J., and Zen, E.A., eds., The Third Hutton Symposium on the Origin of Granites and Related Rocks: Geological Society of America Special Paper 315, p. 85–94, https://doi.org/10.1130/0-8137-2315-9.85.

Sawyer, E.W., 2001, Melt segregation in the continental crust: Distribution and movement of melt in anatectic rocks: Journal of Metamorphic Geology, v. 19, p. 291–309, https://doi.org/10.1046/j.0263-4929.2000.00312.x.

Schmid, S.M., Scharf, A., Handy, M.R., and Rosenberg, C.L., 2013, The Tauern Window (eastern Alps, Austria): A new tectonic map, with cross-sections and a tectonometamorphic synthesis: Swiss Journal of Geosciences, v. 106, p. 1–32, https://doi.org/10.1007/s00015-013-0123-y.

Searle, M.P., 2010, Low-angle normal faults in the compressional Himalayan orogen; Evidence from the Annapurna-Dhaulagiri Himalaya, Nepal: Geosphere, v. 6, p. 296–315, https://doi.org/10.1130/GES00549.1.

Searle, M.P., and Cox, J., 1999, Tectonic setting, origin and obduction of the Oman ophiolite: Geological Society of America Bulletin, v. 111, p. 104–122, https://doi.org/10.1130/0016-7606(1999)111<0104:TSOAOO>2.3.CO;2.

Searle, M.P., and Cox, J., 2002, Subduction zone metamorphism during formation and emplacement of the Semail ophiolite in the Oman Mountains: Geological Magazine, v. 139, no. 3, p. 241–255, https://doi.org/10.1017/S0016756802006532.

Searle, M.P., Warren, C.J., Waters, D.J., and Parrish, R.R., 2004, Structural evolution, metamorphism and restoration of the Arabian continental margin, Saih Hatat region, Oman Mountains: Journal of Structural Geology, v. 26, p. 451–473, https://doi.org/10.1016/j.jsg.2003.08.005.

Searle, M.P., Law, R.D., and Jessup, M.J., 2006, Crustal structure, restoration and evolution of the Greater Himalaya in Nepal–South Tibet: Implications for channel flow and ductile extrusion of the middle crust, *in* Law, R.D., Searle, M.P., and Godin, L., eds., Channel Flow, Ductile Extrusion, Exhumation in Continental Collision Zones: Geological Society of London Special Publication 268, p. 355–378, https://doi.org/10.1144/GSL.SP.2006.268.01.17

Searle, M.P., Cottle, J.M., Streule, M.J., and Waters, D.J., 2010, Crustal melt granites and migmatites along the Himalaya: Melt source, segregation, transport and granite emplacement mechanisms: Earth and Environmental Science Transactions of the Royal Society of Edinburgh, v. 100, Special Issue 1–2, p. 219–233, https://doi.org/10.1017/S175569100901617X.

Seward, D., Vanderhaeghe, O., Siebenaller, L., Thomson, S., Hibsch, C., Zingg, A., Holzner, P., Ring, U., and Duchêne, S., 2009, Cenozoic tectonic evolution of Naxos Island through a multi-faceted approach of fission track analysis, *in* Ring, U., and Wernicke, B., eds., Extending a Continent: Architecture, Rheology, and Heat Budget: Geological Society of London Special Publication 321, p. 179–196.

Smye, A.J., Bickle, M.J., Holland, T.J.B., Parrish, R.R., and Condon, D.J., 2011, Rapid formation and exhumation of the youngest Alpine eclogites: A thermal conundrum to Barrovian metamorphism: Earth and Planetary Science Letters, v. 306, p. 193–204, https://doi.org/10.1016/j.epsl.2011.03.037.

Spear, F.S., 1993, Metamorphic Phase Equilibria and Pressure-Temperature-Time Paths: Mineralogical Society of America Monograph 1, 799 p.

Spear, F.S., and Selverstone, J., 1983, Quantitative *P-T* paths from zoned minerals: Theory and tectonic applications: Contributions to Mineralogy and Petrology, v. 83, p. 348–357, https://doi.org/10.1007/BF00371203.

Spear, F.S., Hickmott, D.D., and Selverstone, J., 1990, Metamorphic consequences of thrust emplacement, Fall Mountain, New Hampshire: Geological Society of America Bulletin, v. 102, p. 1344–1360, https://doi.org/10.1130/0016-7606(1990)102<1344:MCOTEF>2.3.CO;2.

Stevens, G., and Clemens, J.D., 1993, Fluid-absent melting and the roles of fluids in the lithosphere: a slanted summary?, Chemical Geology, v. 108, p. 1–17, https://doi.org/10.1016/0009-2541(93)90314-9.

Stipp, M., and Kunze, K., 2008, Dynamic recrystallization near the brittle-plastic transition in naturally and experimentally deformed quartz aggregates: Tectonophysics, v. 448, p. 77–97, https://doi.org/10.1016/j.tecto.2007.11.041.

Stipp, M., Stünitz, H., Heilbronner, R., and Schmid, S.M., 2002a, Dynamic recrystallization of quartz: Correlation between natural and experimental conditions, *in* De Meer, S., Drury, M.R., De Bresser, J.H.P., and Pennock, G.M., eds., Deformation Mechanisms, Rheology, and Tectonics: Current Status and Future Perspectives: Geological Society of London Special Publication 200, p. 171–190, https://doi.org/10.1144/GSL.SP.2001.200.01.11.

Stipp, M., Stünitz, H., Heilbronner, R., and Schmid, S.M., 2002b, The eastern Tonale fault zone: A 'natural laboratory' for crystal plastic deformation of quartz over a temperature range from 250 to 700 °C: Journal of Structural Geology, v. 24, p. 1861–1884, https://doi.org/10.1016/S0191-8141(02)00035-4.

St-Onge, M.R., 1984, The muscovite-melt bathograd and low-*P* isograd suites in north-central Wopmay orogen, Northwest Territories, Canada: Journal of Metamorphic Geology, v. 2, p. 315–326, https://doi.org/10.1111/j.1525-1314.1984.tb00592.x.

St-Onge, M.R., 1987, Zoned poikiloblastic garnets: *PT* paths and syn-metamorphic uplift through 30 km of structural depth, Wopmay orogen, Canada: Journal of Petrology, v. 28, p. 1–21, https://doi.org/10.1093/petrology/28.1.1.

Stouraiti, C., Pantziris, I., Vasilatos, C., Kanellopoulos, C.P., Mitropoulos, P., Pomonis, P., Moritz, R., and Chiaradia, M., 2017, Ophiolitic remnants from the upper and intermediate structural unit of the Attic-Cycladic Crystalline Belt (Aegean, Greece): Fingerprinting geochemical affinities of magmatic precursors: Geosciences, v. 7, p. 14, https://doi.org/10.3390/geosciences7010014.

Teyssier, C., and Whitney D.L., 2002, Gneiss domes and orogeny, Geology, v. 30, p. 1139–1142, https://doi.org/10.1130/0091-7613(2002)030<1139:GDAO>2.0.CO;2.

Thompson, A.B., 1982, Dehydration melting of pelitic rocks and the generation of H_2O-undersaturated granitic liquids: American Journal of Science, v. 282, p. 1567–1595.

Tippett, C.R., 1980, A Geological Cross-Section through the Southern Margin of the Foxe Fold Belt, Baffin Island, Arctic Canada, and its Relevance to the Tectonic Evolution of the Northeastern Churchill Province [Ph.D. thesis]: Kingston, Ontario, Canada, Queen's University.

Tomaschek, F., Kennedy, A.K., Villa, I.M., Lagos, M., and Ballhaus, C., 2003, Zircons from Syros, Cyclades, Greece—Recrystallization and mobilization of zircon during high-pressure metamorphism: Journal of Petrology, v. 44, p. 1977–2002, https://doi.org/10.1093/petrology/egg067.

Tracy, R.J., Robinson, P., and Thompson, A.B., 1976, Garnet composition and zoning in the determination of temperature and pressure of metamorphism, central Massachusetts: The American Mineralogist, v. 6, p. 762–775.

Tyler, I.M., and Ashworth, J.R., 1982, Sillimanite potash feldspar assemblages in graphitic pelites, Stronian area, Scotland: Contributions to Mineralogy and Petrology, v. 81, p. 18–29, https://doi.org/10.1007/BF00371155.

Urai, J.L., Schuiling, R.D., and Jansen, J.B.H., 1990, Alpine deformation on Naxos (Greece), *in* Knipe, R.J., and Rutter, E.H., eds., Deformation Mechanisms, Rheology and Tectonics: Geological Society of London Special Publication 54, p. 509–522.

Vanderhaeghe, O., 2004, Structural development of the Naxos migmatite dome, *in* Whitney, D.L., Teyssier, C., and Siddoway, C.S., eds., Gneiss Domes in Orogeny: Geological Society of America Special Paper 380, p. 211–227.

Vanderhaeghe, O., and Teyssier, C., 2001, Partial melting and flow of orogens: Tectonophysics, v. 342, p. 451–472, https://doi.org/10.1016/S0040-1951(01)00175-5.

Virgo, S., von Hagke, C., and Urai, J.L., 2018, 2018, Multiphase boudinage: A case study of amphibolites in marble in the Naxos migmatite core: Solid Earth, v. 9, p. 91–113, https://doi.org/10.5194/se-9-91-2018.

Von Hagke, C., Bamberg, B., Virgo, S., and Urai, J.L., 2018, Outcrop-scale tomography: Insights into the 3D structure of multiphase boudins: Journal of Structural Geology, v. 115, p. 311–317, https://doi.org/10.1016/j.jsg.2018.02.014.

Weinberg, R., and Hasalová, P., 2015, Water-fluxed melting of the continental crust: A review: Lithos, v. 212–215, p. 158–188, https://doi.org/10.1016/j.lithos.2014.08.021.

Weller, O.M., St-Onge, M.R., Waters, D.J., Rayner, N., Searle, M.P., Chung, S.-L., Palin, R.M., Lee, Y.-H., and Xu, X., 2013, Quantifying Barrovian metamorphism in the Danba structural culmination of eastern Tibet: Journal of Metamorphic Geology, v. 31, p. 909–935, https://doi.org/10.1111/jmg.12050.

Wernicke, B., 1981, Low-angle normal faults in the Basin and Range Province: Nappe tectonics in an extending orogeny: Nature, v. 291, p. 645–648.

Wernicke, B., 1985, Uniform normal-sense simple shear of the continental lithosphere: Canadian Journal of Earth Sciences, v. 22, p. 108–125.

White, R.W., and Powell, R., 2002, Melt loss and the preservation of granulite-facies mineral assemblages: Journal of Metamorphic Geology, v. 20, p. 621–632.

White, R.W., Powell, R., and Clarke, G.L., 2002, The interpretation of reaction textures in Fe-rich metapelitic granulites of the Musgrave block, central Australia: Constraints from mineral equilibria calculations in the system K_2O-FeO-MgO-Al_2O_3-SiO_2-H_2O-TiO_2-Fe_2O_3: Journal of Metamorphic Geology, v. 20, p. 41–55, https://doi.org/10.1046/j.0263-4929.2001.00349.x.

White, R.W., Powell, R., and Halpin, J.A., 2004, Spatially focused melt formation in aluminous metapelites from Broken Hill, Australia: Journal of Metamorphic Geology, v. 22, p. 825–845, https://doi.org/10.1111/j.1525-1314.2004.00553.x.

White, R.W., Pomroy, N.E., and Powell, R., 2005, An in-situ metatexite-diatexite transition in upper amphibolite-facies rocks from Broken Hill, Australia: Journal of Metamorphic Geology, v. 23, p. 579–602, https://doi.org/10.1111/j.1525-1314.2005.00597.x.

White, R.W., Powell, R., and Holland, T.J.B., 2007, Progress relating to calculation of partial melting equilibria for metapelites: Journal of Metamorphic Geology, v. 25, p. 511–527, https://doi.org/10.1111/j.1525-1314.2007.00711.x.

Whitney, D.L., and Evans, B.W., 2010, Abbreviations for names of rock-forming minerals: The American Mineralogist, v. 95, p. 185–187, https://doi.org/10.2138/am.2010.3371.

Whitney, D.L., and Irving, A.J., 1994, Origin of K-poor leucosomes in a metasedimentary migmatite complex by ultrametamorphism, syn-metamorphic magmatism and subsolidus processes: Lithos, v. 32, p. 173–192, https://doi.org/10.1016/0024-4937(94)90038-8.

Wiederkehr, M., Bousquet, R., Schmid, S.M., and Berger, A., 2008, From subduction to collision: thermal overprint of HP/LT meta-sediments in the north-eastern Lepontine Dome (Swiss Alps) and consequences regarding the tectono-metamorphic evolution of the Alpine orogenic wedge: Swiss Journal of Geosciences, v. 101, https://doi.org/10.1007/s00015-008-1289-6.

Wijbrans, J.R., van Wees, J.D., Stephenson, R.A., and Cloetingh, S.A.P.L., 1993, Pressure-temperature-time evolution of the high-pressure, metamorphic complex of Sifnos, Greece: Geology, v. 21, p. 443–446, https://doi.org/10.1130/0091-7613(1993)021<0443:PTTEOT>2.3.CO;2.

Woodsworth, G.J., 1977, Homogenization of zoned garnets from pelitic schists: Canadian Mineralogist, v. 15, p. 230–242.

Wortel, M.J.R., and Spakman, W., 2000, Subduction and slab detachment in the Mediterranean-Carpathian region: Science, v. 290, no. 5498, p. 1910–1917, https://doi.org/10.1126/science.290.5498.1910.

Yin, A., 1991, Mechanisms for the formation of domal and basinal detachment faults: A three-dimensional analysis: Journal of Geophysical Research, v. 96, p. 14,577–14,594, https://doi.org/10.1029/91JB01113.

Science Editor: Aaron J. Cavosie
Associate Editor: Nicholas Erik Timms

Manuscript Received 27 November 2017
Revised Manuscript Received 9 September 2018
Manuscript Accepted 4 April 2018

Printed in the USA